ACOUSTIC SCATTERING ANALYSIS FOR REMOTE SENSING OF MANGANESE NODULES

by

Yushieh Ma

Dissertation submitted to the Faculty of the

Virginia Polytechnic Institute and State University

in partial fulfillment of the requirements for the degree of

DOCTOR OF PHILOSOPHY

in

Aerospace and Ocean Engineering

APPROVED:

Allen H. Magnuson, Chairman

Joseph A. Schetz

K. Sundkvist

Werner E. Kohler

Ioannis M. Besieris

March, 1982

Blacksburg, Virginia

ACKNOWLEDGEMENTS

The author would like to express his sincere appreciation to Dr. Allen H. Magnuson for his patience, guidance and encouragement extended throughout the research work.

Special thanks are due Dr. Karl Sundkvist, Dr. Joseph A. Schetz, Dr. Werner E. Kohler and Dr. Ioannis M. Besieris for their advice.

The author also wishes to show his gratitude to his parents, Mr. and Mrs. Hungshung Ma, his wife Yuanling and son Harvey for their love and support throughout the graduate study.

This work is sponsored by NOAA Office of Sea Grant, Department of Commerce, under Grant # NA-80-AAD-00020.

TABLE OF CONTENTS

LIST OF TABLES

LIST OF FIGURES

NOMENCLATURE

$\vec{A}$	Vector potential, or directional area
A	Area, or scattering characteristics
A_r, A_θ, A_ψ	Components of $\vec{A}$ in spherical coordinates
a	Radius of sphere
B_n, a_n, b_n, D_n	Expansion coefficients
b	Rayleigh size distribution parameter
C_n	Expansion coefficients for elastic sphere
C_{nf}	Expansion coefficients for fluid sphere
C^+	Coherent reflection coefficient
C^-	Coherent transmission coefficient
c	Speed of wave propagation
d	Exclusion length
$E(\vec{R},\vec{r})$	Propagation function
Exp ( )	Exponential of ( )
$\vec{e}_r, \vec{e}_\theta, \vec{e}_\chi$	Unit vectors in spherical coordinates
erf ( )	Error function
e	Compressibility ratio
$\vec{e}_z$	Unit vector in the positive z direction
$F(\omega)$	Fourier transform of pulse
F	Random function
$f(a,\theta)$	Scattering function
f(R)	Radial distribution function
g	Density ratio

H	The depth measured from the receiver
$H(\ )$	Function of ( )
h	Sound velocity ratio
$h_n^{(\frac{1}{2})}(\ )$	Spherical Hankel function
I	Wave intensity (energy flux)
$Im(\ )$	Imaginary part of ( )
i	Imaginary unit ($i^2 = -1$)
$j_n(\ )$	Spherical Bessel function
k	Wave number
N	Total number of scatterers
$n_n(\ )$	Spherical Neumann function
$O(\ )$	Order of ( )
$P(\ )$	Joint probability function
$P_n(\cos\theta)$	Legendre polynomial
p	Pressure
$q(\ )$	Size probability density function
R	Distance between scatterer and receiver, or distance between two scatterers
R_θ	Reflectivity factor
Re	Real part of ( )
$\vec{r}$	Position vector on z = 0 plane
r,θ,ψ	Spherical coordinates
s	Scattering parameter, or entropy
TS	Target strength
t	Time
$U(\vec{R})$	Total scattered field at $\vec{R}$

$\vec{u}$	Displacement vector
u_j	Scattered field from the jth scatterer
u_r, u_θ, u_ψ	Components of $\vec{u}$ in spherical coordinates
$\vec{v}$	Velocity vector
$w(\ )$	Locational probability distribution function
x,y,z	Rectangular coordinates
$\vec{x}$	Position vector
$Y_{m,n}(\ )$	Spherical harmonic
λ	Lamé elastic constant
μ	Lamé parameter (rigidity modulus), or absorption coefficient
θ	Scattering angle
ω	Radial frequency
α	Gaussian beamform coefficient
Δ	Dilatation
δ_{nm}	Kronecker delta
δ_{HP}	Half power beam width
Ω	Solid angle
$\sigma_{rr}, \sigma_{r\theta}$	Stress components in spherical coordinates
ρ	Mass density, or area number density
σ	Total scattering cross section
σ^+	Total backscatter cross section
σ^-	Total forward scatter cross section
ϕ	Scalar displacement potential
$\phi_o(\omega)$	Integration constant
$\Gamma(\ )$	Gamma function

∂	Partial differential operator
∇	Gradient operator
$\cdot$	Denotes scalar multiplication of two vectors
$\times$	Denotes cross product of two vectors
$( )'$	Perturbation quantity, or derivative
$\frac{d}{dt}$	Total differential operator
ψ	Wave function (acoustic potential)
$< >$	Configurational average
$< >_j$	Configurational average holding jth scatterer fixed
$< >_{jk}$	Configurational average holding jth and kth scatterer fixed
[ ]	Number in brackets designates references at the end of the thesis

Subscripts

a	Amplitude
b.s.	Backscatter
E	Refers to elastic medium
f	Refers to fluid sphere
f,r	Refers to radial components in fluid sphere
HS	Refers to horizontal shear wave
i	Refers to incident wave
i,r	Refers to radial component in incident wave
j,k,ℓ	Refers to jth, kth, ℓth nodule
L	Refers to longitudinal wave
m,n	Indices (integer)
s	Refers to scattered wave

s,r	Refers to radial component in scattered wave
T	Refers to transverse wave
VS	Refers to vertical shear wave
0	Refers to undisturbed quantity

Superscripts

*	Complex conjugate
-	Average value
→	Vector sign
j,k	External field of the jth (or kth) scatterer
^	Nondimensional quantity
+	$z > 0$ plane
-	$z < 0$ plane

PART ONE

ACOUSTIC SCATTERING ANALYSIS FOR THE SINGLE NODULE

I. INTRODUCTION, Part 1

Manganese nodules occur over millions of square miles of the deep ocean basins. The deposits are vast: in the Pacific Ocean alone, a recent estimate suggests the presence of about 350 billion tons of manganese, 200 billion tons of iron, 15 billion tons of nickel, 8 billion tons of copper, and 5 billion tons of cobalt [1].

Since the late 1950's and early '60's the manganese nodule deposits have attracted much attention as a potential marine mineral resource. Manganese nodules have also been studied extensively since then and many reasonably good regional maps that show their gross distribution have been established [2]. However there is still much to be learned on a smaller scale. Certainly, for efficient exploitation more work is needed, because the distribution of manganese nodules on the ocean basins is not all that even and the composition is not as uniform as the maps indicate.

The potential deep sea mining sites for manganese nodules must contain a sufficient abundance of nodules for economic gain, and the nodules must conform to certain size limitations imposed by the newly developed deep sea mining equipment. This makes the prospection or exploration so important. The industry is now in the last stages of test and evaluation of prototype mining systems [3]. However, the prospecting techniques are still under improvement.

Exiting prospecting techniques involve combinations of spot-checking and deep-tow surveillance. Spot-checking employs lowering optical

sensors, grad samplers, box corners or dredgers several miles to the ocean floor to examine the ocean bed and obtain the bottom samples [1]. The other involves a towed "fish" which is a sensor package containing photographic equipment, videotape equipment, side-scan sonar and transponders. The fish is usually towed at a very low speed (2 knots or lower) a constant distance (about 10-20 m) above the ocean bottom [4]. Accidents such as cable cutting or collisions with obstacles may occur on towing such systems.

One sees that either speed of the mentioned surveillance is very low because of the long cable and deck machinery needed to deploy and operate the sensor systems, making prospecting very expensive. An alternative is therefore desirable to increase the speed of surveillance which will greatly decrease the prospecting cost.

One way to increase the surveillance speed is to eliminate the long cable from which the instrumentation is suspended by using a remote sensing system. That is, the sensor system mounted either on a "fish" shallowly (on or just beneath the water surface) towed behind a surveying vessel (see Figure 1) at a normal crusing speed (8-10 knots) or in the vessel.

Acoustic sounding is commonly used to obtain information on the nature of the ocean floor. It should be noted that most survey vessels have a subbottom profiler (frequency range from 3 to 5 kHz), an echo sounder (8-15 kHz) and a precision depth recorder sounder (25-35 kHz). Therefore by using existing shipboard sounding systems and by proper analysis and interpretation of bottom-reflected pulse data, the presence of and amount of nodules can be inferred. Potential mining

sites for manganese nodules can thus be easily identified from the nodule distribution maps [2] through this remote sensing survey.

Generally speaking, in establishing the feasibility of prospecting for manganese nodules by using remote acoustic sounding two important problems will be encountered. First, the single nodule scattering problem needs to be solved and then these results can be used in the solution of the multiple scattering problem. From this information predictions of the reflected return sound pulse sent from a survey vessel can then be compared to experimental results obtained in the lab to infer the presence of and amount of nodules.

The scattering of sound was first investigated mathematically by Lord Rayleigh [5] who considered a sphere of dimensions small compared to a wavelength. For Rayleigh scattering both the diameter and the wavelength enter into the scattering in a simple power relationship. Anderson [6] was concerned with scattering from spheres whose acoustic properties are near those of the surrounding medium, and of diameters up to several wavelengths. Faran [7] studied sound scattering by cylinders and spheres of solid material and gave several mathematical solutions. Hickling [8] also did an analysis of backscattering from a solid elastic sphere in water and compared experimental results with his calculations.

To make the single scatterer analysis tractable, it is necessary to use an idealized (but still meaningful) geometry. No single geometric form can be attributed to actual manganese nodules which are randomly shaped but on the average can be described as oblate, discord, or prolate [9]. In this thesis, the nodule will be modeled as an elastic

sphere (each scatterer on the bottom has a circular cross-section, see Figure 2), which has both compressional and shear wavespeeds and wet mass density of the nodule material, half submerged in the sedimentary bottom (see Figure 3). The bottom is, in general, composed of abyssal silt which is relatively transparent to sound waves and its presence will be ignored. Thus, the total analysis assumes there is no interaction between the bottom and the nodule (see Figure 4). The surrounding medium (ocean) will be taken as a homogeneous and isotropic inviscid fluid.

Nonlinear governing equations for the acoustic medium are perturbed to give a linearized wave equation. The elastodynamic vector wave equation from [10] is used for the nodules. Solutions for the linearized wave equations are expressed in terms of scalar potentials. The solutions are then used in the scattering computation for the elastic sphere excited by an incoming plane wave. The scattering cross section is computed, the scattering function is derived (which will be widely used in the multiple scattering analysis) and the results are presented to characterize the wave scattering from a single nodule.

Results are presented first in algebraic form for Rayleigh scattering which is a low frequency scattering case. After this, results for a fluid sphere and a fixed rigid sphere, which are special cases of scattering from an elastic sphere, are provided. Computer programs were written for computing scattering properties and numerical results are presented for total scattering cross sections of fluid and fixed rigid spheres and the backscattering reflectivity factor of the elastic sphere. These results are compared with those from previous

investigators to ensure that the equations and the computer programs used in the scattering calculations are correct. Computations for manganese nodules are then carried out using the verified computer programs and results are presented as plots of nondimensional scattering cross section versus nondimensional wave frequency and the backscattering reflectivity versus nondimensional wave frequency. Experimental values for the wave speeds in the nodule and nodule wet densities obtained from a related investigation at Virginia Tech were used in the computations.

II. GOVERNING EQUATIONS FOR THE ACOUSTIC AND ELASTIC MEDIA

The dynamic field equations are derived for monochromatic waves propagating in an inviscid fluid and in an elastic medium. For the inviscid fluid the equation of motion, equation of continuity, and equation of state are linearized by taking small disturbances from an equilibrium state. The reduced wave equation is obtained by combining the linear field and state equations. The linearized elastodynamic vector field equation is written for the solid medium and simplified using techniques [11] for electromagnetic wave propagation problems. After simplifying the field equation for the solid to scalar Helmholtz equations, the vector problem is reduced to finding three scalar potentials which are the solutions of three scalar Helmholtz equations in both longitudinal and transverse displacement fields.

A. Linearized Acoustic Wave Equation

A fluid medium at rest is taken with uniform density ρ_0, pressure p_0, displacement $\vec{u} = \vec{0}$ and velocity $\vec{v} = \vec{0}$. After disturbing the medium, i.e., in the presence of sound waves sent by the transmitter, the displacement, velocity, density and pressure become $\vec{u}'(\vec{x},t)$, $\vec{v}'(\vec{x},t)$, $\rho_0 + \rho'(\vec{x},t)$ and $p_0 + p'(\vec{x},t)$, respectively, where the primes denote the perturbed values. It is assumed that the disturbance is relatively weak so the nonlinear effects are negligible and the only energy involved in the acoustic motion is mechanical. The continuity

equation, equation of motion and equation of state are, respectively,

$$\frac{\partial \rho}{\partial t} + \nabla\cdot(\rho\vec{v}) = 0 \tag{1}$$

$$\rho \frac{d\vec{v}}{dt} = - \text{grad } p \tag{2}$$

$$p = H(\rho,s) \ , \tag{3}$$

where s is the entropy.

Substituting the expansion for velocity, density and pressure into (1) - (3) and linearizing them by retaining only first-order terms in the primed quantities, the equations then reduce to

$$\frac{\partial \rho'}{\partial t} + \rho_0 \nabla\cdot\vec{v}' = 0 \tag{4}$$

$$\rho_0 \frac{\partial \vec{v}'}{\partial t} + \nabla p' = 0 \tag{5}$$

$$p' = c_0^2 \rho' \ , \tag{6}$$

where $\rho' << \rho_0$, $|\vec{v}'| << c_0$, $p' << p_0$ and c_0 is the adiabatic sound speed in the fluid medium. By taking time derivatives $\left(\frac{\partial}{\partial t}\right)$ and $\left(\frac{\partial^2}{\partial t^2}\right)$ of Eqs. (4) and (6), respectively, Eqs. (4) and (6) then become

$$\frac{\partial^2 \rho'}{\partial t^2} + \rho_0 \nabla\cdot\left(\frac{\partial \vec{v}'}{\partial t}\right) = 0 \tag{4-a}$$

$$\frac{\partial^2 p'}{\partial t^2} = c_0^2 \frac{\partial^2 \rho'}{\partial t^2} \ . \tag{6-a}$$

Introducing $\frac{\partial \vec{v}'}{\partial t} = - \frac{\nabla p'}{\rho_0}$ from Eq. (5) in (4-a) gives

$$\frac{\partial^2 \rho'}{\partial t^2} = \nabla\cdot(\nabla p') \ . \tag{7}$$

Eliminating the density in (6-a) and (7) gives the acoustic wave equation

$$\nabla^2 p' = \frac{1}{c_0^2} \frac{\partial^2 p'}{\partial t^2} \quad . \tag{8}$$

Eq. (8) is of differential form in space and time. It can be handled more conveniently in the frequency domain. One introduces the following Fourier transform pair:

$$F(\omega) = \int_{-\infty}^{\infty} f(t)\, e^{-i\omega t}\, dt$$

and

$$f(t) = \frac{1}{2\pi} \int_{-\infty}^{\infty} F(\omega)\, e^{i\omega t}\, d\omega \ , \tag{9}$$

where ω is the radian frequency.

One sees from (9) that time differentiation is represented in the frequency domain by multiplication by $i\omega$. Eq. (8) can be written in the frequency domain as follows:

$$(\nabla^2 + k^2)\, p = 0 \ , \tag{8-a}$$

where p is the perturbation pressure and k is the wavenumber which is equal to ω/c_0.

B. Wave Equations for the Elastic Solid

The field equation for the elastic solid in the frequency domain is written from [10] as

$$-\rho_E \omega^2 \vec{u} + \mu[\nabla x(\nabla x\vec{u})] - (\lambda + 2\mu)\, \nabla(\nabla\cdot\vec{u}) = \vec{0} \ , \tag{10}$$

Using (14), Eqs. (11) and (12) may be written as

$$[\nabla^2 + k_L^2]\,(\nabla\cdot\vec{u}_L) = 0 \qquad (11\text{-a})$$

$$[\nabla x\nabla x - k_T^2]\,(\nabla x\vec{u}_T) = \vec{0}\ . \qquad (12\text{-a})$$

Eqs. (11-a) and (12-a) can be manipulated as follows:

$$\nabla\cdot[(\nabla\nabla\cdot + k_L^2)\,\vec{u}_L] = 0 \qquad (11\text{-b})$$

$$\nabla x[(\nabla x\nabla x - k_T^2)\,\vec{u}_T] = \vec{0} \qquad (12\text{-b})$$

It follows from (14) that,

$$\nabla x[(\nabla\nabla\cdot + k_L^2)\,\vec{u}_L] = \vec{0} \qquad (11\text{-c})$$

$$\nabla\cdot[(\nabla x\nabla x - k_T^2)\,\vec{u}_T] = 0\ . \qquad (12\text{-c})$$

From vector analysis, it is known that, except for the constant vector field which is trivial in the present case, if both the divergence and curl of a vector field vanish, then the vector field itself must vanish. The quantities inside the brackets in Eqs. (11-b) and (12-b) and (11-c) and (12-c) must vanish, leaving

$$[\nabla\nabla\cdot + k_L^2]\,\vec{u}_L = \vec{0} \qquad (11\text{-d})$$

and

$$[\nabla x\nabla x - k_T^2]\,\vec{u}_T = \vec{0}\ . \qquad (12\text{-d})$$

Both of these are now vector wave equations. The solution to each equation will have an implicit time dependence $e^{i\omega t}$.

C. General Solutions to the Wave Equations

Due to the geometry of the problem, the spherical coordinate system is introduced. The general solution to Eq. (8-a) is [12]

in which $\vec{u}$ is the perturbation displacement vector.

Taking the divergence of Eq. (10) gives

$$[\nabla^2 + k_L^2] (\nabla \cdot \vec{u}) = 0 , \tag{11}$$

where $k_L = \frac{\omega}{c_L}$

$$c_L = \sqrt{\frac{\lambda+2\mu}{\rho_E}}$$

ρ_E = the density of the elastic solid

λ, μ = Lamé constants

c_L = the longitudinal sound velocity in the elastic solid.

Since the divergence of a vector is a scalar, Eq. (11) is thus recognized as a scalar wave equation for the elastic solid.

Taking the curl of Eq. (10) gives

$$[\nabla x \nabla x - k_T^2] (\nabla x \vec{u}) = 0 , \tag{12}$$

where $k_T = \frac{\omega}{c_T}$, $c_T = \sqrt{\frac{\mu}{\rho_E}}$, and c_T is the transverse sound velocity in the elastic solid.

It is convenient at this point to decompose the displacement vector into longitudinal (or irrotational) and transverse (or solenoidal) parts as follows:

$$\vec{u} = \vec{u}_L + \vec{u}_T , \tag{13}$$

where the subscript L refers to the longitudinal component and T refers to the transverse component; that is,

$$\begin{aligned} \nabla \cdot \vec{u}_T &= 0 \\ \nabla \times \vec{u}_L &= \vec{0} \end{aligned} \tag{14}$$

$$p = \sum_{n,m=0}^{\infty} p_{m,n}\, Y_{m,n}\,(\theta,\psi) \begin{bmatrix} j_n\,(kr) \\ \\ n_n\,(kr) \end{bmatrix}, \tag{15}$$

where $Y_{m,n}\,(\theta,\psi)$ is the spherical harmonic, $j_n(kr)$ and $n_n(kr)$ are the spherical Bessel function and Neumann function, respectively. The notation is indicated in Figure 5.

Solutions to Eqs. (11-d) and (12-d) may be written from electromagnetic theory [11] as

$$\vec{u}_L = \nabla\phi_L \tag{16}$$

and

$$\vec{u}_T = \nabla x\vec{A}\,, \tag{17}$$

where ϕ_L is a scalar potential and $\vec{A}$ is a vector potential. One usually imposes on the vector potential the following condition

$$\nabla\cdot\vec{A} = 0 \tag{18}$$

to eliminate the possibility $\vec{A}$ being the gradient of another scalar function.

To find the equation that governs ϕ_L, one substitutes Eq. (16) into (11-d). This gives

$$[\nabla\nabla\cdot + k_L^{\,2}]\,(\nabla\phi_L) = \vec{0}\,. \tag{11-e}$$

Eq. (11-e) can be manipulated as

$$\nabla[(\nabla^2 + k_L^{\,2})\,\phi_L] = \vec{0}\,. \tag{11-f}$$

Integrating Eq. (11-f) spatially gives

$$(\nabla^2 + k_L^{\,2})\,\phi_L = \phi_0(\omega) \tag{11-g}$$

where ϕ_o is uniform spatially, and may be set to zero with no loss in generality because the preferred solutions are spatially dependent. Eq. (11-g) thus becomes

$$(\nabla^2 + k_L^2)\ \phi_L = 0\ . \tag{19}$$

One sees that the longitudinal field is the gradient of a scalar function which is obtained by solving a Helmholtz equation.

The vector potential $\vec{A}$ has two components corresponding to two polarizations, the vertical shear and the horizontal shear. The vertical shear component can be expressed as [11]

$$\vec{A}_{VS} = \nabla x(r\vec{e}_r\ \phi_{VS})\ , \tag{20}$$

where ϕ_{VS} is a scalar function, r the radial component, and $\vec{e}_r$ the unit vector in $\vec{r}$ direction. The subscript VS denotes this solution as a "vertical shear" wave.

Due to the symmetry of this problem (see Figure 5), there is no ψ dependence. Substituting Eq. (20) into (17) and using

$$\nabla x\vec{A} = \frac{1}{r^2 \sin\theta}\begin{vmatrix} \vec{e}_r & r\vec{e}_\theta & r\sin\theta\ \vec{e}_\psi \\ \frac{\partial}{\partial r} & \frac{\partial}{\partial\theta} & \frac{\partial}{\partial\psi} \\ A_r & rA_\theta & r\sin\theta\ A_\psi \end{vmatrix}\ , \tag{20-a}$$

gives

$$\vec{u}_{VS} = -\left(\frac{\cot\theta}{r}\frac{\partial\phi_{VS}}{\partial\theta} + \frac{1}{r}\frac{\partial^2\phi_{VS}}{\partial\theta^2}\right)\vec{e}_r + \left(\frac{1}{r}\frac{\partial\phi_{VS}}{\partial\theta} + \frac{\partial^2\phi_{VS}}{\partial r\partial\theta}\right)\vec{e}_\theta, \tag{20-b}$$

where A_r, A_θ and A_ψ are the r, θ and ψ components of $\vec{A}$, and $\vec{e}_\theta$ and $\vec{e}_\psi$ are the unit vectors in θ and ψ directions. One sees that $\vec{u}_{VS}$ is on the

r-θ plane and this is where the name "vertical shear" comes from.

The curl of Eq. (20) is also a solution to Eq. (17), that is

$$\vec{A}_{HS} = \frac{1}{k_T} \nabla x[\nabla x(r\vec{e}_r \phi_{HS})] , \tag{21}$$

where ϕ_{HS} is another potential function. The HS designation implies that the solution is a "horizontal shear" wave because taking the curl of Eq. (21) and using (20-a) and (17) gives

$$\vec{A}_{HS} = \frac{1}{k_T} \left[\frac{2}{r} \frac{\partial^2 \phi_{HS}}{\partial r \partial \theta} + \frac{\partial^3 \phi_{HS}}{\partial r^2 \partial \theta} - \frac{\csc^2 \theta}{r^2} \frac{\partial \phi_{HS}}{\partial \theta} + \frac{\cot\theta}{r^2} \frac{\partial^2 \phi_{HS}}{\partial \theta^2} + \frac{1}{r^2} \frac{\partial^3 \phi_{HS}}{\partial \theta^3} \right] \vec{e}_\chi , \tag{21-a}$$

which lies on the plane normal to r-θ plane. The k_T factor has been introduced in Eq. (21) in order to give ϕ_{VS} and ϕ_{HS} the same dimensions.

To find the governing equations for the scalar potentials ϕ_{VS} and ϕ_{HS} first take the curl of Eq. (20) giving

$$\nabla x \vec{A}_{VS} = \nabla \left(\frac{\partial r \phi_{VS}}{\partial r} \right) - r \vec{e}_r \nabla^2 \phi_{VS} . \tag{22}$$

Now taking the curl of the curl of Eq. (22) gives

$$\nabla x \nabla x (\nabla x \vec{A}_{VS}) = \nabla x \nabla x \nabla \left(\frac{\partial r \phi_{VS}}{\partial r} \right) - \nabla x \nabla x (r \vec{e}_r \nabla^2 \phi_{VS}) . \tag{22-a}$$

Since $\nabla x \vec{A}_{VS}$ is a transverse wave and curl grad ( ) = $\vec{0}$, substitution of Eq. (12-d) into the left hand side of Eq. (22-a) gives

$$k_T^2 (\nabla x \vec{A}_{VS}) = - \nabla x \nabla x (r \vec{e}_r \nabla^2 \phi_{VS}) . \tag{22-b}$$

Comparing both sides of Eq. (22-b) using (20) one sees that ϕ_{VS} must satisfy

$$(\nabla^2 + k_T^2)\ \phi_{VS} = 0 \ . \tag{23}$$

Eq. (23) is a scalar Helmholtz equation. The same procedure can be applied to the HS polarization to get

$$(\nabla^2 + k_T^2)\ \phi_{HS} = 0 \ . \tag{24}$$

To summarize, the elastic vector field equation has been reduced to three polarizations: two transverse and one longitudinal. The displacement field may then be written as

$$\vec{u} = \vec{u}_L + \vec{u}_{VS} + \vec{u}_{HS}$$

where,
$$\vec{u}_L = \nabla\phi_L$$
$$\vec{u}_{VS} = \nabla x \nabla x\ (r\ \vec{e}_r\ \phi_{VS}) \tag{25}$$
$$\vec{u}_{HS} = \frac{1}{k_T}\ \nabla x \nabla x \nabla x\ (r\ \vec{e}_r\ \phi_{HS}) \ .$$

The vector problem has been reduced to finding the scalar potentials ϕ_L, ϕ_{VS} and ϕ_{HS} which are the solutions of the following scalar Helmholtz equations satisfying the appropriate boundary conditions at the fluid-solid interface.

$$(\nabla^2 + k_L^2)\ \phi_L = 0$$

and (25-a)

$$(\nabla^2 + k_T^2) \begin{Bmatrix} \phi_{VS} \\ \\ \phi_{HS} \end{Bmatrix} = 0 \ .$$

The general expansions in spherical coordinates for ϕ_L, ϕ_{VS} and ϕ_{HS} are similar to Eq. (15) where the proper wave numbers k_L and k_T are substituted for k.

III. SCATTERING COMPUTATION FOR THE ELASTIC SPHERE WITH PLANE WAVE EXCITATION

A time-harmonic plane wave of sound of frequency ω in a fluid medium is incident upon an isotropic elastic sphere of radius a. The center of the sphere coincides with the origin of the coordinate system and the plane wave approaches the sphere along the negative z-axis, as shown in Figure 5. Because of symmetry there is no ψ dependence in the solution to the problem. Eq. (15) reduces to the simpler form [12]

$$p_i = p_a \sum_{n=0}^{\infty} (2n+1)\, i^n\, j_n(kr)\, P_n(\cos\theta) , \qquad r \geq 0 \tag{26}$$

where the subscript i denotes the incident wave, p_a is the pressure amplitude, and $P_n(\cos\theta)$ is the Legendre polynomial. The reason for using $j_n(kr)$ as the appropriate spherical Bessel function in (26) is that j_n is finite at $r = 0$. Actually Eq. (26) is the spherical expansion of the incident plane wave

$$p_i = p_a\, e^{ikr\cos\theta} . \tag{27}$$

In addition to the original incoming plane wave there is a scattered or diffracted wave that propagates energy in all directions. The pressure in the outgoing scattered wave, i.e., the scattered pressure field external to the sphere, will be of the form [12]

$$p_s = \sum_{n=0}^{\infty} B_n\, h_n^{(2)}(kr)\, P_n(\cos\theta) , \qquad r \geq a \tag{28}$$

where the subscript s denotes the scattered wave and $h_n^{(2)}(kr)$ is the spherical Hankel function for outgoing waves for time dependence $e^{i\omega t}$. The B_n coefficients must be evaluated using proper boundary conditions.

A. The Stress and Displacement Fields

The displacement vector $\vec{u}$ of the elastic sphere can be written in spherical coordinates as

$$\vec{u} = u_r\vec{e}_r + u_\theta\vec{e}_\theta + u_\psi\vec{e}_\psi \ , \tag{29}$$

in which $u_\psi = 0$ because of symmetry. To get u_r and u_θ it is necessary to find $\vec{u}_L$ and $\vec{u}_{VS}$ in terms of the scalar potentials ϕ_L and ϕ_{VS}. In this problem the HS polarization does not arise because of the type of excitation. Therefore Eq. (25) becomes

$$\vec{u} = \vec{u}_L + \vec{u}_{VS} \ . \tag{25-a}$$

As mentioned before, the vector problem has been reduced to solving ϕ_L and ϕ_{VS} which satisfy scalar Helmholtz equations and appropriate boundary conditions at the solid-fluid interface. Similar to the solution for (Eq. (15)), ϕ_L and ϕ_{VS} are found as

$$\phi_L = \sum_{n=0}^{\infty} a_n j_n(k_L r)\, P_n(\cos\theta) \ , \qquad r \leq a \tag{30-a}$$

and

$$\phi_{VS} = \sum_{n=0}^{\infty} b_n j_n(k_T r)\, P_n(\cos\theta) \ , \qquad r \leq a$$

where a_n and b_n are unknown coefficients to be decided using

boundary conditions. The spherical Neumann function is eliminated to avoid the singularity at r = 0. Substituting (30-b) into (20-b) and (30-a) into (16) and using Eqs. (25-a) and (29) gives u_r, u_θ as

$$u_r = \sum_{n=0}^{\infty} \left[\frac{b_n}{r} n(n+1)\, j_n(k_T r)\, P_n(\cos\theta) + a_n \frac{d}{dr} j_n(k_L r)\, P_n(\cos\theta) \right] \tag{31}$$

$$u_\theta = \sum_{n=0}^{\infty} \left[\frac{a_n}{r} j_n(k_L r) \frac{d}{d\theta} P_n(\cos\theta) + b_n \frac{d}{dr} j_n(k_T r) \frac{d}{d\theta} P_n(\cos\theta) + \frac{b_n}{r} j_n(k_T r) \frac{d}{d\theta} P_n(\cos\theta) \right]$$

Only two components in the stress field are needed for the boundary conditions, namely σ_{rr} and $\sigma_{r\theta}$. In spherical coordinates σ_{rr} and $\sigma_{r\theta}$ are expressed as [10]

$$\sigma_{rr} = 2\rho_E c_T^2 \left(\frac{\lambda}{2\mu} \Delta + \frac{\partial u_r}{\partial r} \right)$$

$$\sigma_{r\theta} = \mu \left(\frac{\partial u_\theta}{\partial r} - \frac{u_\theta}{r} + \frac{1}{r} \frac{\partial u_r}{\partial \theta} \right), \tag{32}$$

where $\Delta = \nabla \cdot \vec{u}$ is the dilatation defined as the divergence of the displacement vector. One sees from Eqs. (19) and (30-a) that

$$\Delta = \nabla^2 \phi_L = - k_L^2 \sum_{n=0}^{\infty} a_n j_n(k_L r)\, P_n(\cos\theta) \tag{33}$$

Eqs. (31) and (32) are the required expressions for the displacement and stress fields. They are used to evaluate boundary conditions at the boundary between the fluid and elastic medium in the following section.

B. The Scattered Wave Solution

The boundary conditions applicable at the solid-fluid interface, $r = a$, are

1. Continuity of stress - the pressure in the fluid must be equal to minus the normal component of stress in the solid at the interface.
2. Continuity of normal displacement - the normal (radial) component of the displacement of the fluid must be equal to the normal component of the displacement of the solid at the interface.
3. Continuity of tangential stress - the tangential component of the shearing stress must vanish at the surface of the solid.

Expressing these in spherical coordinates gives

$$p_i + p_s = - \sigma_{rr} \qquad \text{at } r = a \tag{34}$$

$$u_{i,r} + u_{s,r} = u_r \qquad \text{at } r = a \tag{35}$$

$$\sigma_{r\theta} = 0 \qquad \text{at } r = a \ , \tag{36}$$

where the subscript r denotes radial direction.

The radial components of the displacement associated with the incident and scattered waves, after using Eq. (5), are found as

$$u_{i,r} = \left(\frac{1}{\rho_0 \omega^2} \right) \frac{\partial p_i}{\partial r}$$

$$= \frac{p_a}{\rho_0 \omega^2} \sum_{n=0}^{\infty} (2n+1) \, i^n \frac{d}{dr} j_n(kr) \, P_n(\cos \theta) \tag{37}$$

and

$$u_{s,r} = \left(\frac{1}{\rho_0 \omega^2}\right) \frac{\partial p_s}{\partial r}$$

$$= \frac{1}{\rho_0 \omega^2} \sum_{n=0}^{\infty} B_n \frac{d}{dr} h_n^{(2)}(kr)\, P_n(\cos\theta) \ . \qquad (38)$$

Upon substituting from Eqs. (26), (28), (31), (32), (33), (37) and (38), the boundary condition equations (34), (35) and (36) become, for the nth mode,

$$2\rho_E c_T^2 k_L^2 \left[\left(\frac{1}{2h_3^2} - 1\right) j_{n2} - j''_{n2}\right] a_n + 2\rho_E c_T^2 n(n+1)\,[j_{n3} - x_3\, j'_{n3}]\, b_n - a^2 h_{n1} = p_a a^2 (2n+1)\, i^n j_{n1} \qquad (34\text{-a})$$

$$x_2\, j'_{n2}\, a_n + n(n+1)\, j_{n3}\, b_n - \frac{x_1}{\rho_0 \omega^2} h'_{n1}\, B_n = \frac{x_1 p_a}{\rho_0 \omega^2} (2n+1)\, i^n j'_{n1} \qquad (35\text{-a})$$

$$[2\, x_2\, j'_{n2} - 2\, j_{n2}]\, a_n + [x_3^2\, j''_{n3} + (n^2+n-2)\, j_{n3}]\, b_n = 0 \ , \qquad (36\text{-a})$$

where, $x = kr$

$x_1 = ka$

$x_2 = k_L a$

$x_3 = k_T a$

$j_{n1} = j_n(x_1)$

$j_{n2} = j_n(x_2)$

$j_{n3} = j_n(x_3)$

$$h_{n1} = h_n^{(2)}(x_1)$$

$$j'_{n1} = \left.\frac{dj_n(k_L^T r)}{d(k_L^T r)}\right|_{r=a}$$

$$j''_{n2} = \left.\frac{d^2 j_n(k_L^T r)}{d(k_L^T r)}\right|_{r=a}$$

$$h'_{n1} = \left.\frac{dh_n^{(2)}(kr)}{d(kr)}\right|_{r=a}$$

$$h_3 = \frac{c_T}{c_L} \quad .$$

Solving Eqs. (34-a), (35-a) and (36-a) simultaneously for B_n by Cramer's rule gives:

$$B_n = \frac{1}{1+iC_n} p_a(2n+1)i^n \quad , \tag{39}$$

where

$$C_n = \frac{n_{n1}D - g\frac{X_1}{X_3^2} n'_{n1} E}{-j_{n1}D + g\frac{X_1}{X_3^2} j'_{n1} E}$$

$$n_{n1} = n_n(ka)$$

$$n'_{n1} = \left.\frac{dn_n(kr)}{d(kr)}\right|_{r=a}$$

$$g = \frac{\rho_E}{\rho_0}$$

$$D = 2n(n+1)\left[1 - \frac{j_{n2}}{x_2 j'_{n2}}\right] - \frac{x_3^2\, j''_{n3}}{j_{n3}} - (n^2+n-2)$$

$$E = 4n(n+1)\left[1 - \frac{j_{n2}}{x_2 j'_{n2}}\right]\left[1 - \frac{x_3 j'_{n3}}{j_{n3}}\right]$$

$$- 2x_2 \left\{\left[\frac{x_3^2\, j''_{n3}}{j_{n3}} + n^2+n-2\right]\left[\left[\frac{1}{2h_3^{\,2}} - 1\right]\frac{j_{n2}}{j'_{n2}} - \frac{j''_{n2}}{j'_{n2}}\right]\right\}$$

The solution for the scattered pressure p_s is found, by substituting (39) into (28), as

$$p_s = \sum_{n=0}^{\infty} \frac{p_a}{1+iC_n}(2n+1)i^n\, h_n^{(2)}(kr)\, P_n(\cos\theta) \ . \qquad (40)$$

At large distances from the sphere, i.e. $kr >> 1$, a simpler expression for the pressure of the scattered wave may be obtained by replacing $h_n^{(2)}(kr)$ by the following asymptotic expression:

$$h_n^{(2)}(kr) \sim \frac{1}{kr} e^{-i[kr - (n+1)\pi/2]} \ , \quad \text{as } kr \to \infty \qquad (41)$$

Substituting (41) in (40) gives

$$p_s \xrightarrow[kr>>1]{} \frac{p_a}{r} e^{-ikr} f(a,\theta) \qquad (42)$$

where $f(a,\theta)$ defined as the scattering function is

$$f(a,\theta) = \frac{1}{k} \sum_{n=0}^{\infty} \frac{(2n+1)(-1)^n\, i}{1 + i\, C_n} P_n(\cos\theta) \ . \qquad (42\text{-a})$$

One sees that the scattering function $F(a,\theta)$ depends on both the non-dimensional frequency ka (implicit in C_n) and the scattering angle θ.

It will be used extensively in Part II (Multiple Scattering Analysis) of this thesis.

C. Scattering Cross Section

The scattering energy is generally characterized by what is called the effective cross section (in some of the literature called the differential scattering cross section). The idea is that when an object or region scatters sound, some of the energy carried by the incident wave is dispersed. The energy lost to the incident wave is scattered radially or diffracted by the scatterer. The effective cross section is thus defined as the ratio of the scattered acoustic energy per unit solid angle in a given direction to the incident wave's intensity. The cross section has the units of an area. Mathematically it can be expressed as [13]:

$$d\sigma = \frac{I_s R^2 d\Omega}{I_i} , \tag{43}$$

where

$d\sigma$ = effective cross section

R = the distance between the center of the scatterer and the receiver

I_s = the scattered wave's intensity at the field point a distance R from the scatterer's center

$d\Omega$ = differential element of solid angle

I_i = the incident wave's intensity

The total effective cross section σ is the integral of $d\sigma$ over all directions of scattering, i.e., over the whole sphere representing a solid angle $\Omega = 4\pi$. It is the ratio of the total scattered intensity to the incident energy flux density and has the dimension of area.

$$\sigma = \frac{\int_0^{4\pi} I_s R^2 d\Omega}{I_i}$$

Since at long ranges $I_i = \frac{|p_i|^2}{\rho_0 c_0}$ and $I_s = \frac{|p_s|^2}{\rho_0 c_0}$ [13], Eq. (44) may be written in the following form:

$$\sigma = \frac{\int_0^{4\pi} |p_s|^2 R^2 d\Omega}{|p_i|^2} . \qquad (44\text{-a})$$

For spherical coordinates (refer to Figure 6), it is found that $\int_0^{4\pi} d\Omega = \int_0^{\pi} \sin\theta d\theta \int_0^{2\pi} d\psi$. For this coordinate system one obtains from (44-a),

$$\sigma = \frac{2\pi \int_0^{\pi} |p_s|^2 R^2 \sin\theta d\theta}{|p_i|^2} . \qquad (44\text{-b})$$

After substituting (42) into (44-c) and applying the following orthogonality condition of the Legendre polynomial [14]:

$$\int_0^{\pi} P_n(\cos\theta)\, P_m(\cos\theta)\, \sin\theta\, d\theta = \frac{2}{2n+1}\, \delta_{nm} ,$$

where δ_{nm} is the Kronecker delta, Eq. (44-b) becomes

$$\hat{\sigma} = \frac{4}{(ka)^2} \sum_{n=0}^{\infty} \frac{2n+1}{1+C_n^2} , \tag{44-c}$$

where $\hat{\sigma}$ is the nondimensional total scattering cross section obtained by dividing σ by the projected area of the sphere (πa^2).

In Part II of this thesis the total backscattered and forward scattered energy will be used in the energy flux calculation. Since the scattered energy is generally characterized by the scattering cross section, the expressions of the total backscattering and forward scattering cross section are also given.

The total backscattering cross section denoted as $\sigma+$ is

$$\sigma+ = \frac{2\pi \int_0^{\frac{\pi}{2}} |p_s|^2 R^2 \sin\theta d\theta}{|p_i|^2} , \tag{45}$$

which relates to the energy scattered at least partly upward $(0 \leq \theta \leq \frac{\pi}{2}$, see Figure 5). However, the energy scattered downward $(\frac{\pi}{2} \leq \theta \leq \pi)$ is described by the total forward scattering cross section which is

$$\sigma^- = \frac{2\pi \int_{\frac{\pi}{2}}^{\pi} |p_s|^2 R^2 \sin\theta d\theta}{|p_i|^2} . \tag{46}$$

The total scattering cross section σ is therefore the addition of the total backscattering cross section σ^+ and the total forward scattering cross section σ^-, i.e.

$$\sigma = \sigma^+ + \sigma^- . \tag{47}$$

The calculation for σ^+ and σ^- is rather complicated since the Legendre polynomial $P_n(\cos\theta)$ is not an orthogonal function in either interval, i.e., $\theta = 0$ to $\theta = \frac{\pi}{2}$ or $\theta = \frac{\pi}{2}$ to $\theta = \pi$. However, by letting $\hat{x} = \cos\theta$ and using the following formula obtained from the properties of the Legendre polynomial [15]:

$$\int_0^1 P_m(\hat{x})\, P_n(\hat{x})\, d\hat{x} = \begin{cases} \dfrac{-2}{\pi(n-m)(n+m+1)} \dfrac{\Gamma\left(\frac{m+1}{2}\right)\Gamma\left(\frac{n+2}{2}\right)}{\Gamma\left(\frac{n+1}{2}\right)\Gamma\left(\frac{m+2}{2}\right)}, & n = \text{odd},\ m = \text{even} \\ 0, & n,m = \text{even} \\ 0, & n,m = \text{odd} \quad (n \neq m) \\ \dfrac{1}{2n+1}, & n = m \end{cases}$$

where $\Gamma(\ )$ is the Gamma function whose properties are [14]:

$$\Gamma(1) = 1$$

$$\Gamma\left(\frac{1}{2}\right) \sim 1.77245$$

$$\Gamma\left(n + \frac{1}{2}\right) = \frac{1\cdot 3\cdot 5\cdots(2n-1)}{2^n}\,\Gamma\left(\frac{1}{2}\right)$$

$$\Gamma(n+1) = n!\ ,$$

one sees

$$\hat{\sigma}^+ = \frac{1}{(ka)^2}\left[\sum_{n=0}^{\infty} \frac{2n+1}{1+C_n^{\,2}} + \sum_{\substack{n,m=0 \\ n\ \text{even} \\ m\ \text{odd}}}^{\infty} \frac{2(2n+1)(2m+1)(1+C_nC_m)\,\Gamma\left(\frac{m+1}{2}\right)\Gamma\left(\frac{n+2}{2}\right)}{\pi(1+C_n^{\,2})(1+C_m^{\,2})(n-m)(n+m+1)\,\Gamma\left(\frac{n+1}{2}\right)\Gamma\left(\frac{m+2}{2}\right)}\right], \tag{45-a}$$

where $\hat{\sigma}^+ \left(= \frac{\sigma^+}{\pi a^2}\right)$ is the nondimensional total backscattering cross section.

The expression for the nondimensional total forward scattering cross section $\hat{\sigma}^-$ can thus be obtained by subtracting Eq. (45-a) from Eq. (44-c) as

$$\hat{\sigma}^- = \frac{1}{(ka)^2}\left[\sum_{n=0}^{\infty} \frac{3(2n+1)}{1+C_n^2} - \sum_{\substack{n,m=0 \\ n \text{ even} \\ m \text{ odd} \\ n \text{ odd} \\ m \text{ even}}} \frac{2(2n+1)(2m+1)(1+C_nC_m)\,\Gamma\left(\frac{m+1}{2}\right)\Gamma\left(\frac{n+2}{2}\right)}{\pi(1+C_n^2)(1+C_m^2)(n-m)(n+m+1)\,\Gamma\left(\frac{n+1}{2}\right)\Gamma\left(\frac{m+2}{2}\right)}\right] \tag{46-a}$$

D. Energy Consideration - Modal Reflection Coefficient and Forward Scattering Theorem

The total pressure field outside the nodule is

$$p_T = p_i + p_s \,. \tag{48}$$

Substituting Eqs. (26) and (40) into the above equation and using the definition for the Spherical Hankel function [14], i.e.

$$h_n^{(1)}(kr) = j_n(kr) + i\, n_n(kr)$$

$$h_n^{(2)}(kr) = j_n(kr) - i\, n_n(kr)$$

Eq. (48) then becomes

$$p_T = \frac{p_a}{2} \sum_{n=0}^{\infty} (2n+1) i^n P_n(\cos\theta) \left[h_n^{(1)}(kr) - \frac{1-iC_n}{1+iC_n} h_n^{(2)}(kr)\right] . \tag{48-a}$$

As kr approaches infinity, the asymptotic forms of the Spherical Hankel function of the 1st and 2nd kind are [14]

$$h_n^{(1)}(kr) \sim \frac{1}{kr} e^{i[kr-(n+1)\pi/2]}$$

$$h_n^{(2)}(kr) \sim \frac{1}{kr} e^{-i[kr-(n+1)\pi/2]} .$$

The far-field expression of p_T can thus be obtained, by substituting the above equations into Eq. (48-a), as

$$p_T \sim \frac{-i\, p_a}{2kr} \sum_{n=0}^{\infty} (2n+1)\, P_n(\cos\theta)\left[e^{ikr} + (-1)^n \frac{1 - i\, C_n}{1 + i\, C_n} e^{-ikr}\right] \tag{48-b}$$

One sees from Eq. (48-b) that p_T can be expressed as the combination of two components, one propagating inward and the other propagating outward. The first component (e^{ikr}) propagates inward. The other travels radially outward (e^{-ikr}) and may be interpreted as the reflected waves (see [12]). The ratio between the pressure amplitudes of the nth outgoing and incoming waves is defined as the modal reflection coefficient R_n which is

$$R_n = \frac{1 - i\, C_n}{1 + i\, C_n} . \tag{49}$$

From Eq. (39) C_n is known to be a real number for a nondissipative elastic scatterer. Therefore, the magnitude of R_n is unity which can be seen from the fact that R_n is a ratio between a pair of complex conjugates. This fact indicates that there is only a phase shift when the nth incoming wave is reflected from the nodule surface so no energy

is lost at the nodule surface.

At high frequencies the forward scattering sector forms the shadow zone, i.e. the total far-field pressure (Eq. (48-b) for $\theta = \pi$) is zero. A connection between the total power abstracted from the incident wave (the total scattering cross section) and the forward scattering function $f(a,\pi)$ (Eq. (42-a) for $\theta = \pi$) seems reasonable [12]. The relationship between each can be found by the following:

Recall Eq. (44) for the total scattering cross section. Evaluation of (44) for scattering from the elastic sphere gave, from Eq. (44-c),

$$\sigma = \frac{4\pi}{k^2} \sum_{n=0}^{\infty} \frac{2n+1}{1+C_n^2} \tag{44-d}$$

For forward scattering, i.e. $\theta = \pi$ in this case (see Figure 5), the scattering function $f(a,\theta)$ becomes, after substituting $\theta = \pi$ in Eq. (42-a) and separating the real and imaginary parts,

$$f(a,\pi) = \frac{1}{k} \sum \frac{C_n(2n+1)}{1+C_n^2} + \frac{i}{k} \sum \frac{(2n+1)}{1+C_n^2} , \tag{42-b}$$

where the Legendre polynomial for forward scattering reduce to [14]

$$P_n(-1) = (-1)^n .$$

From Eqs. (47-a) and (42-b) one sees that the forward scattering function $f(a,\pi)$ is related to the total scattering cross section σ as follows

$$\sigma = \frac{4\pi}{k} \mathrm{Im}[f(a,\pi)] , \tag{44-e}$$

where $\mathrm{Im}[f(a,\pi)]$ denotes the imaginary part of $f(a,\pi)$ in Eq. (42-b).

One may also relate the total scattering function σ to the modal reflection coefficient R_n. From Eq. (49)

$$\mathrm{Re}(R_n) = \frac{1 - C_n^2}{1 + C_n^2} \quad , \tag{49-a}$$

where $\mathrm{Re}(R_n)$ denotes the real part of R_n. The simple arithmetic gives

$$\frac{1}{1+C_n^2} = \frac{1}{2}\left(1 + \mathrm{Re}(R_n)\right) \quad . \tag{49-b}$$

After substituting Eq. (49-b) into (44-d) one sees that

$$\sigma = \frac{2\pi}{k^2} \sum_{n=0}^{\infty} (2n+1)(1+\mathrm{Re}(R_n)) \quad . \tag{44-f}$$

Comparing Eq. (44-f) with (44-e) the forward scattering function $f(a,\pi)$ can also be expressed, using the modal reflection coefficient R_n, as

$$\mathrm{Im}[f(a,\pi)] = \frac{1}{2k} \sum_{n=0}^{\infty} (2n+1)(1+\mathrm{Re}(R_n))$$

IV. SCATTERING RESULTS FOR SPECIAL CASES

The effect of an elastic sphere of dimensions small compared to a wavelength in a sound field is investigated. Both the radius of the sphere and incident wavelength enter into this so-called Rayleigh scattering in a simple power relationship. Scattering from spheres whose acoustic properties are near the surrounding fluid medium, i.e. fluid spheres without shear waves inside, is treated for all wave lengths. The solution for scattering by rigid, immovable spheres can also be obtained as a limiting case of fluid spheres.

A. Rayleigh Scattering (Long Wave Length - Asymptotic Result)

For scattering from an elastic solid sphere whose radius a becomes much less than the incident wavelength $\frac{2\pi}{k}$, i.e., $ka << 1$, both zeroth (monopole) and the first order (dipole) terms of the series solutions for p_s are important. By omitting higher order terms Eq. (42-a) is expanded as

$$f \xrightarrow[kr>>1]{} \frac{1}{k}\left[\frac{i}{1+iC_0} P_0(\cos\theta) - \frac{3i}{1+iC_1} P_1(\cos\theta)\right] \qquad (42\text{-c})$$

Eq. (42-c) can be further reduced, using $P_0(\cos\theta) = 1$ and $P_1(\cos\theta) = \cos\theta$, to:

$$f \xrightarrow[kr>>1]{} \frac{1}{k}\left[\frac{i}{1+iC_0} - \frac{3i}{1+iC_1}\cos\theta\right] \qquad (42\text{-d})$$

One sees that the first term on the right hand side of Eq. (42-d) relates to the monopole radiation and the second term generates dipole

radiation.

Substituting Eq. (42-d) into Eqs. (44-c), (45-b) and (46-b) one sees that

$$\hat{\sigma} = 4(ka)^4 \left(E_1^2 + \frac{1}{3} E_2^2\right) , \quad ka<<1 \tag{50}$$

$$\hat{\sigma}^+ = 2(ka)^4 \left(E_1^2 + E_1E_2 + \frac{1}{3} E_2^2\right) , \quad ka<<1 \tag{51}$$

$$\hat{\sigma}^- = 2(ka)^4 \left(E_1^2 - E_1E_2 + \frac{1}{3} E_2^2\right) , \quad ka<<1 \tag{52}$$

where $E_1 = \frac{1}{3} - \frac{1}{3e_1-4e_2}$

$$E_2 = \frac{g - 1}{2g + 1}$$

$$e_1 = g\left(\frac{c_L}{c_0}\right)^2$$

$$e_2 = g\left(\frac{c_T}{c_0}\right)^2$$

$$g = \frac{\rho_E}{\rho_0} .$$

Eqs. (50), (51) and (52) are respectively the expressions of nondimensional total scattering, backscattering, and forward scattering cross section for an elastic sphere in the Rayleigh region. All results are proportional to the fourth power of the nondimensional frequency, i.e. the ratio of the radius of the sphere to the incident wavelength. They can be further simplified, by taking $c_T = 0$, as

$$\hat{\sigma} = 4(ka)^4 \left(E_3^2 + \frac{1}{3} E_4^2\right) , \quad ka<<1 \tag{50-a}$$

$$\hat{\sigma}^{+} = 2(ka)^4 \left(E_3^2 + E_3E_4 + \frac{1}{3}E_4^2\right) , \quad ka<<1 \tag{51-a}$$

$$\hat{\sigma}^{-} = 2(ka)^4 \left(E_3^2 - E_3E_4 + \frac{1}{3}E_4^2\right) , \quad ka<<1 \tag{52-a}$$

where $E_3 = \frac{e_1-1}{3e_1}$ and $E_4 = \frac{g-1}{2g+1}$.

One sees from Eq. (50-a) that the zeroth order monopole term (the first term on the right hand side) is dependent only on the compressibility of the sphere and the first order dipole term (the second term on the right hand side) depends only on the density of the sphere. Eqs. (50-a), (51-a) and (52-a) are found to be the solutions for a fluid sphere in the Rayleigh region [17].

For very large e_1 (compressibility ratio) and g (density ratio), i.e. $e_1>>1$ and $g>>1$, Eqs. (51) and (52) may be converted to the Rayleigh region solutions for a rigid sphere [16]. Nondimensional total scattering, backscattering and forward scattering cross section for a rigid sphere are, from (50-a), (51-a) and (52-a), respectively

$$\hat{\sigma} = \frac{7}{9}(ka)^4 , \quad ka<<1 \tag{50-b}$$

$$\hat{\sigma}^{+} = \frac{13}{18}(ka)^4 , \quad ka<<1 \tag{51-b}$$

$$\hat{\sigma}^{-} = \frac{1}{18}(ka)^4 , \quad ka<<1 \tag{52-b}$$

B. Scattering from a Fluid Sphere, All Wavelengths

The same procedure used in solving the scattering problem for the elastic sphere is also applied to the fluid sphere. Instead of three boundary conditions, two boundary conditions in pressure and velocity fields are required since the fluid sphere cannot support a shear

stress. At the interface between the fluid sphere and the surrounding fluid two boundary conditions must be satisfied:

$$p_i + p_s = p_f \ , \quad \text{at } r = a \tag{53}$$

$$v_{i,r} + v_{s,r} = v_{f,r} \ , \quad \text{at } r = a \tag{54}$$

where p_f is the pressure inside the fluid sphere, and the subscript f denotes fluid sphere. p_i and p_s are given from Eqs. (26) and (28), respectively. p_f can be written as (see Eq. (30-a))

$$p_f = \sum_{n=0}^{\infty} D_n j_n(k_f r) \, P_n(\cos\theta) \ , \tag{55}$$

where D_n are unknown coefficients to be decided using (53) and (54) and k_f is the wave number for waves inside the fluid sphere.

$v_{i,r}$, $v_{s,r}$ and $v_{f,r}$ can be obtained by the following relationship which is from Eq. (5):

$$v_{(i,s,f),r} = \frac{1}{\rho_0 \omega^2} \frac{\partial p_{i,s,f}}{\partial r} \ .$$

Solving the simultaneous equations (53) and (54) for p_s, it is found that

$$p_s = p_a \sum_{n=0}^{\infty} \frac{i^n}{1+iC_{nf}} (2n+1) \, P_n(\cos\theta) \, h_n^{(2)}(kr) \ , \tag{56}$$

where

$$C_{nf} = \frac{j'_{nf} n_{nl} - n'_{nl} j_{nf} \, gh}{-j'_{nf} j_{nl} + j'_{nl} j_{nf} \, gh}$$

$$j_{nf} = j_n(k_f a)$$

$$j'_{nf} = \left.\frac{dj_n(k_f r)}{d(k_f r)}\right|_{r = a}$$

$$j_{nl} = j_n(ka)$$

$$j'_{nl} = \left.\frac{dj_n(kr)}{d(kr)}\right|_{r = a}$$

$$k_f = \frac{\omega}{c_f}$$

$$n_{nl} = n_n(ka)$$

$$n'_{nl} = \left.\frac{dn_n(kr)}{d(kr)}\right|_{r = a}$$

$$h = \frac{c_f}{c_0}$$

c_f = wave speed inside the fluid sphere.

Using Eq. (41) the pressure at a point far removed from the sphere is

$$p_s \xrightarrow[kr>>1]{} \frac{p_a}{kr} e^{ikr} \sum_{n=0}^{\infty} \frac{(-1)^n i}{1+iC_{nf}} (2n+1) P_n(\cos\theta) \qquad (56\text{-a})$$

One sees that both solutions of the scattering problem for elastic and fluid spheres have the same form except that they are different in the expressions for C_n and C_{nf}, i.e. $\hat{\sigma}$, $\hat{\sigma}^+$ and $\hat{\sigma}^-$ for fluid spheres can be obtained by changing C_{nf} for C_n in Eqs. (44-c), (45-a) and (46-a), respectively.

C. Scattering from a Fixed Rigid Sphere

It is of interest to obtain a limiting case for a sphere of radius a with density and sound speed ratios approaching infinity ($g,h \to \infty$). In this case C_{nf} reduces to $\frac{-n'_{nl}}{j'_{nl}}$ and the nondimensional total scattering, backscattering and forward scattering cross sections are found by substituting this reduced C_{nf} into Eqs. (44-c), (45-a) and (46-a) for C_n, respectively.

V. COMPARISON OF RESULTS WITH PREVIOUS INVESTIGATORS

The equations derived in Chapter III in solving the scattering problem of an elastic sphere are used to obtain the numerical data in this chapter. The computation of total scattering cross sections of fluid and fixed rigid spheres (special cases of the elastic sphere) and the calculation of the backscattering reflectivity factor for the elastic sphere are presented. The results are compared with computations of previous investigators and show a good agreement. The comparisons are carried out to ensure that the computer programs used to implement those equations in Chapter III are valid.

A. The Total Scattering Cross Sections of Fluid Spheres

Calculations of nondimensional total scattering cross sections for fluid spheres of different density ratio g and different compressibility ratio h have been made by Anderson [6]. Nondimensional total scattering cross sections were calculated using Eq. (44-c) where C_{nf} in Eq. (56) was used in place of C_n.

One sphere has values of $g = 1.0$ and $h = 1.2$. The other has both g and h equal to 0.5. The calculation was also made using the reduced C_{nf} which is $\frac{-n'_{nl}}{j_{nl}}$ for C_n in Eq. (47) for a fixed rigid sphere. The results are presented as plots of $\hat{\sigma}$ vs. ka in Figures 7, 8, and 9.

Anderson's results are limited to the frequency range $0 \leq ka \leq 6$. However by using a computer the frequency range can be extended. In calculating $\hat{\sigma}$ the first five terms in the series (Eq. (44-c)) were used in the frequency range $0 \leq ka \leq 1.0$ (Rayleigh region). Twenty terms

were used in the range $1.0 < ka \leq 10$, and sixty terms were used in the range $10 < ka \leq 30$. The higher order terms in the expression for C_{nf} become more and more important in the higher frequency ranges and in different frequency ranges the series solution for $\hat{\sigma}$ can be truncated at different number terms, i.e. more terms than required used in calculation will give the result with an accuracy up to eight decimal places. Anderson's results are also plotted on Figures 7, 8, and 9 for comparison. One sees that in the frequency range $0 \leq ka \leq 6$ the results match well. A fluid sphere of small g and h (usually less than one) is highly resonant, i.e. many peaks of $\hat{\sigma}$ appear at various values of ka which are nondimensional resonant frequencies (see Figure 9). However, the resonances do not appear for the hard (large g and h) fluid sphere (see Figures 7 and 8).

B. Reflectivity Factors of the Elastic Spheres

Anderson presented part of his results using a reflectivity factor (also known as the form function [17]) which is defined in notation of this report as

$$R_\theta = \frac{2|f|}{a} \tag{57}$$

Calculations of the reflectivity factor at $\theta = 0$ (backscatter) have been made by Hickling [8] using Faran's analysis [7] for elastic spheres.

In reference [8] results are provided as plots of $R_{\theta=0}$ denoted as f_∞ in [8], versus the nondimensional incident wave frequency ka. The expression for backscattering reflectivity factor $R_{\theta=0}$, after substituting Eq. (42) into (57), becomes

$$R_{\theta=0} = \frac{2}{a}|f(a,0)| \qquad (58)$$

The reflectivity factor $R_{\theta=0}$ can thus be computed from Eq. (58) by taking sufficient terms using a computer.

The backscattering reflectivity factors were calculated using Eq. (58) for armco iron and beryllium sphere whose properties are shown in Table 1. The fluid outside the sphere was assumed to be water of density 1 g /cc and compressional velocity 1410 m/sec. The results are compared with those of Hickling. Again in calculating $R_{\theta=0}$ five terms, twenty terms and sixty terms were used in the frequency ranges $0 \leq ka \leq 1$, $1 < ka \leq 10$, and $10 < ka \leq 30$ respectively. The results are presented as plots of $R_{\theta=0}$ vs. ka in Figures 10 and 11. These results accurately duplicate Hickling's [8] Figures 3 and 5 which appear in Figure 12 of this thesis. The plot of $R_{\theta=0}$ vs. ka is also presented for a rigid sphere (see Figure 13).

The results obtained in sections A and B of this chapter agree well with the computations made by previous investigators. Thus the computer program used to implement the equations in Chapter III seems valid. The solutions for the scattering problem of a manganese nodule using these programs are presented in the following chapter.

VI. RESULTS AND DISCUSSION

A. Computations for Manganese Nodules

Numerical values of the wave propagation speeds of manganese nodules are required in order to quantify the results. Values for the compressional and shear wave speeds of manganese nodules do not appear in the literature since only the mineralogical properties of nodules are usually the topics of interest. However, samples of manganese nodules and slab material donated by Deep Sea Ventures, Inc. have been analyzed recently at Virginia Tech. The wave speeds in manganese nodules from Atlantic and Pacific Ocean basins were measured by Smith [18]. The ranges of c_L and c_T for nodules in the wet condition are shown in Table 2. It is found that the ratio of c_T over c_L, i.e., h_3, for wet Pacific nodules is generally larger than that for wet Atlantic ones. Also this is true for the wet density ratio. Generally speaking, the wet specific gravities for nodules from both oceans are in the range of 1.9 to 2.0 which is higher than Gladsby's result [19], but is close to Greenslate's data [20]. One also sees that the compressional wave speeds (c_L) are always larger than shear wave speeds (c_T), as would be expected in an elastic medium (see Eqs. (11) and (12)).

Nodules from the Pacific Ocean are of prime interest for this thesis because of their potential for future mining operations. The ratios of c_L over c_0, c_T over c_0 and the density ratio g of the Pacific nodules are required in obtaining quantitative results for the scattering from manganese nodules. Values of c_L/c_0, c_T/c_0 and g used in the

calculations are 1.70, 1.57 and 1.94 respectively. Values of c_L, c_T and the density of wet Pacific nodules were taken from Table 2. A salt water density (ρ_0) of 1.03 g /cc and sound speed in salt water (c_0) of 1500 m/sec were used in obtaining these ratios. For comparison and to show the different effects of both nodule shear waves and density in the high frequency and Rayleigh regions, i.e., sensitivity test, another sets of c_L/c_0, c_T/c_0 and g were also used in the computations (see Table 3).

Results for this specific scattering problem of manganese nodules from the Pacific Ocean are shown in Figures 14 and 15. Figure 14 shows the relationship between the nondimensional total scattering cross section $\hat{\sigma}$ and the nondimensional frequency ka of the Pacific nodules. In computing this, Eqs. (39) and (44-c) were used. One sees from this log-log plot that up to ka equal to 0.4 the curve is a straight line whose slope is about 4.0. This means that in the range $0 \leq ka \leq 0.4$ $\hat{\sigma}$ is proportional to $(ka)^{4.0}$ for scattering from a single spherical Pacific nodule. The value of $\hat{\sigma}$ increases with increasing ka until $\hat{\sigma}$ reaches its first local maximum value of 7.48. The corresponding ka is 2.30. In the range $0.4 < ka \leq 2.30$ the curve cannot be described by a simple power relationship between $\hat{\sigma}$ and ka because more and more higher order terms come in the series solution for $\hat{\sigma}$ after ka leaves the Rayleigh region. For ka>>1, high frequency effects dominate and the nodule obeys a geometrical scattering. In other words, when the radius of the nodule is very large compared to the incident wave length, geometrical scattering phenomena occur. This can be seen from the small fluctuation of $\hat{\sigma}$ with respect to ka where $\hat{\sigma}$ approaches a constant

value for the larger ka cases in Figure 14.

The relationship between the backscatter reflectivity factor $R_{\theta=0}$ of the Pacific nodule and ka is shown in Figure 15. One sees many peaks and troughs for the backscattering (internal resonance, detail later). The value of $R_{\theta=0}$ increases rapidly from 1.15 to 8.11 in the narrow frequency range of $1.5 \leq ka \leq 2.2$. Resonant frequencies do not happen in the Rayleigh region ($ka \ll 1$) and the magnitude of $R_{\theta=0}$ is much smaller than that in the high frequency region.

Figure 16 compares the results of a Pacific nodule and the same nodule with the shear wave speed c_T set to zero (fluid sphere case). One sees that the major differences in shape occur at the higher frequencies ($ka > 1$). The Pacific nodule has higher values of $\hat{\sigma}$ in the range $1 \leq ka \leq 12$. From the Rayleigh region up to $ka = 1$, the two curves are parallel to each other and the nodule always has higher values of $\hat{\sigma}$.

For two nodules differing only in density ratio g Figure 17 gives the comparison. Although there are differences of $\hat{\sigma}$ in both the high frequency and Rayleigh regions, the changes in the region $ka > 4$ are very small and can be neglected. The first local maximum of $\hat{\sigma}$ appears at a larger ka for the nodule with g equals 1.4 (the wet density ratio was taken as 1.4 by Gladsby [19]). Two curves in the Rayleigh region are parallel up to $ka = 1$. However the nodule with $g = 1.4$ has the higher $\hat{\sigma}$ in this region. The density ratio g apparently affects the low frequency region and for large ka the change in g does not vary the total scattering cross section significantly.

The effect of a change in shear wave speed c_T on $\hat{\sigma}$ is shown in Figure 18. In the low frequency region, ka < 1, two curves are parallel to each other and the nodule with $c_T/c_0 = 1.2$ has much lower values of $\hat{\sigma}$ in the region. The resonance of $\hat{\sigma}$ does not occur for the lower value of c_T. Generally speaking, in the high frequency range the nodule with a higher c_T/c_0 ratio gives smaller values of $\hat{\sigma}$. This is probably due to the constraint from the higher rigidity. In the low frequency region the scattering is dominated by the rigidity and this can also be seen from Figure 16 where the fluid sphere has zero rigidity.

The polar plots of the reflectivity R_θ vs. θ for the rigid sphere of ka = 0.01, 2 and 8 are shown in Figures 19, 20 and 21 which are in good agreement with Stenzel's results [21]. The calculation of the reflectivity for nodules has also been done for ka = 0.01, 2 and 8 and presented as plots of R_θ vs. θ shown in Figures 22, 23 and 24. In the high frequency region the forward scattering will form the shadow. However one sees in both cases (rigid and elastic spheres) the back-scattering is eminent in the Rayleigh region. The scattering strength in both cases has more fluctuations in directions in the high frequency region than in the low frequency region.

B. Free Vibration Analysis of Single Nodule

As can be seen from Figures 10, 11 and 15 of $R_{\theta=0}$ vs. ka for Beryllium and Armco spheres as well as for a single nodule, there is a strongly fluctuating behavior for sound scattering from elastic bodies at moderate to large ka characterized by sharp spikes. Calculations from

previous investigators showed close correspondence between frequencies of the free vibration of the elastic sphere in vacuum and the frequencies (i.e., ka) at which the minima occur in $R_{\theta=0}$ (see [7], [17] and [22]).

In practice, the measurement for both shear and longitudinal wave velocities of manganese nodules was under some experimental error (within a certain range). The free vibration analysis of the elastic sphere in vacuum can thus serve as a guide to check the error. In other words, the sound velocities in nodules can be best estimated until the computed free vibration frequencies of the nodule best corresponded to the experimental minima of $R_{\theta=0}$. As noted by Faran [7], there is usually a shift between the position of a minimum on $R_{\theta=0}$ and the free vibration frequency of the elastic sphere. However, for a nondissipative sphere with the density much larger than that of the surrounding fluid, the frequency shift is small pointed out also by him. For the nodule, the density ratio g is 1.94 and is not so large that one should expect a moderate frequency shift when doing such a comparison.

Some literature shows that successive minima appearing in the plots of $R_{\theta=0}$ vs. ka are caused by a coincidence of the speeds of various elastic-type creeping waves (regge poles) with the phase velocities of various normal mode vibrations of the scattering body (see [22] and [23]). Since the scattered pressure field is obtained by means of a modal series (see Eq. (40)), it is convenient to study the properties of the individual normal mode rather than to do the creeping wave analysis. However, it is not to be discussed further in this thesis.

C. Absorption Analysis of Single Nodule

Experimental measurements of the backscattering response (e.g. $R_{\theta=0}$) from solid metal spheres in water show excellent agreement with those calculated from the elastic theory (see [17] and [24]). These results demonstrate that ignoring absorption effects is a very good assumption for metals.

Grubb [25] did some acoustic measurements for manganese nodules (due to the limitation of the testing facility tiny nodules of about 1/10 inch diameter were used). Results from Grubb are not conclusive because many experimental flaws associated with the preliminary testing set-ups. However, there was some indication that the acoustic dissipation may be presented in the nodule material seeing from the comparison between the measured R_θ vs. ka and that calculated from the analytical formula.

As mentioned before, manganese nodules are porous. Therefore, nodule pores are filled with fluid which may introduce dissipation. This suggests that a modification of the present elastic sphere model to include the effects of the absorption on shear and compressional waves in manganese nodules should be established.

Biot [26] investigated the propagation of elastic waves in a fluid-saturated porous solid in great details and established a general theory to solve the related problems. However, in doing the calculation the dissipation arising from the porosity can be obtained by using complex wave numbers into the elastic theory (see [27]). The complex compressional and shear wave numbers k_L' and k_T' are given by

$$k_L'a = (ka)\frac{c_0}{c_L} - ika\frac{c_0}{c_L}\beta_L$$

$$k_T'a = (ka)\frac{c_0}{c_T} - ika\frac{c_0}{c_T}\beta_T \quad , \tag{59}$$

where β_L and β_T are absorption factors which may be obtained using Biot's theory [26] or obtained experimentally (see [28]).

The computations of the backscattering response (e.g. $R_{\theta=0}$) for absorbing spheres can be done using Eq. (58). However, the elements of C_n (in Eq. (39)) containing spherical Bessel functions will now have complex arguments. Since no tabulation of Bessel functions with complex arguments are available, an alternative method will be considered. Vogt et al [27] redefined those Bessel functions in terms of the hypergeometric function together with its properties to calculate the backscattering response of a plane wave from a lucite sphere (i.e. an absorbing sphere) using the computer. Their results show a good agreement between the model modified with the absorption and the transient wave measurement.

The method employed by Vogt et al [27] will thus serve as a guide in the modification of the present elastic theory in which the nodule is modeled as a nonabsorbing elastic sphere. However, the detailed calculation for the porous nodule is beyond the scope of this work. The absorption factors β_L and β_S for nodule materials must be known before computations can be carried out.

D. Summary

The results expressed as plots of nondimensional scattering cross section ($\hat{\sigma}$) versus nondimensional frequency (ka) for a nodule modeled as an elastic solid sphere represent the nodule's "acoustic signature." The specific "acoustic signature" of the Pacific nodule can be used to distinguish nodule deposits from acoustic returns from other bottom types.

The scattered acoustic signal from the nodule is, in general, a function of the incident wave's frequency. For very low frequencies (Rayleigh scattering) the wave length is much larger than the nodule radius, i.e. $ka \ll 1$, and the scattered wave varies from the fourth power of the frequency. This can be easily seen from plots (Figures 13-18) in the low frequency range ($0.15 \leq ka \leq 1$). The density ratio g dominates the magnitude of scattering cross section in the low frequency region. However, all curves in the low frequency region are parallel to each other and have similar slopes on the log-log plots (slope 4 for $ka \ll 1$ according to Rayleigh [5]).

In the high frequency region ($ka > 1$), the nodule's shear wave speed (rigidity) becomes important. The rigidity will give a larger response for an elastic sphere than for a fluid sphere in the high frequency range. This can be seen from Figure 16. The maximum $\hat{\sigma}$ for the Pacific nodule is found, from Figure 13, to be about 7.48 corresponding to a frequency range of 17 to 27 kHz for nodules around 5 to 8 cm in diameter. The audible frequency range from 5.6 to 9 kHz corresponds to a ka of 1.0 for the 5 to 8 cm diameter nodules.

It is well known that nodule material is a porous solid [20]. Porosity may produce viscoelastic effects. The elastic model presented here can be generalized to include viscoelastic effects due to porosity using Biot's [26] models or modifications. This modeling work should be conducted parallel with experimental laboratory work on measuring loss mechanisms in wave propagation in nodule material.

For the single scattering problem interaction between the ocean bottom and the nodule has been ignored. The mud sediment in which the nodules rest is known to be relatively transparent acoustically. To take into account the presence of the ocean bottom is a difficult mathematical boundary value problem. A closed form analytical solution is probably impossible because one cannot express the boundary conditions on both the sphere and the ocean bottom interface in a simple way using one coordinate system. However, a combined analytical finite element technique based on the work of Venderborck and Rumelhard [29] can be developed in solving this problem.

PART TWO

ANALYSIS OF MULTIPLE SCATTERING FOR MANGANESE NODULES

VII. INTRODUCTION, Part 2

The multiple scattering of waves by randomly distributed scatterers has been studied in the literature. As early as 1945 Foldy [30] has applied a self-consistent method to obtain the index of refraction for scalar waves traveling in a medium of random, isotropic scatterers.

Later in 1951 Lax [31,39] extended the self-consistent method to the anisotropic scattering in addition to the monopole and dipole case and also gave a detailed review of multiple scattering of waves. The highlight lies in the discussion of the effective scattering field in dense systems, i.e., where scatterers are crowdedly distributed in space. The quasi-crystalline approximation was suggested to simplify the averaging process.

Twersky [33,38,41,42,43] has done extensive work in the multiple scattering of waves from volumetric and planar arrangements of scatterers. As expected physically, Twersky [43] shows that the average scattered wave, from a planar arrangement of scatterers excited by an incident plane wave, is also a plane wave characterized by an equivalent reflection or transmission coefficient.

Ishimaru [37] interpreted Foldy, Twersky and other previous investigators' work and used the consistent set of integral equations to explain various processes of multiple scattering. The multiple scattering problem can therefore be divided into two general categories: (1) for a sparse distribution of scatterers, the single scattering analysis is good enough in evaluating the average scattered field. However, (2) for a dense distribution of scatterers, the pair correlation

appeared in the second equation of the Foldy-Lax hierarchy is required to obtain more accurate scattering results.

The present problem is the investigation of the acoustic wave scattering from randomly distributed nodules on a plane, i.e. sea floor. In order to make the randomness tractable, statistical quantities such as the area number density, the nodule size distribution statistics and the radial distribution characteristics of nodules are required. A statistical description of the manganese nodule deposit is given in Chapter VIII where the configurational average [30] is introduced.

Chapter IX begins with the statement of the multiple scattering problem and ends with all the formulations which will be used in the later analysis and calculations. Then to make the scattering processes physically understandable the orders of scattering are explained and the concept of the coherent and incoherent fields are also presented.

The sound source with relatively narrow beam widths is particularly important in the deep ocean sounding environment. A Gaussian beam form acoustic wave as a spherical type sound source is investigated in Chapter X. The effect of the beam width on the average backscattered wave field is examined. The result is used to verify the validity of the plane wave excitation for the multiple scattering problem.

Sumitomo Metal Mining Company of Tokyo, Japan, has recently developed and is now marketing a sounding equipment for exploring deep sea manganese nodules. Chapter XI is therefore a review of Sumitomo's work and describes their idealized scattering model which is shown to be complementary to the present study. Sumitomo's system requires at-sea calibration and the present analysis shows why this is necessary.

In Chapter XII the configurational averages for the wave function, wave intensity and energy flux are derived for a sparse distribution of nodules excited by a normally incident plane wave. The equivalent reflection and transmission coefficient are obtained which are functions of the incident wave frequency and the forward and backward scattering characteristics for a single nodule. The energy principle is verified for the single scattering case where higher order terms are small and can be neglected. A simple step function representing a radial distribution function is used in finding its effect on the average scattered field and serves as a guide for future study.

VIII. STATISTICAL DESCRIPTION OF MANGANESE NODULE DEPOSIT

In order to analyze the acoustic waves which are scattered by a randomly planar distribution of scatterers, i.e. for the present case nodules on the ocean floor, it is necessary to know the statistical description of nodule deposits. One usually characterizes scattering from random distributions of scatterers by the ensemble average of the relevant physical quantities (e.g. wave function itself) as presented by Foldy [30].

From a similar statistical analysis one finds that the incident wave and the scattered waves combine on the average to form a specularly reflected wave which indicates the presence and the amount of scatterers [31]. One is therefore, instead of investigating one particular bottom configuration of nodule deposits, interested in the statistical measures of all possible bottom configurations of nodule deposits.

The statistical picture of the ocean floor covered with nodules can be described by three relevant nodule distribution characteristics: the area number density, the distribution of nodule sizes and the spatial distribution of nodule locations. They will be investigated in detail in this chapter.

A. Nodule Size Statistics

Photographs of manganese nodule deposits on the ocean floor (see Figure 25) give valuable statistical information relevant to the

detection and identification of the nodule deposits. In a related investigation at Virginia Tech, Smith [18] measured the apparent area of nodules and determined the center location of each nodule of several central Pacific nodule deposit photographs provided by Deep Sea Ventures Inc.

The number of nodules per unit bottom area (the area number density ρ) was determined by counting the nodules on a bottom photograph in a known bottom area. This statistical quantity gives a lowest order spacing statistical information about nodule deposits. For a sparse distribution of nodules this information, i.e. ρ, and the size distribution are sufficient to evaluate the magnitude of the average scattered response (details later).

The apparent projected area of each nodule was measured with a planimeter from enlarged photographs which are properly scaled. In making an abundance estimate from bottom photographs, as pointed out by Felix [32], both the number and the total apparent projected area of nodules may be greatly underestimated. By comparison with box coring data it was found that in some instances the nodule abundance taken from bottom photos was approximately 50 to 75 percent of the true abundance attributed to partial or complete coverage of some nodules by a thin layer of sediment. However, Felix's observations were based only on a small area of the North Pacific nodule belt and might be valid for some locations but not for all. For example, the bottom photograph of nodules appeared in Figure 2 does not suffer from this effect. The photographs used in Smith's analysis were clear and the apparent size of each nodule was carefully examined and approximated so that the blanket effect was

minimized to the lowest extent. Some of Smith's results were also derived from box core samples published by McFarland [49]. Therefore Smith's results are in general expected to be adequate in the estimation. As a matter of fact, under the acoustic sounding the surface-sediment layer is relatively transparent to the sound wave and acoustic measurements would not suffer from the blanket effect as photographic measurements might.

Since the nodules were modeled as spheres, the apparent radius a_j of each nodule was defined as the square root of the apparent projected area A_j by dividing by π:

$$a_j = \sqrt{A_j/\pi} \quad .$$

Therefore the average of any power, m, of the radii may be calculated directly from the data for N nodules by the following relation:

$$\overline{a^m} = (1/N) \sum_{j=1}^{N} (a_j)^m \quad ,$$

in which the overbar represents the arithmatic average. However, it is more convenient to describe the size statistics by a probability density function $q(a^m)$ so that

$$\overline{a^m} = \int_0^\infty q(a^m) a^m \, da^m \quad . \tag{60}$$

From the photograph analysis Smith found that the radius squared distribution histograms (see Figure 26 for example) were well approximated by the Rayleigh distribution curve for the radius squared distribution given as

$$q(a^2) = (a^2/b^2)\ \mathrm{Exp}\ (-a^4/2b^2)\ . \qquad (61)$$

For the curve fit the Rayleigh parameter b was obtained by matching $\overline{a^2} = \sqrt{\pi/2}\ b$ (derived from Eq. (60) for m = 2) of the Rayleigh distribution function to the photograph analyzed value of $\overline{a^2}$ of the histogram.

Consequently an expression relating the probability densities for different powers of the apparent radius a was obtained by Smith as

$$q(a^m) = (2a^{4-m}/mb^2)\ \mathrm{Exp}\ (-a^4/2b^2)\ . \qquad (61\text{-}a)$$

One sees that the relationship between the averages of different powers of the apparent radius, i.e. $\overline{a^m}$, and the Rayleigh size distribution parameter b can thus be obtained using Eqs. (60) and (61-a). One complete statistical bottom data set was computed from Smith's photograph analysis in which $\overline{a^2} = 9.3\ cm^2$ and summarized as Table 4.

B. Spatial Distribution of Manganese Nodule Deposit

In sparsely distributed nodule fields nodules are assumed to be spaced far enough apart so that the probable location of each nodule is independent of the locations of the others. As mentioned previously, the lowest order statistical quantity ρ and the size distribution can best describe the bottom configuration. However, in dense packing nodule fields the separation distance statistics becomes important because the joint statistics cannot be ignored (see Twersky [33]). Therefore, the higher order spacing statistics between any two nodules needs to be considered in the multiple scattering analysis. On the ocean floor covered by crowded nodules the location of each nodule is not independent any more but is constrained by the positions of

adjoining nodules.

Smith [18] did the analysis for the locational relationship between pairs of nodules in manganese nodule fields using bottom photos. Smith calculated the distances between nodules in photographs. The resulting data set of distances was grouped in equal distance intervals and the number of nodules in each distance group was counted. Geometrically, the distance intervals represent rings of bottom area about each nodule. Since the ring area increases proportionally with the distance from each nodule, the number in each distance group would be expected to be the same. The geometrically expected variation is eliminated by dividing the number in the distance group by the distance and the product is represented as a bar graph versus the distance. One example shown in Figure 27 was calculated from one bottom photograph that had a reference length scale.

The bar graph represents the pair relationship between two nodules through the normalized radial distribution function f(R). Similar radial distribution functions were numerically generated by Hong [34] using the Perius-Yevick equation of liquid physics (see Croxton [35]) to describe the spatial correlation between the particles. Although Hong approximated his crowded monolayer of spheres to be a mixture of three sizes (or species) of spheres, his theoretical results are still in good agreement with the experimental data. Hong's spatial correlation between spheres considered both size and location. Since the spheres of the same size can be grouped together in his analysis, the location and the size statistics are interdependent. In Smith's analysis sizes are not accounted for in the pair correlation between nodules as the

analysis has assumed they are independent for convenience.

One sees from Figure 27 that since there is little chance that nodules lie on top of each other thus at small distances there is an exclusion region where the radial distribution function f(R) ~ 0 and the adjacent nodules are exhibited by the first peak, i.e. f(R) > 1. However, each adjacent nodule also has its own exclusion region and somewhat shields the original center nodule from its next nearest neighbors. Hence a valley on the graph (f(R) < 1) appears. This correlation of the nodule locations decreases with increasing distance until at large distances, i.e. the jth nodule is located in a region far away from the kth nodule, the relative location of the jkth pair is very weakly correlated and can be considered to be uncorrelated. This may be observed from the graph; as R increases f(R) asymptotically approaches unity, i.e. uncorrelated.

C. Configurational Average of the Nodule Field

Since all nodules do not have identical scattering properties (they are random in almost all aspects) it is assumed that the scattering properties of the jth nodule are determined by a single scalar scattering parameter denoted by s_j. Physically speaking, the scattering parameter s_j depends on the physical and geometrical characteristics of the jth nodule. To find such a dependence is beyond the scope of this study. However, according to the single nodule scattering analysis it is reasonably assumed that the scattering parameter s_j can be represented by the acoustic properties, i.e. the radius a, the density ratio g and the sound speed ratios c_L/c_0 and c_T/c_0, of the jth nodule.

If there is a collection of N nodules lying on the bottom and the position $\vec{r}_j(x_j,y_j,0)$ and scattering parameter s_j are given for each then one particular configuration of the nodule fields is defined. However, for the problem of multiple scattering of waves by the nodule fields one is interested in the statistical average taken over the ensemble of all possible bottom configurations of nodule deposits, i.e. all possible arrangements of $\vec{r}_j$ and s_j for $j = 1,2,\ldots,N$.

Since nodules are statistically distributed on the ocean bottom, an ensemble of configurations of nodule deposits can be characterized by a joint probability distribution function of $\vec{r}_j$ and s_j which is

$$P = P(\vec{r}_1,\vec{r}_2,\ldots,\vec{r}_N\ ;s_1,s_2,\ldots,s_N)\ . \tag{63}$$

The distribution (63) specifies the probability that the first nodule lies in the element of area $d\vec{r}_1$ about the position $\vec{r}_1$ and has a scattering parameter lying between s_1 and $s_1 + ds_1$. Similarly the second nodule lies in the element of area $d\vec{r}_2$ about the position $\vec{r}_2$ and has a scattering parameter lying between s_2 and $s_2 + ds_2$, etc. The probability of finding such a nodule field can thus be represented as

$$P d\vec{r}_1 d\vec{r}_2 \ldots d\vec{r}_N\ ds_1 ds_2 \ldots ds_N$$

By introducing a random scalar function F which is a function of the $\vec{r}_j$'s and s_j's, i.e. $F = F(\vec{r}_1,\vec{r}_2,\ldots,\vec{r}_N\ ;s_1,s_2,\ldots,s_N)$, the configurational average of F, which may be a physical quantity (e.g. pressure or energy flux), over the ensemble of configurations can be given in terms of P following Foldy [30]:

$$\langle F \rangle = \int_{2N} \ldots \int F\ P d\vec{r}_1 d\vec{r}_2 \ldots d\vec{r}_N\ ds_1 ds_2 \ldots ds_N \tag{64}$$

The conditional joint probability distribution function $P(\vec{r}_1,\vec{r}_2,\ldots,\vec{r}_{N-1};\ s_1,s_2,\ldots,s_{N-1}\ /\ \vec{r}_j;s_j)$ which is useful in the averaging process represents the probability of finding the N-1 nodules located at the appropriate intervals of $\vec{r} + d\vec{r}$ with the scattering parameters s + ds when the jth nodule is at the fixed position $\vec{r}_j$ with the scattering parameter s_j. In the same manner the conditional joint probability distribution function

$$P(\vec{r}_1,\vec{r}_2,\ldots,\vec{r}_{N-2};\ s_1,s_2,\ldots s_{N-2}\ /\ \vec{r}_j,\vec{r}_k;\ s_j,s_k)$$

which represents two nodules held fixed and

$$P(\vec{r}_1,\vec{r}_2,\ldots,\vec{r}_{N-3};\ s_1,s_2,\ldots,s_{N-3}\ /\ \vec{r}_j,\vec{r}_k,\vec{r}_\ell;\ s_j,s_k,s_\ell)$$

has three fixed, etc.

According to the law for the conditional probability [36], one sees,

$$P(\vec{r}_1,\vec{r}_2,\ldots,\vec{r}_N;\ s_1,s_2,\ldots,s_N) = P_j(\vec{r}_j;s_j)\ P(\vec{r}_1,\vec{r}_2,\ldots,\vec{r}_{N-1};\ s_1,s_2,\ldots,s_{N-1}\ /\ \vec{r}_j;s_j)\ ,$$

$$P(\vec{r}_1,\vec{r}_2,\ldots,\vec{r}_N;\ s_1,s_2,\ldots,s_N) = P_{jk}(\vec{r}_j,\vec{r}_k;\ s_j,s_k)\ P(\vec{r}_1,\vec{r}_2,\ldots,\vec{r}_{N-2};\ s_1,s_2,\ldots,s_{N-2}\ /\ \vec{r}_j,\vec{r}_k;\ s_j,s_k)\ ,$$

$$P(\vec{r}_1,\vec{r}_2,\ldots,\vec{r}_N;\ s_1,s_2,\ldots,s_N) = P_{jk\ell}(\vec{r}_j,\vec{r}_k,\vec{r}_\ell;\ s_j,s_k,s_\ell)\ P(\vec{r}_1,\vec{r}_2,\ldots,\vec{r}_{N-3};\ s_1,s_2,\ldots,s_{N-3}\ /\ \vec{r}_j,\vec{r}_k,\vec{r}_\ell;\ s_j,s_k,s_\ell)\ ,$$

$$\text{etc.}\ , \qquad (65)$$

where $P(\vec{r}_j;s_j)$ is the probability of the nodule occurring between $\vec{r}_j$ and $d\vec{r}_j$ with scattering parameter between s_j and ds_j, and $P(\vec{r}_j,\vec{r}_k;\ s_j,s_k)$ is the probability of the jth and kth nodules occurring simultaneously as specified, etc.

The conditional configurational average of a random function F over the ensemble of configurations of N-1 nodules holding the jth nodule fixed with the scattering parameter s_j can thus be defined in terms of the conditional joint probability distribution function $P(\vec{r}_1,\vec{r}_2,\ldots,\vec{r}_N; s_1,s_2,\ldots,s_N \,/\, \vec{r}_j;s_j)$ as

$$\langle F\rangle_j = \int_{2N-2}\cdots\int F\, P(\vec{r}_1,\vec{r}_2,\ldots,\vec{r}_{N-1};\, s_1,s_2,\ldots,s_{N-1} \,/\, \vec{r}_j;s_j) \prod_{\substack{n=1\\ n\neq j}}^{N} d\vec{r}_n\, ds_n\,, \tag{66}$$

where $\prod_{n=1}^{N} d\vec{r}_n\, ds_n = d\vec{r}_1 d\vec{r}_2 \ldots d\vec{r}_N\, ds_1 ds_2 \ldots ds_N$ and the above integration is not performed over $d\vec{r}_j$ and ds_j.

Similarly the conditional configurational averages of F with two, three or more nodules held fixed are expressed as, respectively,

$$\langle F\rangle_{jk} = \int_{2N-4}\cdots\int F\, P(\vec{r}_1,\vec{r}_2,\ldots,\vec{r}_{N-2};\, s_1,s_2,\ldots,s_{N-2} \,/\, \vec{r}_j,\vec{r}_k;\, s_j,s_k) \prod_{\substack{n=1\\ n\neq j,k}}^{N} d\vec{r}_n\, ds_n\,, \tag{67}$$

$$\langle F\rangle_{jk\ell} = \int_{2N-6}\cdots\int F\, P(\vec{r}_1,\vec{r}_2,\ldots,\vec{r}_{N-3};\, s_1,s_2,\ldots,s_{N-3} \,/\, \vec{r}_j,\vec{r}_k,\vec{r}_\ell;\, s_j,s_k,s_\ell) \prod_{\substack{n=1\\ n\neq j,k,\ell}}^{N} d\vec{r}_n\, ds_n\,,$$

etc.

Using Eqs. (65) and (66) the configurational average of F (Eq. (64)) can thus be written as

$$\langle F \rangle = \iint \langle F \rangle_j \, P(\vec{r}_j; s_j) \, d\vec{r}_j \, ds_j \, . \tag{64-a}$$

Similarly the conditional configurational averages of $\langle F \rangle_j$ and $\langle F \rangle_{jk}$ can be expressed using Eq. (65) in terms of $\langle F \rangle_{jk}$ and $\langle F \rangle_{jk\ell}$ in the following manner:

$$\langle F \rangle_j = \iint \langle F \rangle_{jk} \frac{P(\vec{r}_j, \vec{r}_k; \, s_j, s_k)}{P(\vec{r}_j; s_j)} \, d\vec{r}_k \, ds_k \tag{66-a}$$

$$\langle F \rangle_{jk} = \iint \langle F \rangle_{jk\ell} \frac{P(\vec{r}_j, \vec{r}_k, \vec{r}_\ell; \, s_j, s_k, s_\ell)}{P(\vec{r}_j, \vec{r}_k; \, s_j, s_k)} \, d\vec{r}_\ell \, ds_\ell \, . \tag{67-a}$$

In each of the above equations ((64-a), (66-a) and (67-a)) the function F on the RHS is averaged with one more nodule held fixed than on the LHS. Also in each successive equation the function F is averaged with one more nodule held fixed. Thus with each successive equation more information on the statistics of the configuration of the nodule field is required. However, rather than consider the entire series which requires knowledge of all joint probability distribution function $P(\vec{r}_j; s_j)$, $P(\vec{r}_j, \vec{r}_k; \, s_j, s_k)$, $P(\vec{r}_j, \vec{r}_k, \vec{r}_\ell; \, s_j, s_k, s_\ell)$, etc., the series may be truncated by applying an appropriate closure condition on the function F. In this study, one will see later for a sparse distribution of nodules the lowest order statistics, i.e. $P(\vec{r}_j; s_j)$ which is related to the areal number density ρ and the size distribution, is enough to describe the nodule field. However, the next higher order statistics, i.e. $P(\vec{r}_j, \vec{r}_k; \, s_j, s_k)$ is required to describe the rather crowded nodule field

which involves the pair correlation.

D. Separation of the Joint Probability Distribution Function

In this study the acoustical properties of nodules are assumed to be independent of their sizes. The scattering parameter s will be considered to depend on the nodule size characterized by its apparent radius a only (this results from the fact that in the single nodule scattering analysis average values of g, c_L/c_0 and c_T/c_0 were used for all nodules). Therefore Smith's results for the statistics of nodule deposits may be applied to multiple scattering calculations. According to Smith's photograph analysis, the nodule size is independent of its location. The joint probability function $P_j(\vec{r}_j;s_j)$ can thus be written as the product of the size probability density function $q(a_j)$, and the locational probability distribution function w as follows

$$P_j(\vec{r}_j;s_j) = q(a_j)\, w(\vec{r}_j) \ . \tag{68}$$

To illustrate the averaging procedure the multiple scattering of waves in the case of a loosely packed system, i.e. nodules are sparsely distributed on the ocean bottom, is first to be investigated. In other words, the nodule field in which the area number density ρ is low and the nodule size is much smaller than the mean separation between nodules is considered. In such a case, the location and the scattering parmeter of each nodule can thus be assumed to be independent of those of the other nodules. Under this assumption, $P(\vec{r}_1,\vec{r}_2,\ldots,\vec{r}_N;\ s_1,s_2,\ldots,s_N)$ can be written as, using Eq. (68),

$$P(\vec{r}_1,\vec{r}_2,\ldots,\vec{r}_N;\ s_1,s_2,\ldots,s_N) = \prod_{j=1}^{N} P_j(\vec{r}_j;s_j)$$

$$= \prod_{j=1}^{N} q(a_j)\ w(\vec{r}_j)\ , \tag{69}$$

where the random locational probability distribution function $w(\vec{r}_j)$, in this situation, is given by

$$w(\vec{r}_j) = \frac{\rho}{N}\ . \tag{70}$$

It can be further shown that the normalization of $P(\vec{r}_j;s_j)$ should be unity, i.e.

$$\int_0^\infty \int_A w(\vec{r}_j)\ q(a_j)\ d\vec{r}_j\ da_j = 1\ , \tag{71}$$

where A is the bottom area on which the jth nodule may lie.

However Eq. (69) cannot be applied to the case of densely packed systems, where nodules are crowded on the bottom plane, for which the pair correlation must be considered. For a dense distribution of nodules, the pair statistics may also be represented as $P(\vec{r}_j,\vec{r}_k;\ s_j,s_k)$ in Eq. (66-a) and the locational pair statistics alone may be represented by the radial distribution function f(R) as Smith did in the photograph analysis. Using Smith's results for the nodule field and assuming that the nodule size distributions are independent of their locations the pair statistics $P(\vec{r}_j,\vec{r}_k;\ s_j,s_k)$ can thus be written as

$$P(\vec{r}_j,\vec{r}_k;\ s_j,s_k) = w(\vec{r}_j,\vec{r}_k)\ q(a_j,a_k)$$

$$= \frac{\rho^2}{N^2} f(R)\ , \tag{72}$$

where $R = |\vec{r}_j - \vec{r}_k|$.

After substituting Eqs. (68), (69), (70) and (72) into Eqs. (64-a) and (66-a) one obtains

$$\langle F \rangle = \frac{\rho}{N} \iint \langle F \rangle_j \, q(a_j) \, d\vec{r}_j \, da_j \qquad (64\text{-b})$$

$$\langle F \rangle_j = \frac{\rho}{N} \iint \langle F \rangle_{jk} \, q(a_k) \, f(R) \, d\vec{r}_k \, da_k \; . \qquad (66\text{-b})$$

As can be seen from Eqs. (64-b) and (66-b), additional accuracy in evaluating the average total field <F> can, of course, be obtained by using the third equation (i.e. Eq. (67-a)), and then higher order equations which involve higher order statistics. However, at this point only two equations, i.e. (64-b) and (66-b), are considered. For nodule deposits, it turns out to be a good approximation.

IX. STATEMENT OF THE MULTIPLE SCATTERING PROBLEM AND THE FORMULATION

Consider the case of steady-state, time-harmonic scattering of waves with frequency ω. The value of the scalar wave potential ψ at the point $\vec{R}$ at time t can be represented as $\psi(\vec{R})e^{i\omega t}$. The acoustic potential ψ is related to the velocity vector $\vec{v}$ and the pressure p as follows (Eqs. (5) and (16)).

$$\vec{v} = \nabla\psi$$
$$p = i\omega \rho_0 \psi \ . \tag{73}$$

In the absence of scatterers from the acoustic medium, $\psi(\vec{R})$ satisfies the Helmholtz equation (ref. Chapter II)

$$(\nabla^2 + k^2)\ \psi = 0 \ .$$

In this study, the self consistent field approach (see Foldy [30]) will be used for the multiple scattering analysis. The self consistent field method assumes that a wave is emitted by each scatterer of an amount and directionality. The excitation is determined by adding to the incident wave all scattered waves emitted by the other scatterers which are in turn affected by the emitted wave from that scatterer. The self consistent procedure is not an expansion in primary, secondary, tertiary waves, etc. The field acting on a given scatterer or emitted by it includes the effects of all orders of scattering. However, in this chapter, the orders of scattering will be introduced and interpreted so that one can physically understand the scattering processes.

A. Self Consistent Method

Now consider a random distribution of N nodules. The total wave function at the field point $\vec{R}$ is the sum of the incident wave $\psi_i(\vec{R})$ and the scattered field $U(\vec{R})$ and can be written as

$$\psi(\vec{R}) = \psi_i(\vec{R}) + U(\vec{R}) \ , \tag{74}$$

where the scattered field is the sum of the waves emitted by each of the N nodules,

$$U(\vec{R}) = \sum_{j=1}^{N} u_j(\vec{R}) \ . \tag{74-a}$$

The jth nodule, with its center at $\vec{r}_j$ on the bottom plane (see Figure 28), emits a wave whose directional strength, i.e. the scattering amplitude, is determined by the scattering function $f(a_j,\theta_j)$ (see Eq. (42-a)) and the external field $\psi^j(\vec{r}_j)$ causing the scattering. The propagation of the emitted wave is described by the medium propagation characteristics from the center position of the jth nodule $\vec{r}_j$ to the field location $\vec{R}$ denoted as $E(\vec{R},\vec{r}_j)$. Symbolically the jth scattered wave $u_j(\vec{R})$ can be represented as

$$u_j(\vec{R}) = f(a_j,\theta_j)\ \psi^j(\vec{r}_j)\ E(\vec{R},\vec{r}_j) \ , \tag{75}$$

where $E(\vec{R},\vec{r}_j) = \dfrac{e^{-ik|\vec{R}-\vec{r}_j|}}{|\vec{R}-\vec{r}_j|}$ in the far field.

The self consistent approach results from defining the external field which excites scattering from the jth nodule as the total field (see Figure 29-a) minus the wave emitted by the jth nodule itself

$$\psi^j(\vec{r}_j) = \psi(\vec{r}_j) - u_j(\vec{r}_j) \ . \tag{76}$$

The above equation can be written as, using Eq. (74) and (74-a) and letting $\vec{R} = \vec{r}_j$,

$$\psi^j(\vec{r}_j) = \psi_i(\vec{r}_j) + \sum_{\substack{k=1 \\ k\neq j}}^{N} u_k(\vec{r}_j) \ . \tag{76-a}$$

Thus the singularity of the emitted wave at $\vec{r}_j$ is eliminated while all orders of scattering are considered. Figure 29-b gives the picture of the external field acting on the jth nodule. Eqs. (74) and (76-a) constitute the following fundamental pair of equations of multiple scattering, after substituting the expressions for $U(\vec{R})$ and $u_j(\vec{R})$ (Eqs. (74-a) and (75),

$$\psi(\vec{R}) = \psi_i(\vec{R}) + \sum_{j=1}^{N} f(a_j,\theta_j)\ \psi^j(\vec{r}_j)\ E(\vec{R},\vec{r}_j) \tag{74-b}$$

$$\psi^j(\vec{r}_j) = \psi_j(\vec{r}_j) + \sum_{\substack{k=1 \\ k\neq j}}^{N} f(a_k,\theta_k)\ \psi^k(\vec{r}_k)\ E(\vec{r}_k,\vec{r}_j) \tag{76-b}$$

B. Orders of Scattering

In principle, the total wave function at $\vec{R}$, i.e. $\psi(\vec{R})$, can be obtained by eliminating $\psi^j(\vec{r}_j)$ from Eqs. (74-b) and (76-b) and solving for the incident wave $\psi_i(\vec{R})$. By substituting Eq. (76-b) into (74-b) and iterating the same process in the following manner Eq. (74-b) then becomes:

$$\psi(\vec{R}) = \psi_i(\vec{R}) + \sum_{j=1}^{N} f(a_j,\theta_j)\, E(\vec{R},\vec{r}_j)\, [\psi_i(\vec{r}_j)$$

$$+ \sum_{k(\neq j)}^{N} f(a_k,\theta_k)\, \psi^k(\vec{r}_k)\, E(\vec{r}_k,\vec{r}_j)]$$

$$= \psi_i(\vec{R}) + \sum_{j=1}^{N} A_j\, \psi_{ij} + \sum_{j=1}^{N} \sum_{k\neq j}^{N} A_j\, A_k\, \psi_{ik}$$

$$+ \sum_{j=1}^{N} \sum_{k\neq j}^{N} \sum_{\neq k}^{N} A_j\, A_{kj}\, A_{\ell k}\, \psi_{i\ell} + \ldots , \qquad (77)$$

where $A_j = f(a_j,\theta_j)\, E(\vec{R},\vec{r}_j)$

$A_{kj} = f(a_k,\theta_k)\, E(\vec{r}_k,\vec{r}_j)$

$A_{\ell k} = f(a_k,a_\ell)\, E(\vec{r}_\ell,\vec{r}_k)$

$\psi_{ij} = \psi_i(\vec{r}_j)$

$\psi_{ik} = \psi_i(\vec{r}_k)$

$\psi_{i\ell} = \psi_i(\vec{r}_\ell)$.

It is necessary now to consider each term of Eq. (77) to understand its physical meaning (see Twersky [38]). The first term on the RHS of Eq. (77) is the incident wave at $\vec{R}$. The second term, actually a summation of $A_j\, \psi_{ij}$ represents all the single scattering (see Figure 30-a). The next summation, $\sum_{j=1}^{N} \sum_{k(\neq j)}^{N} A_j\, A_{kj}\, \psi_{ik}$, represents all the double scattering (see Figure 30-b). The fourth term is a triple summation, but the terms k=j and ℓ=k are excluded, while the term ℓ=j is not excluded. Therefore, this summation may be separated into two summations in which one includes the terms containing distinct j, k and ℓ, the other has the terms corresponding to ℓ=j, i.e.

$$\sum_{j=1}^{N} \sum_{k(\neq j)}^{N} \sum_{\ell(\neq k)}^{N} A_j A_{kj} A_{\ell k} \psi_{i\ell} = \sum_{j=1}^{N} \sum_{k(\neq j)}^{N} \sum_{\ell(\neq k,\neq j)}^{N} A_j A_{kj} A_{\ell k} \psi_{i\ell}$$

$$+ \sum_{j=1}^{N} \sum_{k(\neq j)}^{N} A_j A_{kj} A_{jk} \psi_{ij} \,. \qquad (77\text{-a})$$

The triple summation on the RHS of Eq. (77) is pictured in Figure 30-c. The next second summation involves only two nodules located at $\vec{r}_j$ and $\vec{r}_k$ (see Figure 30-d).

Generally speaking, the total scattered field at $\vec{R}$, i.e. $\sum_{j=1}^{N} A_j \psi^j(\vec{r}_j)$, is affected by two major multiple scattering processes and can be divided into the following two groups:

1. The first group consists of all the multiply scattered waves which involve chains of successive scattering through different nodules and may be called the island-jump scattering (see Figure 31-a). This kind of scattering dominates almost all the multiple scattering processes and when the number of nodules is large Eq. (77) can be approximated by

$$\chi(\vec{R}) = \chi_i(\vec{R}) + \sum_{j=1}^{N} A_j \psi_{ij} + \sum_{j=1}^{N} \sum_{k\neq j}^{N} A_j A_{kj} \psi_{ik}$$

$$+ \sum_{j=1}^{N} \sum_{k(\neq j)}^{N} \sum_{\ell(\neq k,\neq j)}^{N} A_j A_{kj} A_{\ell k} \psi_{i\ell} \qquad (77\text{-b})$$

with only a small difference (see Ishimaru [37]). It can further be shown that there are N terms for single scattering, N-1 terms for double scattering, N-2 terms for triple scattering and so on.

2. The second group is composed of all orders of multiple scattering (except single scattering) which all the scattering paths go through a

nodule at least twice (ping-pong type scattering, see Figure 31-b). This kind of scattering may become important when the backscattering is large compared with the scattering in all other directions and the number of nodules is finite [37]. However, in the present problem the main focus is aimed at the first group.

Eq. (77) is also known as the expanded representation, by Twersky [38], which is useful in understanding the scattering processes involved.

C. Coherent and Incoherent Field

Since the nodules are randomly distributed, the scattered field U is not constant and its magnitude (also phase) will fluctuate in a random manner. Thus one sees from Eq. (74) that the total field at $\vec{R}$, i.e. $\psi(\vec{R})$, is also a random function and can usually be divided into the average field $\langle\psi\rangle$ and the fluctuating field ψ'. The reason for this is because the multiple scattering problem is usually divided into a consideration of the coherent and incoherent radiation. (The average field $\langle\psi\rangle$ is also called the coherent field and ψ' the incoherent field.)

The square of the magnitude of the coherent field $|\langle\psi\rangle|^2$ is the coherent component and the average of the square of the magnitude of the incoherent field is the incoherent component. The sum of the coherent and incoherent components is the average of the square of the magnitude of the wave function, i.e.

$$\langle|\psi|^2\rangle = |\langle\psi\rangle|^2 + \langle|\psi'|^2\rangle \ , \tag{78}$$

where ψ' is related to U as

$$\psi' = U - \langle U \rangle$$

or (78-a)

$$\langle |\psi'|^2 \rangle = \langle |U|^2 \rangle - |\langle U \rangle|^2$$

The energy flux $\vec{s}$ defined as [11]

$$\vec{s} = \frac{1}{2} (p^* \vec{v} + p \vec{v}^*)$$

is an important quantity in the wave propagation theory for considering energy conservation. Using Eq. (73) the energy flux $\vec{s}$ can be expressed in terms of ψ as:

$$\vec{s} = \frac{i\omega \rho_0}{2} (\psi^* \nabla\psi - \psi \nabla\psi^*) ,$$

where the asterisk denotes the complex conjugate of the quantity to which it is attached. The configurational average of the energy flux becomes

$$\langle \vec{s} \rangle = \frac{i\omega \rho_0}{2} [\langle \psi^* \nabla\psi \rangle - \langle \psi \nabla\psi^* \rangle]$$

or (79)

$$\langle \vec{s} \rangle = \omega k \rho_0 \, \mathrm{Re} \left\langle \frac{\psi^* \nabla\psi}{-ik} \right\rangle \quad \text{(see [43])}$$

The average energy flux $\langle \vec{s} \rangle$ contains also coherent and incoherent components and will be discussed in more detail later.

D. Configurational Average of the Wave Function

As mentioned in Chapter VIII, one is interested in quantities which are averaged over all possible configurations of nodules. According to Foldy's discussion [30] it is more practical to take the configurational averages of fundamental quantities, e.g. ψ, and solve for the averaged quantities than to solve the fundamental quantities for the total field

and then perform the averaging process. In other words, instead of solving $\psi(\vec{R})$ from Eqs. (74-b) and (76-b) and find the configurational average of $\psi(\vec{R})$, i.e. $\langle\psi(\vec{R})\rangle$, one will take the configurational average of $\psi(\vec{R})$ first and solve for $\langle\psi(\vec{R})\rangle$ using the self consistent approach [30]. By the same procedure results can also be obtained for the configurational average of the energy flux $\langle\vec{s}\rangle$.

The configurational average of $\psi(\vec{R})$ can be obtained by substituting the expression of $\psi(\vec{R})$ (Eq. (74-b)) for F in Eq. (64-b),

$$\langle\psi(\vec{R})\rangle = \langle\psi_i(\vec{R})\rangle + \frac{\rho}{N}\sum_{j=1}^{N}\int E(\vec{R},\vec{r}_j)\,\langle\overline{f(a_j,\theta_j)}\;\psi^j(\vec{r}_j)\rangle_j\,d\vec{r}_j\ , \tag{80}$$

where $\overline{f(a_j,\theta_j)} = \int_0^\infty f(a_j,\theta_j)\,q(a_j)\,da_j$ is the size averaged individual scatterer's strength. The above equation can be further reduced to

$$\langle\psi(\vec{R})\rangle = \psi_i(\vec{R}) + \rho\int E(\vec{R},\vec{r}_j)\,\langle\overline{f(a_j,\theta_j)}\;\psi^j(\vec{r}_j)\rangle_j\,d\vec{r}_j\ , \tag{80-a}$$

since the configurational average of $\psi_i(\vec{R})$ remains the same and the position of the jth nodule is arbitrary.

In a similar way, the configurational average of the external field of the jth nodule with its position held fixed can be written as, using Eq. (66-b) and the approximation $\frac{N-1}{N} \sim 1$ for large N,

$$\langle\psi^j(\vec{r}_j)\rangle_j = \psi_i(\vec{r}_j) + \rho\int E(\vec{r}_k,\vec{r}_j)\,f(R)\,\langle\overline{f(a_k,\theta_k)}\;\psi^k(\vec{r}_k)\rangle_{jk}\,d\vec{r}_k \tag{81}$$

As a matter of fact, if one keeps doing the averaging process a series of N coupled integral equations known as the Foldy-Lax hierarchy

[37] will result. Generally speaking, to evaluate the configurational average of the quantity on the LHS in the Foldy-Lax hierarchy the information on the RHS of the same equation is required which appears to be evaluated as the LHS of the next equation. However by applying an appropriate closure condition for one equation in the Foldy-Lax hierarchy the average quantity on the LHS can be evaluated from the RHS directly in the same equation. Thus equations before this can be solved successively backwards using the obtained information and equations after this hierarchy are truncated. This is essentially a procedure which ignores the effects of the higher order statistics.

For a sparse distribution, the appropriate closure condition due to Foldy [30] is that the conditional average of the external field of the jth scatterer is nearly equal to the average total field at $\vec{r}_j$, i.e.

$$\langle \psi^j(\vec{r}_j) \rangle_j \sim \langle \psi(\vec{r}_j) \rangle \ . \tag{82}$$

The resulting relation for the self consistent average field is, after substituting Eq. (82) into Eq. (80-a),

$$\langle \psi(\vec{R}) \rangle = \psi_i(\vec{R}) + \rho \int E(\vec{R},\vec{r}_j) \, \overline{\langle f(a_j,\theta_j) \rangle} \, \langle \psi(\vec{r}_j) \rangle \, d\vec{r}_j \ . \tag{80-b}$$

The closure condition of Eq. (82) assumes that the configuration of other nodules and the average total field are affected little by the location and the scattering parameter of the jth nodule. Therefore for a sparse distribution Eq. (80-b) alone can appropriately describe the average total field $\langle \psi(\vec{R}) \rangle$ (or coherent field $\langle \psi(\vec{R}) \rangle$) and all other equations in the Foldy-Lax hierarchy are truncated. One also sees that only the lowest order statistical quantity ρ is required for a sparse distribution of nodules.

However, for crowded scatterers (dense distributions) the locational statistics (see discussions in the previous chapter) become important. Consideration of correlated pair statistics involves inclusion of the second equation (Eq. (81)) in the Foldy-Lax hierarchy. In the crystalline case, Eqs. (80-a) and (81) constitute a complete description of the average total field since no additional information can be obtained by holding additional scatterers fixed. Thus for any fixed set of scatterers, $\langle\psi^k\rangle_{jk}$ does not differ from $\langle\psi^j\rangle_j$ and therefore no approximations are required to treat the crystalline case. In order to apply this criterion to the present problem an appropriate closure condition is required. The corresponding closure condition

$$\langle\psi^k(r_k)\rangle_{jk} \sim \langle\psi^k(r_k)\rangle_k \tag{83}$$

was termed the quasi crystalline approximation by Lax [39] since it is strictly valid in the crystalline case. This approximation is tacitly made in many treatments of homogeneous media.

Physically the presence of the kth scatterer affects its external field, i.e. by restricting the locations of the others through pair correlations, but the exact location of a particular one of the others, the jth, is unimportant. This is a particularly good approximation for a dense distribution of scatterers where the jth scatterer would tend to be lost in the crowd of others. The resulting coupled pair of equations are

$$\langle\psi(\vec{R})\rangle = \psi_i(\vec{R}) + \rho \int E(\vec{R},\vec{r}_j)\, \langle\overline{f(a_j,\theta_j)}\, \psi^j(\vec{r}_j)_j\rangle\, d\vec{r}_j \tag{80}$$

$$\langle\psi^j(\vec{r}_j)\rangle_j = \psi_i(\vec{r}_j) + \rho \int E(\vec{r}_k,\vec{r}_j)\, f(R)\, \langle\overline{f(a_k,\theta_k)}\, \psi^k(\vec{r}_k)\rangle_k\, d\vec{r}_k \tag{81-a}$$

One sees from Eq. (80-a) that a next higher order statistics, i.e. the radial distribution function f(R), besides the area number density ρ is required to obtain the average total field for a dense distribution of nodules.

E. Size Averaging of the Scattering Function

In evaluating the coherent field $\langle\psi\rangle$ using the self consistent method, the size averaging of the scattering function $\overline{f(a_j,\theta_j)}$ can be either done earlier or later. According to the previous assumption the nodule sizes are independent of their locations so that the integrations can be done separately.

The size averaging of the scattering function is, from Eq. (80),

$$f(a_j,\theta_j) = \int_0^\infty f(a_j,\theta)\, q(a_j)\, da_j \ . \tag{80-c}$$

For a uniform size distribution, i.e. $a_j = \bar{a}$, one knows

$$\overline{f(a_j,\theta_j)} = f(\bar{a},\theta_j) = f(a,\theta_j) \ .$$

However, for the size distribution of the Rayleigh type $q(a_j)$ can be obtained as, from Eq. (61) with m = 1,

$$q(a_j) = (2a_j^3/b^2)\ \mathrm{Exp}\ (-a_j^4/2b^2) \ , \tag{61-a}$$

where $b^2 = 0.74(\bar{a})^4$ calculated from Table 4.

Substituting Eq. (61-a) into Eq. (80-c) and rearranging the terms $\overline{f(a_j,\theta_j)}$ can be written as

$$\overline{f(a_j,\theta_j)} = 2.704 \int_0^\infty f(x\bar{a},\theta)\, x^3\, e^{-0.676\, x^4}\, dx \,, \qquad (80\text{-d})$$

where $x = \frac{a_j}{\bar{a}}$, or

$$\overline{f(a_j,\theta_j)} = \int_0^\infty f(1.103\, \eta^{1/4}\, \bar{a},\theta_j)\, e^{-\eta}\, d\eta \,,$$

where $\eta = 0.676\, x^4$.

It is easy to verify

$$\int_0^\infty q(a_j)\, da_j = 1$$

by substitution of variables yielding,

$$\int_0^\infty e^{-\eta}\, d\eta = 1 \,.$$

In fact $\overline{f(a_j,\theta_j)}$ is difficult to evaluate because it is both frequency and θ dependent. But the size averaging of the backscattering (or forward scattering) function $\overline{f(a_j,\theta)}$ is θ independent and its magnitude can be calculated using a computer.

Generally speaking, the size averaging process is able to smooth the resonant spikes in the high frequency region. This can be seen from Figure 32 which is the comparison between the square root of the total scattering cross section divided by the nondimensional frequency, i.e., $\sqrt{\sigma}/ka$, vs. ka for a uniform size distribution of nodules (has been normalized by $2\pi\rho a^2$) and that for nodules with the Rayleigh size distribution in which

$$\overline{\sqrt{\sigma}}/ka = \left(\int_0^\infty \sqrt{\sigma}\, q(a)\, da\right) / ka \,.$$

The calculation is based on a sparse distribution of nodules and the

expression for the total scattering cross section σ can be found from Eq. (44-c).

X. NARROW BEAM ANALYSIS

Most investigators use plane wave excitation to analyze the multiple scattering problem from a plane of scatterers (see References [34], [40], [41], [42], [43]). The results yield a scattered wave which is analogous to the reflection of a plane wave on a rough surface characterized by an equivalent reflection coefficient [43]. In marine geophysics it is customary to use the ray theory [13] together with the plane wave reflection coefficient to study the reflections at the sea floor, i.e. rough subbottom. Therefore, the present study uses the normally incident plane wave as this closely represents the equipment (see Figure 1) used in the remote sensing. The narrow beam spherical wave (as an acoustic source) analysis is done here to indicate the accuracy of its usage and justify the plane wave analysis for the multiple scattering problem. The normal incidence of a narrow beam is also used so that one can obtain a physical interpretation of the analysis without going into too much complexity in mathematics.

In this chapter, the backscattered response of a random distribution of manganese nodules on a plane subjected to a normally incident, narrow beam form acoustic wave is to be investigated for single scattering (valid for a sparse distribution [44]). Typical echo sounders use beam widths of at least 60° for the acoustic beam so as to accommodate the roll and pitch of the survey ship. However, in the deep sea sounding environment high intensity is required to overcome transmission losses occurring in the water column. In order to do this the

narrow beam width is beneficial because it concentrates the acoustic energy into a smaller area on the bottom. Therefore in the market much smaller beams are becoming common, with 6° being representative [45].

A. Gaussian Beamform Acoustic Wave

The acoustic source which is located a distance H above the bottom plane (see Figure 33), radiates a spherically spreading pressure wave with a Gaussian beamform

$$\psi_i(\vec{R}) = \psi_a \frac{R_o\, e^{-(ik+\mu)|\vec{R}-\vec{z}|}}{|\vec{R}-\vec{z}|} e^{-\alpha\delta^2} \quad . \tag{84}$$

In which ψ is the acoustical potential, $\vec{z} = (0,0,H)$, μ the absorption coefficient in the fluid medium (ocean), R_o the reference distance (usually one meter), δ the beam width (in radian), $1/|\vec{R}-\vec{z}|$ the spreading factor and α the Gaussian beamform coefficient defined as

$$\alpha = \frac{\ln 4}{(\delta_{HP})^2} \quad ,$$

where δ_{HP}, the half power beam width, is shown in Figure 34.

On the bottom plane, i.e. z = 0, at a distance $\vec{r}_j$ from the beam axis the incident wave field becomes

$$\psi_i(\vec{r}_j) = \psi_a \frac{R_o}{D} e^{-(ik+\mu)D}\, e^{-\alpha\delta_j^2} \quad , \tag{84-a}$$

where D is the distance between the transducer and $\vec{r}_j$. The incident field at the image point, i.e. z = -H or D = 2H, is

$$\psi_i(z=-H) = \psi_a\, R_o \frac{e^{-(ik+\mu)2H}}{2H} \quad . \tag{84-b}$$

B. Scattered Wave Field

A single nodule located at $\vec{r}_j$ on the bottom plane (z=0) will radiate a spherically spreading wave due to the excitation by the incident wave. The strength of the radiated wave depends on both the external wave field (for the single scattering case the incident wave field $\psi_i(\vec{r}_j)$ only) and the nodules' characteristics which can be described by the scattering function $f(a,\theta)$ (see Eq. (42-a)). Although the scattering function $f(a,\theta)$ was derived for a plane wave, it is appropriate for the narrow beam analysis since the field curvature is negligible at the nodule. The backscattered field (θ_j=0) at z=H of the single nodule at $\vec{r}_j$ can thus be defined as, using Eqs. (75) and (84-a),

$$u_{j(b.s)} = f(a_j,0)\,\frac{e^{-(ik+\mu)D}}{D}\,\psi_i(\vec{r}_j)$$

$$= f(a_j,0)\,\psi_a\,\frac{R_o}{D^2}\,e^{-(ik+\mu)2D}\,e^{-\alpha\delta^2} \qquad (86)$$

In which $e^{-(ik+\mu)D}/D$ is the far field expression for $E(\vec{R},\vec{r}_j)$ in Eq. (75) which satisfies the radiation condition [46]. The subscript b.s. denotes the backscattering. One sees from Eq. (86) that the spreading factor is now $1/D^2$ for the scattered field $u_{j(b.s.)}$.

If there is a sparse distribution of nodules on the ocean floor, the total backscattered field is simply the sum of the fields scattered from each nodule. In other words, the single scattering phenomenon which the external field of each nodule is due to the incident wave alone (see Figure 30-a) and is the first order approximation of the scattering processes. The total backscattered field is thus found as, using Eqs. (74-a), (80-a) and (86),

$$\langle U_{b.s.} \rangle = \rho \, \overline{f(a_j,0)} \, R_o \, \psi_a \int_0^\infty \frac{e^{-(ik+\mu)2D} \, e^{-\alpha\delta_j^2} \, 2\pi \, r_j \, dr_j}{D^2} \, , \tag{87}$$

where the axial symmetry and the polar integration for a large area

$$\int_A d\vec{r}_j = \int_0^{2\pi} \int_0^\infty r_j \, dr_j \, d\theta = 2\pi \int_0^\infty r_j \, dr_j$$

have been employed. From the geometry (Figure 33) one sees

$$\tan \delta_j = \frac{r_j}{H}$$

$$D^2 = H^2 + r_j^2 \, .$$

Using the above relatoinships and changing the integration variable by (instead of r_j integration, δ_j integration is used)

$$r_j \, dr_j = H^2 \left(\frac{r_j}{H}\right) d\left(\frac{r_j}{H}\right)$$

$$= H^2 \tan \delta_j \sec^2 \delta_j \, d\delta_j$$

in Eq. (87), the configurational average of the total backscattered field becomes

$$\langle U_{b.s.} \rangle = 2\pi\rho \, \overline{f(a_j,0)} \, \psi_a \, R_o \int_0^{\frac{\pi}{2}} e^{-2(ik+\mu)H \sec \delta_j} \, e^{-\alpha\delta_j^2} \tan \delta_j \, d\delta_j \tag{87-a}$$

The integral in the above equation can be done using the principle of stationary phase [48]. The magnitude of kH is always much larger than that of $\alpha\delta^2$ (see Table 5 for comparison). For $kH \gg 1$, which is a phase control factor, the integral can be converted to the following form

$$\int_0^{\frac{\pi}{2}} e^{-ikHg(\delta_j)} \tan \delta_j \, d\delta_j \, , \qquad (87\text{-b})$$

in which $g(\delta_j) = (2 + \frac{2\mu}{ik}) \sec \delta_j + \frac{\alpha}{ikH} \delta_j^2$.

The phase angle γ is obtained by solving the δ_j which makes

$$g'(\delta_j) = (2 + \frac{2\mu}{ki}) \sec \delta_j \tan \delta_j + \frac{2\alpha}{ikH} \delta_j = 0$$

and is found to be zero, i.e. $\gamma = 0$, in this case (in the interval of 0 and $\pi/2$). The second derivative of $g(\delta_j)$ evaluated at the phase angle $\gamma = 0$ is

$$g''(0) = 2 + \frac{2\mu}{ki} + \frac{2\alpha}{ikH}$$

Using the stationary phase principle, (87-b) can be written in the following manner

$$g(\gamma) \int_0^{\infty} e^{-ikH \, g''(\gamma) \frac{\xi^2}{2}} \xi \, d\xi \, , \qquad (87\text{-c})$$

in which ξ is the parameter in the Taylor expansion around the phase angle γ, i.e.

$$g(\delta_j) = g(\gamma + \xi) = g(\gamma) + g'(\gamma)\xi + \frac{g''(\gamma)}{2!} \xi^2 + \ldots$$

$$\text{tau } \delta_j = \tan (\gamma + \xi) = \tan\gamma + \sec^2\gamma \, \xi + \ldots \, .$$

Substituting $\gamma = 0$ and the expressions for $g(\gamma)$ and $g''(\gamma)$ into (87-c) one obtains

$$e^{-ik(1+\frac{\mu}{ik})\,2H}\int_0^{\infty} e^{-ikH(1+\frac{\mu}{ik}+\frac{\alpha}{ikH})\,\xi^2}\,\xi\,d\xi \quad . \tag{88}$$

Finally after substituting Eq. (88) into (87-a) and carrying out the integral in (88) the configurational average of the total backscattered field becomes

$$\langle U_{b.s.}\rangle = \frac{2\pi\rho\,\overline{f(a_j,0)}}{ik}\cdot\left(\frac{1}{1+\frac{\alpha}{ikH}+\frac{\mu}{ik}}\right)\cdot\frac{R_o\,e^{-(ik+\mu)2H}}{2H}\,\psi_a \quad . \tag{89}$$

One sees from the above equation that the last term is actually the incident field at the image point, i.e. z = -H, comparing with Eq. (84-b). The beam effect which involves in the second term α/ikH can be evaluated. As can be seen from Table 6 at large depth, unless a very narrow beam width under the low frequency is used, the beam effect on the average backscattered field is very small and can be neglected for further analysis of multiple scattering problems. The first term is thus recognized as an equivalent plane wave reflection coefficient which relates the average backscattered field to the incident wave field by just a simple proportionality. This is physically the phenomenon of the plane wave excitation and thus the validity of the plane wave analysis for the nodule scattering problems has been verified through this narrow beam investigation. This fact indicates that higher order scattering models may use more elaborate plane wave analysis to investigate the higher order scattering effects.

XI. SUMITOMO'S SCATTERING ANALYSIS

A major effort in sounding for manganese nodules has been conducted by the engineers working in the Ocean Resources Department of Sumitomo Metal Mining Company (Tokyo, Japan). Their work proceeded from 1976 without any publicity until they put a manganese nodule sounding data analysis system (the MFES - Multi-Frequency Exploration System) on the market in April 1981. In informal meetings between Dr. Magnuson and Sumitomo representatives at the 13th Offshore Technology Conference in Houston in May 1981 and subsequent correspondence it was determined that the MFES system is based on the same principle developed by Magnuson et al [47], i.e. variation of the bottom reflectivity with frequency due to the nodule presence. The MFES system development included in situ experimentation and is complementary to this study (which is based on a more sophisticated theoretical analysis, computer predictions and laboratory work). This more elaborate theoretical approach is better suited to refinements and improvements of the first generation MFES system. However, a brief review of the Sumitomo's work, collected nodule data and a short discussion of the limitations of the MFES system will be given.

A. Sumitomo's Model for Bottom Reflexibility

According to the principle that the bottom reflectivity (equivalent reflection coefficient) varies with the frequency of the incident acoustic wave when nodules are present, the nodule deposits can be

characterized by the specific acoustic signature of the bottom in the presence of nodules (Figure 14 presents the acoustic signature of a single Pacific nodule). Figure 35 shows the general idea of using the acoustic response spectrum (usually represented by the bottom reflectivity vs. the nondimensional frequency $k\bar{a}$) to infer the mean diameter and the area weight density of the nodule deposit. Sumitomo's model considered a spherically radiating acoustic wave incident on a randomly distributed planar field of rigid uniform sized spherical nodules.

In Sumitomo's model nodules are widely distributed on the sea bottom and the backscattered wave from each nodule will bear a different phase. Instead of the real backscattered sound path $|\vec{R}-\vec{r}_j|$ for each nodule the depth H was used for approximation. The total backscattered pressure at z = H was found to be (with the propagation term $e^{-i(kH-\omega t)}$ removed)

$$\sum_{j=1}^{N} p_{b.s.} = \sum_{j=1}^{N} \left(\frac{e^{-\mu H}}{H}\right) \sqrt{(TS)_j} \left(\frac{R_o\, e^{-\mu H}}{H}\, p_a\right) \sin(-2k\,\zeta_j) \,, \quad (91)$$

where μ = the absorption coefficient for the acoustic medium (ocean)

TS = Target Strength of a single nodule (rigid)

ζ_j = difference in the sound wave path (phase effect, see Figure 36) .

The term $e^{-\mu H}/H$ refers to the return loss and $R_o\, e^{-\mu}\, p_a/H$ is the sound pressure at the bottom plane.

One sees from Eq. (91) that Sumitomo's model has apparently used the sparse distribution assumption and therefore applied a single

scattering theory in obtaining the result. It is similar to the narrow beam analysis in the previous chapter. However, the model does not consider the beam form and approximates the distance to each nodule as being equal to the sounding depth. Sumitomo's model also assumed the nodules' sizes are uniform, i.e. $a_j = \bar{a}$, so that Eq. (91) can be converted to the following form, using the polar integration,

$$\Sigma\, p_{b.s.} = \rho\sqrt{TS}\,\frac{e^{-2\mu H}}{H^2}\,p_a \int_0^{\infty} \sin(-2k\zeta)\, 2\pi r\, dr \qquad (91\text{-a})$$

From the geometry (Figure 36) one sees

$$\zeta = D - H \qquad \text{and} \qquad D^2 = H^2 + r^2$$

By changing the integration variable, using the above relationship, Eq. (91-a) becomes

$$\Sigma\, p_{b.s.} = \rho\sqrt{TS}\, R_o\, \frac{2\pi e^{-2\mu H}}{H^2}\,p_a \int_H^{\infty} \sin[2k(H-D)]D\, dD\ . \qquad (91\text{-b})$$

The above equation can be easily solved by either integrating by parts or using the following formula

$$\int x \sin x\, dx = \frac{\sin \alpha x}{\alpha^2} - \frac{x \cos \alpha x}{\alpha}\ .$$

Finally the amplitude of the total backscattered pressure can be found as

$$|\Sigma\, p_{b.s.}| = \frac{2\pi\rho\sqrt{TS}}{k}\,\frac{R_o\, e^{-2\mu H}}{2H}\,p_a\ . \qquad (92)$$

The term $\frac{2\pi\rho\sqrt{TS}}{k}$ in Eq. (92) is defined as the bottom reflexibility. Comparing with Eq. (90) one sees that it is similar to the equivalent reflection coefficient $\frac{2\pi\rho\ \overline{f(a,0)}}{ik}$ obtained from the narrow beam analysis. Actually it can be shown that for the uniform size distribution $\sqrt{TS}$ is the backscattering function f(a,0).

B. Results of Sumitomo's Model

Sumitomo employed an area coverage 0.785 (the ratio between the area covered by nodules and the bottom area of interest) to calculate the bottom reflexibility with respect to $k\bar{a}$. The result is represented as a plot of reflexibility vs. $k\bar{a}$ in Figure 37. As expected the result matches well with that calculated from the equivalent reflection coefficient using the rigid sphere as a scatterer. The reason is that the target strength TS in Sumitomo's model from definition [13] is

$$TS = \frac{|p_{b.s.}|^2}{|p_i|^2} R^2$$

Using Eq. (42) and (42-a) for $\theta = 0$ (backscattering) it can be written as

$$TS = |f(\bar{a},0)|^2 , \tag{93}$$

where f(a,0) is referred to Eq. (32-a) for $\theta = 0$.
Therefore the bottom reflexibility can be related to the equivalent reflection coefficient as follows

$$\text{Reflexibility} = \frac{2\pi\rho\sqrt{TS}}{k} = \left|\frac{2\pi\rho\ f(\bar{a},0)}{ik}\right| = C_R \tag{94}$$

The area number density ρ corresponded to the square packing whose area coverage 0.785 (used in Sumitomo's calculation) is found to be $1/4\ \bar{a}^2$ (see Figure 38). Thus in this case the equivalent reflection coefficient C_R is reduced to

$$C_R = 1.57 \left| \frac{\Sigma\ (2n+1)(-1)^n\ i\ /\ (1+i\ C_n)}{(k\bar{a})^2} \right| . \qquad (94\text{-a})$$

The above equation may be evaluated for different frequencies ($k\bar{a}$) by using a computer. One sees from Figure 37 that the area coverage and the mean size $\bar{a}$ of the nodule deposit can be inferred by the first peak of the bottom acoustic signature shown in Figure 35. In general, the peak occurs at $k\bar{a} \sim 1$. The horizontal shift of the peak relates to the change of the average size $\bar{a}$ and the area number density ρ can be inferred from the vertical shift of the peak.

As mentioned previously, for a dense distribution of scatterers the single scattering analysis is inadequate to describe the scattered field. Even so, the sparse distribution assumptions (made implicitly in Sumitomo's model) are seen to give surprisingly good results as evidenced by the good correlation of the Sumitomo MFES data in Figure 39. However, one major disadvantage of Sumitomo's MFES system is that calibration constants must be set using grab sample data prior to sounding in a given area. This is apparently done for at least four reasons: (1) Sumitomo's model used rigid spheres which needs to be corrected for the finite impedance of nodules, (2) to account for sedimentary bottom reflectivity, (3) to account for the difference between the sparse distribution and dense distribution of nodules using the same scattering

analysis and (4) to account for water column transmission losses.

XII. MULTIPLE SCATTERING ANALYSIS OF THE NODULE FIELD EXCITED BY A NORMALLY INCIDENT PLANE WAVE

In this chapter, the configurational averages of the wave function ψ, the square of field ψ^2 and the wave energy flux $\vec{s}$ will be derived for manganese nodule deposits excited by a normally incident plane wave. First consider a sparse distribution of nodules so that only the first equation (Eq. (80-b)) in the Foldy-Lax hierarchy is required to estimate the average field. Both the reflection and transmission coefficient for the nodule field will be investigated. Relations between the coherent and incoherent energy flux will be obtained using the energy principle, i.e. conservation of energy [43]. The effect of the pair statistics on the average scattered field will be examined using a simplified form of the radial distribution function f(R) and the coupled pair of Eqs. (80) and (81-a) which employs the quasi crystalline approximation as a closure condition.

A. The Configurational Average of the Wave Function, $\langle\psi\rangle$

Considering a plane wave normally incident upon a sparsely distributed nodule field (see Figure 40) then the coherent field becomes, using Eq. (74),

$$\begin{aligned} \langle\psi\rangle &= \langle\psi_i\rangle + \langle U\rangle \\ &= \psi_a e^{ikz} + \langle U\rangle \ . \end{aligned} \tag{95}$$

Comparing Eq. (95) with (74-b) one sees

$$\langle U \rangle = \rho \int E(\vec{R},\vec{r}_j) \langle \overline{f(a_j,\theta_j)}\ \psi(\vec{r}_j) \rangle\, d\vec{r}_j \qquad (95\text{-a})$$

Physically speaking, the average scattered field can be expressed as a combination of a reflected wave and a transmitted wave due to the plane wave excitation [43]. Therefore for the present case (normal incidence) the configurational average of the scattered field, i.e. $\langle U \rangle$, may be expressed as

$$\begin{aligned} \langle U \rangle|_{z>0} &= \langle U \rangle^{+} = C^{+}\ \psi_a\ e^{-ikz} \\ \langle U \rangle|_{z<0} &= \langle U \rangle^{-} = C^{-}\ \psi_a\ e^{ikz} \\ \text{or } \langle U \rangle^{\pm} &= C^{\pm}\ \psi_a\ e^{-ik|z|}\ ,\quad z \neq 0\ , \end{aligned} \qquad (96)$$

where $\langle U \rangle^{+}$ and $\langle U \rangle^{-}$ are the normally upward and downward going plane waves characterized by the coherent reflection coefficient C^{+} and the quasi transmission coefficient C^{-} (the coherent transmission coefficient is $1 + C^{-}$), respectively. The picture of the average scattered field $\langle U \rangle$ is shown in Figure 40.

However, the coherent field $\langle \psi \rangle$ on the bottom plane, i.e. $z = 0$, is a constant attributed to both halves of the upward and downward going waves (including the incoming wave) and can be reasonably written as an average of up-going and down-going waves at $z = 0$ [43]

$$\begin{aligned} \langle \psi(\vec{r}_j) \rangle &= \langle \psi_i \rangle|_{(x_j,y_j,0)} + \left.\frac{\langle U \rangle^{+} + \langle U \rangle^{-}}{2}\right|_{(x_j,y_j,0)} \\ &= \psi_a + \left(\frac{C^{+} + C^{-}}{2}\right) \psi_a \end{aligned} \qquad (97)$$

Substituting the above equation into Eq. (95-a) yields

$$\langle U\rangle = \rho\,\psi_a \int E(\vec{R},\vec{r}_j)\,\langle\overline{f(a_j,\theta_j)}\left(1+\frac{C^+ + C^-}{2}\right)\rangle\, d\vec{r}_j \qquad (98)$$

At large distance from nodules ($k|\vec{R}-\vec{r}_j|>>1$), the far field expression for $E(\vec{R},\vec{r}_j)$ is $e^{-ik|\vec{R}-\vec{r}_j|}/|\vec{R}-\vec{r}_j|$. Using the polar integration as defined in Eq. (87) the average scattered field $\langle U\rangle$ becomes

$$\langle U\rangle = 2\pi\rho \int_0^\infty \frac{e^{-ik|\vec{R}-\vec{r}_j|}}{|\vec{R}-\vec{r}_j|}\,\langle\overline{f(a_j,\theta_j)}\left(1+\frac{C^+ + C^-}{2}\right)\rangle\, r_j\, dr_j \,.$$

The distance of $|\vec{R}-\vec{r}_j|$ is found to be $H/\cos\theta_j$ (see Figure 41 for the case $\vec{R} = (0,0,H)$). Therefore the above equation can be rewritten in terms of the θ integration as

$$\langle U\rangle = 2\pi\rho \int_0^\pi \Big\{\Big(1+\frac{C^-}{2}\Big)\,\overline{f(a_j,\theta_j)} + \frac{C^+}{2}\,\overline{f(a_j,\pi-\theta_j)}\, e^{-ikH/\cos\theta_j}\,(H\tan\theta_j/\cos\theta_j)\Big\} d\theta_j$$

$$= \frac{2\pi\rho}{-ik}\int_0^\pi \Big[\Big(1+\frac{C^-}{2}\Big)\,\overline{f(a_j,\chi)} + \frac{C^+}{2}\,\overline{f(a_j,\chi)}\Big]\, e^{-\chi}\, d\chi \,, \qquad (99)$$

where instead of $\overline{f(a_j,\theta_j)}$ the average scattering function $\overline{f(a_j,\pi-\theta_j)}$ is used to multiply $C^+/2$. The reason is that the excitation from $\langle U\rangle^+$ is opposite to the incoming wave and the scattering angle θ is therefore 180° different. In which $\chi = -ikH/\cos\theta_j$.

To solve Eq. (99) for $kH>>1$ (far field case) the principle of stationary phase [48] is used. The solution can thus be written in terms of the stationary phase angle γ as

$$\langle U\rangle = \frac{2\pi\rho\ [(1 + \frac{C^-}{2})\ \overline{f(a_j,\gamma)} + \frac{C^+}{2} f(a_j,\pi-\gamma)]}{-ik}\ e^{-ikH/\cos\gamma}\ . \qquad (99\text{-a})$$

The stationary phase angle γ is obtained by solving

$$\frac{d\chi}{d\theta_j} = \frac{-ikH \tan\theta_j}{\cos\theta_j} = 0$$

and found to be $n\pi$ ($n = 0,1,2,\ldots$) in this case.

One sees from the geometry (see Figure 40) that $\langle U\rangle^+$ can be solved, by integrating θ_j from 0 to $\pi/2$ (θ_j is the so-called meridian angle in the spherical coordinates and is defined as $0 < \theta_j < \pi/2$ for $z > 0$) using Eq. (99). The only appropriate phase angle in this region is zero so $\langle U\rangle^+$ is found to be, using Eqs. (95) and (96) at $z = H$,

$$\langle U\rangle^+ = \frac{2\pi\rho\ \psi_a}{-ik}\ [(1 + \frac{C^-}{2})\ \overline{f(a_j,0)} + \frac{C^+}{2}\ \overline{f(a_j,\pi)}]\ e^{-ikH} = C^+\ \psi_a\ e^{-ikH} \qquad (100)$$

By the same manner $\langle U\rangle^-$ is obtained as (θ_j is now in the region of $\pi/2$ and π and the phase angle is π),

$$\langle U\rangle^- = \frac{2\pi\rho\ \psi_a}{-ik}\ [(1 + \frac{C^-}{2})\ \overline{f(a_j,\pi)} + \frac{C^+}{2}\ \overline{f(a_j,0)}]\ e^{ikH} = C^-\ \psi_a\ e^{ikH} \qquad (101)$$

The two unknowns C^+ and C^- (i.e. coherent reflection and quasi transmission coefficient) can thus be solved simultaneously from Eqs. (100) and (101) using Cramer's rule and are as follows

$$C^+ = \beta_0/[1 - \beta_\pi + (\beta_\pi^2 + \beta_0^2)/4] \qquad (102)$$

$$C^- = (\beta_\pi - [(\beta_0^2 + \beta_\pi^2)/2])/[1 - \beta_\pi + (\beta_\pi^2 + \beta_0^2)/4]\ , \qquad (103)$$

where $\beta_0 = 2\pi\rho\ \overline{f(a_j,0)}/-ik$

$\beta_\pi = 2\pi\rho\ \overline{f(a_j,\pi)}/-ik$

After substituting the expressions for C^+ and C^- into Eqs. (100) and (101) respectively, U^+ and U^- become

$$\langle U\rangle^+ = [\beta_0 + \beta_0\beta_\pi + O(\beta_0^3)]\ \psi_a\ e^{-ikz} \quad , \quad z > 0 \qquad (100\text{-a})$$

$$\langle U\rangle^- = [\beta_\pi + \frac{1}{2}(\beta_\pi^2 + \beta_0^2) + O(\beta_\pi^3)]\ \psi_a\ e^{ikz} \quad , \quad z < 0 \qquad (101\text{-a})$$

The first term on the RHS of Eq. (100-a) (same for Eq. (101-a)) is due to the single scattering whose excitation is the incident plane wave ψ_i only. This can be done by substituting ψ_i $(z = 0)$ for $\langle\psi(\vec{r}_j)\rangle$ into Eq. (95-a). The second term is obtained using the self consistent approach which is essentially the Picard's process of successive approximations in the present case. Foldy [30] introduced this method to explain the orders of scattering since the higher order scattering is approximated by the iteration using the next lower order scattering. The idea is that the average scattered field $\langle U\rangle^+$ (or $\langle U\rangle^-$) can be obtained from a Newman series which is, in this case

$$\langle U(\vec{R})\rangle = u_1^{\pm} + \sum_{m=2}^{\infty} u_m^{\pm} \ , \qquad (104)$$

where $$u_m^{\pm} = \rho \int \overline{f(a_j,\theta_j)}\ \frac{(u_{m-1}^+(\vec{r}_j) + u_{m-1}^-(\vec{r}_j))}{2}\ \frac{e^{-ik|\vec{R}-\vec{r}_j|}}{|\vec{R}-\vec{r}_j|}\ d\vec{r}_j$$

and $u_1^+ = \beta_0\ \psi_a\ e^{-ikz} \quad , \quad z > 0$

$u_1^- = \beta_\pi\ \psi_a\ e^{ikz} \quad , \quad z < 0 \ .$

One can see from Eq. (104) that m=1, m=2 and m=3 correspond to single, double and triple scattering respectively.

To evaluate the contribution of each term (single, double, triple scattering) toward the average scattered field <U> the magnitudes of β_0 and β_π need to be decided. For the uniform size distribution, i.e. $\overline{f(a_j,\theta_j)} = f(a,\theta_j)$, both β_0 and β_π can be rewritten in terms of the reflectivity factor R_θ (Eq. (57)) as

$$\beta_{\theta=0,\pi} = \rho\pi a^2 \left[\frac{R_{\theta=0,\pi}}{-ika}\right] = \text{area coverage} \times O(1) \ .$$

The reason for this is that the magnitude of $R_{\theta=0}/ka$ is of order one (which can be seen from Figure 15 for a single Pacific nodule). For a sparse distribution, e.g. area coverage = 0.1, this implies that the successive term is about ten percent of the previous term in magnitude. Therefore the higher order scattering can be neglected in the approximation of the average scattered field <U> for a sparse distribution. As can be seen from Figure 42, there is almost no difference between the result of C^+ using only the first term (single scattering) in Eq. (100-a) and that with the second term correction.

B. Configurational Average of the Square of the Magnitude of the Wave Function, $<|\psi|^2>$

One sees from Eq. (78-a) that the incoherent component $<|\psi'|^2>$ is

$$<|\psi'|^2> = <|U|^2> - |<U>|^2$$

and the average of the square of the magnitude of the wave function $<|\psi|^2>$ is

$$\langle|\psi|^2\rangle = |\langle\psi\rangle|^2 + \langle|\psi'|^2\rangle \ .$$

Since the coherent component $|\langle\psi\rangle|^2$ can be obtained from the coherent field $\langle\psi\rangle$ in the previous section it is of interest to find here the incoherent component $\langle|\psi'|^2\rangle$ only.

Substituting the expression for U (Eq. (74-a)) into Eq. (78-a) yields

$$\langle|\psi'|^2\rangle = \langle\Sigma\ u_j^*\ \Sigma\ u_k\rangle - \Sigma\ \langle u_j\rangle^*\ \Sigma\ \langle u_k\rangle$$

$$= \sum_{j\neq k}\ \sum_{k}\ \langle u_j^*\ u_k\rangle + \sum_{j}\ \langle|u_j|^2\rangle - \sum_{j}\ \sum_{k}\ \langle u_j\rangle^*\ \langle u_k\rangle \ , \qquad (105)$$

in which $|\langle U\rangle|^2 = \langle U\rangle\ \langle U\rangle^*$ and $|U|^2 = U\ U^*$ are used. The above equation can also be written in the following form for scatterers of the same size (uniform size distribution)

$$\langle|\psi'|^2\rangle = \rho^2 \iint \left(\frac{N-1}{N}\ \langle u_j^*\ u_k\rangle_{jk} - \langle u_j\rangle_j^*\ \langle u_k\rangle_k\right) d\vec{r}_j\ d\vec{r}_k$$

$$+ \rho \int \langle|u_j|^2\rangle_j\ d\vec{r}_j \qquad (105\text{-a})$$

To get this one uses the previous definition for the configurational average, i.e.

$$\langle u_j\rangle = \frac{\rho}{N} \iint \langle u_j\rangle_j\ q(a_j)\ d\vec{r}_j\ da_j$$

To make the incoherent component $\langle|\psi'|^2\rangle$ easily calculable two approximations are introduced. First (N-1)/N is replaced by unity (valid for large N). Second the approximation

$$\langle u_j^*\ u_k\rangle_{jk} \sim \langle u_j\rangle_j^*\ \langle u_k\rangle_k \qquad (106)$$

suggested by Twersky [43] is used in Eq. (105-a). Eq. (106) may be

interpreted physically as neglecting contributrions to the excitations of a scatterer arising from the fluctuations of the average radiation scattered by the other scatterers. Finally the incoherent component $\langle|\psi'|^2\rangle$ becomes

$$\langle|\psi'|^2\rangle \simeq \rho \int \langle|u_j|^2\rangle_j \, d\vec{r}_j \ . \qquad (105\text{-b})$$

One sees from Eqs. (105-a) and (105) that actually $\sum_{j\neq k} \sum_k \langle u_j^* u_k\rangle$ can be approximated using $|\langle U\rangle|^2$. This fact implies that $\sum_{j\neq k} \sum_k \langle u_j^* \frac{\nabla}{-ik} u_k\rangle$, i.e. the average of the jth scattered field multiplied by the gradient of the kth scattered field (instead of a scalar it is a vector) can therefore be estimated as

$$\sum_{j\neq k} \sum_k \langle u_j^* \frac{\nabla}{-ik} u_\kappa\rangle^+ \simeq |\langle U\rangle^+|^2 \hat{e}_z \quad , \quad z > 0 \qquad (107)$$

$$\sum_{j\neq k} \sum_k \langle u_j^* \frac{\nabla}{-ik} u_k\rangle^- \simeq - |\langle U\rangle^-|^2 \hat{e}_z \quad , \quad z < 0 \qquad (108)$$

where $\hat{e}_z$ is the unit vector in the positive z direction. Recalling the expression for u_j (Eq. 86)) the gradient of u_j gives a radial direction. However the average direction should be in the z direction as expected from the symmetry of the problem (energy flux is cancelled out along x and y direction). Both Eqs. (107) and (108) are important approximations in considering the energy conservation which will appear in the next section.

C. The Configurational Average of Energy Flux, $\langle\vec{s}\rangle$

One sees from Eq. (79) that the configurational average of energy flux is

$$\langle \vec{s} \rangle = \omega \rho_0 k \, \mathrm{Re} \left\langle \frac{\psi^* \nabla \psi}{-ik} \right\rangle .$$

Substituting Eq. (74) for ψ into the above equation yields

$$\langle \vec{s} \rangle = \omega \rho_0 k \, \mathrm{Re} \left(\frac{\psi_i^* \nabla \psi_i}{-ik} + \frac{\psi_i^*}{-ik} \nabla \langle U \rangle + \frac{\langle U \rangle^* \nabla \psi_i}{-ik} + \frac{\langle U^* \nabla U \rangle}{-ik} \right) ,$$

in which the following relationship [30]

$$\langle \nabla U \rangle = \nabla \langle U \rangle$$

has been employed.

One expects $\langle \vec{s} \rangle$ for scattered waves to be going outward away from the plane of scatterers. Since the scattering characteristics are different in the positive z and negative z directions, it is necessary to separate $\langle \vec{s} \rangle$ into two parts for consideration. In other words

$$\langle \vec{s} \rangle = \langle \vec{s} \rangle^+ \quad , \quad z > 0 \tag{109}$$

$$\langle \vec{s} \rangle = \langle \vec{s} \rangle^- \quad , \quad z < 0 \tag{110}$$

The expressions for $\langle \vec{s} \rangle^+$ and $\langle \vec{s} \rangle^-$ are as follows,

$$\langle \vec{s} \rangle^+ = \omega \rho_0 k \, \mathrm{Re} \left(\frac{\psi_i^* \nabla \psi_i}{-ik} + \frac{\psi_i^*}{-ik} \nabla \langle U \rangle^+ + \frac{\langle U \rangle^{+*} \nabla \psi_i}{-ik} + \frac{\langle U^* \nabla U \rangle^+}{-ik} \right) \tag{109-a}$$

$$\langle \vec{s} \rangle^- = \omega \rho_0 k \, \mathrm{Re} \left(\frac{\psi_i^* \nabla \psi_i}{-ik} + \frac{\psi_i^*}{-ik} \nabla \langle U \rangle^- + \frac{\langle U \rangle^{-*} \nabla \psi_i}{-ik} + \frac{\langle U^* \nabla U \rangle^-}{-ik} \right) \tag{110-a}$$

On substituting the expressions for ψ_i, $\langle U \rangle^+$ and $\langle U \rangle^-$ (Eqs. (95) and (96)) into Eqs. (109-a) and (110-a) one obtains

$$\langle s \rangle^+ = \omega \rho_0 k \left[-\psi_a^2 \hat{e}_z + \mathrm{Re} \left(\frac{\langle U^* \nabla U \rangle^+}{-ik} \right) \right] \tag{109-b}$$

$$\langle s\rangle^{-} = \omega\rho_0 k\,[-\psi_a{}^2\,\hat{e}_z - \mathrm{Re}\,(C^{-} + C^{-*}\,\psi_a{}^2\,\hat{e}_z + \mathrm{Re}\,(\frac{\langle U^{*}\nabla U\rangle^{-}}{-ik})] \tag{110-b}$$

The second term on the RHS of Eq. (109-b) (or the third term on the RHS of Eq. (110-b) can further be separated into two parts

$$\frac{\langle U^{*}\nabla U\rangle^{\pm}}{-ik} = \sum_{j\neq k}\sum_{k}\langle u_j\,\frac{\nabla}{-ik}\,u_k\rangle^{\pm} + \sum_{j}\langle u_j\,\frac{\nabla}{-ik}\,u_j\rangle^{\pm}\,. \tag{109-c}$$

Using the above equation and Eqs. (107) and (108), the average energy flux $\langle\vec{s}\rangle^{\pm}$ becomes

$$\langle\vec{s}\rangle^{+} = \omega\rho_0 k\,[\psi_a{}^2\,(-\hat{e}_z) + \psi_a{}^2\,(|\langle U\rangle^{+}|^2\,\hat{e}_z + \vec{I}^{+}] \tag{109-d}$$

$$\langle\vec{s}\rangle^{-} = \omega\rho_0 k\,[\psi_a{}^2\,(-\hat{e}_z) + \psi_a{}^2\,\mathrm{Re}\,(C^{-} + C^{-*})(-\hat{e}_z)$$
$$+ \psi_a{}^2\,(|\langle U\rangle^{-}|^2)(-\hat{e}_z) + \vec{I}^{-}]\,, \tag{110-d}$$

where

$$\vec{I}^{+} = \mathrm{Re}\,(\sum_j\langle u_j{}^{*}\,\frac{\nabla}{-ik}\,u_j\rangle^{+}) = \mathrm{Re}\,(\frac{\rho}{-ik}\int\langle u_j{}^{*}\nabla u_j\rangle_j^{+}\,d\vec{r}_j)$$

$$\vec{I}^{-} = \mathrm{Re}\,(\sum_j\langle u_j{}^{*}\,\frac{\nabla}{-ik}\,u_j\rangle^{-}) = \mathrm{Re}\,(\frac{\rho}{-ik}\int\langle u_j{}^{*}\nabla u_j\rangle_j^{-}\,d\vec{r}_j)$$

The energy principle simply states that the mean energy outflow for nondissipative scatterers, from any enclosed volume vanishes [43], i.e.

$$\oint\langle\vec{s}\rangle\cdot d\vec{A} = 0\,.$$

In order to verify this a simple control volume is assumed (see Figure 43). For the upper plane ($z > 0$)

$$\int \langle \vec{s} \rangle^{+} \cdot d\vec{A} = \omega \rho_0 k \left[\psi_a^2 (-\hat{e}_z) + \psi_a^2 (|\langle u \rangle^{+}|^2)\, \hat{e}_z \right] \cdot \hat{e}_z + \omega \rho_0 k \int \vec{I}^{+} \cdot d\vec{A} \qquad (111)$$

For the lower plane ($z < 0$)

$$\int \langle \vec{s} \rangle^{-} \cdot d\vec{A} = \omega \rho_0 k\, \psi_a^2 [(-\hat{e}_z) + \mathrm{Re}\,(C^{-} + C^{-*})(-\hat{e}_z) + \mathrm{Re}\,(|\langle U \rangle^{-}|^2)(-\hat{e}_z)]\,(-\hat{e}_z) A + \omega \rho_0 k \int \vec{I}^{-} \cdot d\vec{A} \,. \qquad (112)$$

Actually one sees from Figure 43 that the total average energy flux (per area) is contributed from two parts. One is the coherent energy flux which has components either in the positive or negative z direction (no x and y directions). The other is the power scattered into all directions (specified by $\vec{e}_r$) and called the incoherent energy flux, i.e. $\vec{I}^{+}$ and $\vec{I}^{-}$. After adding Eq. (112) to (111) it gives

$$\oint \langle \vec{s} \rangle \cdot d\vec{A} = \omega \rho_0 k \left[\mathrm{Re}(C^{-} + C^{-*}) + \mathrm{Re}\,(|\langle U \rangle^{+}|^2 + |\langle U \rangle^{-}|^2)\, \psi_a^2 \right] + \omega \rho_0 k \oint \vec{I} \cdot d\vec{A} \qquad (113)$$

The term $u_j^* \frac{\nabla}{-ik} u_j$ appeared in $\vec{I}^{+}$ and $\vec{I}^{-}$ (Eq. (110-d)) is the $p_s p_s^*$ term related to the scattering cross section σ in the first part. Recalling that, for the single scattering case,

$$u_j = f(a_j, \theta_j) \frac{e^{-ik|\vec{R}-\vec{r}_j|}}{|\vec{R}-\vec{r}_j|} \psi_a \quad .$$

Then u_j and u_j^* become, respectively

$$\nabla u_j = \frac{\partial u_j}{\partial R} = -ik\, f(a,\theta) \frac{e^{-ik|\vec{R}-\vec{r}_j|}}{|\vec{R}-\vec{r}_j|} \psi_a + O\left(\frac{1}{|\vec{R}-\vec{r}_j|^2}\right)$$

$$u_j^* = f^*(a_j,\theta_j)\,\frac{e^{ik|\vec{R}-\vec{r}_j|}}{|\vec{R}-\vec{r}_j|}\,\psi_a \ .$$

Neglecting the higher order term ($\frac{1}{|\vec{R}-\vec{r}_j|^2} \ll 1$, for $k|\vec{R}-\vec{r}_j| \gg 1$) finally one sees, using Eq. (42) for $p_a = \psi_a$,

$$u_j^* \frac{\nabla}{-ik} u_j = p_s p_s^* \tag{114}$$

The above equation links the incoherent energy flux to the scattering cross section σ defined as (see Eq. (44-a))

$$\sigma = \frac{\int_0^{4\pi} |p_s|^2 R^2 \, d\Omega}{p_a^2}$$

as follows

$$\frac{1}{\psi_a^2} \int \vec{I}^+ \cdot d\vec{A} = \rho\sigma^+$$

$$\frac{1}{\psi_a^2} \int \vec{I}^+ \cdot d\vec{A} = \rho\sigma^- \tag{115}$$

$$\frac{1}{\psi_a^2} \oint \vec{I} \cdot d\vec{A} = \rho(\sigma^+ + \sigma^-) = \rho\sigma \ ,$$

in which σ^+ and σ^- are defined in the first part (see Eqs. (45-a) and (46-a)).

After dividing Eq. (113) by $\psi_a^2/\omega\rho_0 k$ and neglecting the terms $|\langle U\rangle^+|^2$ and $|\langle U\rangle^-|^2$ (of order $|C^\pm|^2$ which are small compared with $|C^\pm|$) Eq. (113) becomes

$$\oint \langle \vec{s} \rangle \cdot d\vec{A} = \mathrm{Re}\,(C^{-} + C^{-*}) + \rho\sigma \ . \qquad (113\text{-a})$$

The first term on the RHS of Eq. (113-a) becomes, using Eqs. (102) and (103),

$$\mathrm{Re}\,(C^{-} + C^{-*}) = \frac{-4\pi\rho}{k}\,\mathrm{Im}\,(f(a,\pi)) \ . \qquad (113\text{-b})$$

Substituting the above equation back into Eq. (113-a) one sees, using the forward scattering theorem (Eq. (44-e)),

$$\oint \langle \vec{s} \rangle \cdot d\vec{A} = \rho(\sigma - \frac{4\pi}{k}\,\mathrm{Im}\,(f(a,\pi)) = 0 \qquad (113\text{-c})$$

The above equation states that the energy flux coherently transmitted is cancelled out by that incoherently scattered which verifies the energy principle for nonabsorbing scatterers mentioned by Twersky [43].

D. Radial Distribution Function Consideration

The previous investigation of the multiple scattering of waves is for sparse distributions in which the wave function ψ depends only on the area number density of the nodules and not on the relative location of nodule pairs. If ψ depends on the joint statistics of two different nodules j and k, then the radial distribution function f(R) needs to be introduced especially for dense distributions. The radial distribution function describes the pair statistics between two nodules. However, instead of going into the detail of the radial distribution function f(R) for the nodule field which at the present time still does not give a complete information (no closed form like the Rayleigh size

distribution has been found for this case), the effect of f(R) on the coherent field $\langle\psi\rangle$ will be discussed using a rather simple function represented f(R).

Starting from a simplified form of the radial distribution function f(R) defined as, i.e. a step function, (see Figure 44),

$$\begin{aligned} f(R) &= 0 \quad , \quad R < d \\ f(R) &= 1 \quad , \quad R \geq d \end{aligned} \tag{116}$$

where R is the distance between the jth and kth nodule and d is the exclusion length (see Figure 45). The step function is modified from the radial distribution histogram (see Figure 27).

One now applies Eq. (116) to the coupled pair of Eqs. (80) and (81-a) to see its influence on the coherent field $\langle\psi\rangle$. In other words, the involved pair statistics requires only the first two equations in the Foldy-Lax hierarchy to estimate the average wave field in a dense distribution. However, more elaborate work may necessarily be used to find the higher order scattering effects using more equations (i.e. need higher order statistics) in the Foldy-Lax hierarchy.

Substituting Eq. (116) into Eq. (81-a) one obtains

$$\begin{aligned} \langle\psi^j(\vec{R})\rangle_j &= \psi_i(\vec{r}_j) + \rho \int \overline{f(a_k,\theta_k)}\, E(\vec{R},\vec{r}_k)\, \langle\psi^k(\vec{r}_k)\rangle_k\, f(R)\, d\vec{r}_k \\ &= \psi_i(\vec{r}_j) + \rho\, \psi_a \int_d^\infty \overline{f(a_k,\theta_k)}\, \frac{e^{-ik|\vec{R}-\vec{r}_k|}}{|\vec{R}-\vec{r}_k|} \left(1 + \frac{C^+ + C^-}{2}\right) \\ &\quad \cdot 2\pi\, r_k\, dr_k \, . \end{aligned} \tag{81-b}$$

The above equation can be solved using the similar method in solving for $\langle U\rangle$ (section A in this chapter) and the result is, at z = H,

$$\langle\psi^j(\vec{R})\rangle_j^+ = \psi_i(\vec{R}) + C_d^+ e^{-ik\sqrt{H^2 + d^2}} \psi_a \ , \qquad (117)$$

where C_d^+ is now a function of θ_d ($C_d^+ = C^+(\theta-\theta_d)$) and θ_d is shown in Figure 44.

To obtain a first approximation of the coherent field $\langle\psi\rangle$ one may substitute Eq. (117) into (80) and neglect the near field effect happened in Eq. (81-b) when R approaches $\vec{r}_j$. This gives

$$\langle\psi(\vec{R})\rangle^+ = \psi_i(\vec{R}) + (\rho\psi_a \int \overline{f(a_j,\theta_j)} \frac{e^{-ik|\vec{R}-\vec{r}_j|}}{|\vec{R}-\vec{r}_j|} (1 + C_d^+) \, d\vec{r}_j) e^{-ikd}$$

$$= \psi_i(\vec{R}) + \beta_0 e^{-ikH}\psi_a + \beta_0\beta_\pi \, e^{-ikd} \, d^{-ikH} \, \psi_a + O(C^+C_d^+) \ . \qquad (118)$$

One sees from the above equation that for this case introducing the radial distribution function f(R) will shift the phase (seen by the term e^{-ikd}) of the second order term of $\langle U\rangle^+$ (Eq. (100-a)). The actual radial distribution function f(R) may be presented as a finer step function (or hopefully a continuous function) and a more rigorous effect in doing the integration is required. However, the principle is the same and a phase shift will be expected in the resulting coherent field $\langle\psi\rangle$.

XIII. SUMMARY AND CONCLUSIONS

Acoustic response from nodule deposits on the ocean bottom constitute a multiple scattering problem that is solved analytically. As can be seen from Figure 32, the highly resonant acoustic response in the high frequency region is able to be smoothed using the averaging technique which employs the Rayleigh size distribution function. The smoothed response representing a type of bottom acoustic signature may be used to compare with the in-situ measurements to infer abundance and mean sizes of nodules.

The narrow beam width of the spherical wave has little effect on the backscattered acoustic response. In general, the beam effect can be neglected or corrected for so that the plane wave excitation is adequate in doing the multiple scattering analysis for sounding the manganese nodules.

The Sumitomo's MFES system was based on a simplified scattering model and at-sea field calibration. The system may be refined and improved using the results of the more elaborate theoretical approach provided by this study.

The multiple scattering effect is found to be mainly the second order correction in evaluating the average scattered field. Its effect is small for a sparse distribution of nodules and therefore the magnitude of the scattered acoustic response can be simply computed from the single scattering analysis. The derived reflection and transmission coefficients are found depending on incident plane waves' frequency,

the area number density and the forward scattering and backscattering characteristics of a simple nodule. However, for a densely packed system, the multiple scattering effect, i.e. higher order terms for the average scattered field, becomes more important and is not negligible any more. The energy principle is applied to the multiple scattering of waves from the nodule field and the scattering process is shown to be energy conserved.

A shifted step function type radial distribution function was introduced in the average scattered field calculation when considering the pair statistics and using the first two equations in the Foldy-Lax hierarchy. The result shows that the pair correlation affects the phase of the second order correction term.

REFERENCES

1. Mero, J. L., "Potential Economic Value of Ocean Floor Manganese Nodule Deposits," in papers from a Conference on Ferromanganese Deposits on the Ocean Floor, ed. Horn, D. R., National Science Foundation, Washington, D.C., 1972, p. 186 and pp. 192-195.

2. Horn, D. R., B. M. Horn and M. N. Delack, "Distribution of Ferromanganese Deposits in the World Ocean," in papers from a Conference on Ferromanganese Deposits on the Ocean Floor, ed. Horn, D. R., National Science Foundation, Washington, D.C., 1972, pp. 9-17.

3. Kaufman, R., "Deep Ocean Mining - 1980 Status Report," Proceeding Ocean '80, Seattle, Washington, 1980 IEEE, pp. 49-54.

4. Speiss, F. N., "Ocean Remote Acoustic Sensing of the Sea Floor," in Vol. II of NOAA Workshop on Ocean Acoustic Remote Sensing, Chairman Murphey, S. R. and M. Schulkin. NOAA Office of Sea Grant, Rockville, Maryland, pp. 11-38.

5. Rayleigh, L., Theory of Sound, Dover Publications, Inc., New York, 1945, Vol. II, p. 282.

6. Anderson, A. L., "Sound Scattering from a Fluid Sphere," Journal of the Acoustical Society of America, Vol. 22, pp. 426-431, 1950.

7. Faran, J. J., "Sound Scattering by a Solid Cylinders and Spheres," Journal of the Acoustical Society of America, Vol. 23, pp. 405-418, 1951.

8. Hickling, R., "Analysis of Echoes from a Solid Elastic Sphere in Water," Journal of the Acoustical Society of America, Vol. 34, pp. 1582-1592, 1962.

9. Raab, W., "Physical and Chemical Features of Pacific Deep Sea Manganese Nodules and Their Implications to the Genesis of Nodules," in papers from a Conference on Ferromanganese Deposits on the Ocean Floor, ed. Horn, D. R., National Science Foundation, Washington, D.C., 1972, p. 32.

10. Love, A. E. H., The Mathematical Theory of Elasticity, Dover Publications, Inc., New York, 1944, pp. 56, 102 and 141.

11. Morse, P. M. and H. Feshback, Methods of Theoretical Physics, McGraw-Hill Book Company, Inc., New York, 1953, Part II, pp. 1759-1767.

12. Morse, P. M. and K. U. Ingard, Theoretical Acoustics, McGraw-Hill Book Company, Inc., New York, 1968, pp. 332-338 and 419-427.

13. Clay, C. S. and H. Medwin, Acoustical Oceanography, John Wiley & Sons, Inc., New York, 1977, pp. 180-183.

14. Abramowitz, M. and I. A. Stegun, Handbook of Mathematical Functions, 9th edition, Dover Publications, Inc., New York, 1972.

15. Gradshteyn, I. S. and I. M. Ryzhik, Tables of Integral Series and Products, Academic Press, New York, 1965, p. 795.

16. Landau, L. D. and E. M. Lifshitz, Fluid Mechanics, Pergamon Press, London, 1959, p. 297.

17. Neubauer, W. G., R. H. Vogt and L. R. Dragonette, "Acoustic Reflection from Elastic Spheres. I. Steady-State Signals," Journal of the Acoustical Society of America, Vol. 57, pp. 1123-1129, 1974.

18. Smith, K., Properties of Ocean Manganese Nodule Fields Relevant to a Remote Acoustical Sensing System, M.S. Thesis, Department of Aerospace and Ocean Engineering, Virginia Polytechnic Institute and State University, Blacksburg, Virginia, 1981.

19. Glasby, G. P., Marine Manganese Deposits, Elsevier Oceanography Series 15, Amsterdam, 1977, p. 359.

20. Greenslate, J., "Manganese Concentration Wet Density: A Marine Geochemistry Constant," in Marine Mining, ed. Moore, J. R., Crane, Russak & Company, Inc., New York, 1977, Vol. I, p. 125.

21. Stenzel, H., "On the Disturbance of a Sound Field Brought about by a Rigid Sphere," Elektrische Nachrichten Technik, Vol. 15, pp. 71-78, 1938.

22. Flex, L., L. R. Dragonette and H. Überall, "Theory of Elastic Resonance Excitation by Sound Scattering," Journal of the Acoustical Society of America, Vol. 63, pp. 723-731, 1978.

23. Überall, H., L. R. Dragonette and L. Flax, "Relation Between Creeping Waves and Normal Modes of Vibration of a Curved Body," Journal of the Acoustical Society of America, Vol. 61, pp. 711-715, 1977.

24. Dragonette, L. R., R. H. Vogt, L. Flax and W. G. Neubauer, "Acoustic Reflection from Elastic Spheres and Rigid Spheres and Spheroids. II. Transient Analysis," Journal of the Acoustical Society of America, Vol. 55, p. 1130, 1974.

25. Grubb, K. W., Sound Scattering Measurements from a Single Manganese Nodule, M.S. Thesis, Department of Aerospace and Ocean Engineering, Virginia Polytechnic Institute and State University, Blacksburg, Virginia, 1981.

26. Biot, M. A., "Theory of Propagation of Elastic Waves in a Fluid Saturated Porous Solid. I. Low Frequency Range," Journal of the Acoustical Society of America, Vol. 28, pp. 168-178, 1956.

27. Vogt, R. H., L. Flax, L. R. Dragonette and W. G. Neubauer, "Monostatic Reflection of a Plane Wave from an Absorbing Sphere," Journal of the Acoustical Society of America, pp. 558-568, 1975.

28. Hartmann, B. and J. Jarzynski, "Ultrasonic Hysteresis Absorption in Polymers," Journal of the Applied Physics, Vol. 43, p. 4304, 1972.

29. Vanderborck, G. and C. Rumelhard, "Diffraction d'une Onde Acoustique par un Solide de Revolution Inhomogene Plonge dans un Fluide," in Innovative Numerical Analysis for the Engineering Sciences, eds. Shaw, R., W. Pilkey, et al., University Press of Virginia, Charlottesville, Virginia, 1980, pp. 119-128.

30. Foldy, L. L., "The Multiple Scattering of Waves," Physical Review, Vol. 67, pp. 107-119, 1945.

31. Lax, M., "Multiple Scattering of Waves," Review of Modern Physics, Vol. 23, pp. 287-310, 1951.

32. Felix, D., "Some Problems in Making Nodule Abundance Estimates from Sea Floor Photographs," in Marine Mining, ed. Moore, J. R., Crane, Russak & Company, Inc., New York, Vol. 2, No. 3, 1980, pp. 293-303.

33. Twersky, V., "Coherent Electromagnetic Waves in Pair-Correlated Random Distributions of Aligned Scatterers," Journal of Mathematical Physics, Vol. 19, pp. 215-230, 1978.

34. Hong, K. M., "Multiple Scattering of Electromagnetic Waves by a Crowded Monolayer of Spheres: Application to Migration Imaging Films," Journal of the Optical Society of America, Vol. 70, pp. 821-826, 1980.

35. Croxton, C. A., Introduction to Liquid Physics, John Wiley and Sons, Inc., New York, 1975, pp. 80-81.

36. Korn, G. A. and T. M. Korn, Mathematical Handbook for Scientists and Engineers, 2nd ed., McGraw-Hill Book Company, New York, 1968, pp. 637-639 and 821.

37. Ishimaru, A., Wave Propagation and Scattering in Random Media, Academic Press, Inc., New York, 1978, Chap. 14.

38. Twersky, V., "Multiple Scattering of Radiation by an Arbitrary Configuration of Parallel Cylinders," Journal of the Acoustical Society of America, Vol. 24, pp. 42-45, 1952.

39. Lax, M., "Multiple Scattering of Waves, II. The Effective Field in Dense Systems," Physical Review, Vol. 85, pp. 621-629, 1951.

40. Biot, M. A., "Generalized Boundary Condition for Multiple Scatter in Acoustic Reflection," Journal of Acoustical Society of America, Vol. 44, pp. 1616-1698, 1968.

41. Twersky, V., "On the Non-Specular Reflection of Plane Waves of Sound," Journal of the Acoustical Society of America, Vol. 22, pp. 539-546, 1950.

42. Twersky, V., "On the Non-Specular Reflection of Sound from Planes and Absorbent Bosses," Journal of the Acoustical Society of America, pp. 336-338, 1951.

43. Twersky, V., "On Scattering and Reflection of Sound by Rough Surfaces," Journal of Acoustical Society of America, Vol. 29, pp. 209-225, 1957.

44. Mathur, N. L. and K. C. Yeh, "Multiple Scattering of Electromagnetic Waves by Random Scatterers of Finite Size," Journal of Mathematical Physics, Vol. 5, pp. 1619-1628, 1964.

45. Myers, J. J., C. H. Holm and R. F. McAllister, Handbook of Ocean and Underwater Engineering, McGraw-Hill Book Company, Inc., New York, 1969, Chap. 3, pp. 94-96.

46. Sommerfeld, A., Partial Differential Equations in Physics, Academic Press, New York, 1949.

47. Mganuson, A. H., K. Sundkvist, Y. Ma and K. Smith, "Acoustic Sounding for Manganese Nodules," 13th Offshore Technology Conference, Paper No. 4133, Houston, 1981.

48. Lamb, H., Hydrodynamics, 6th edition, Dover Publications, Inc., New York, 1932, p. 395.

49. McFarland, W. D., Development of a Reliable Method for Resource Evaluation of Deep-Sea Manganese Nodule Deposits Using Bottom Photographs, M.S. Thesis, Department of Geology, Washington State University, 1980.

Table 1. Elastic Constants for Beryllium and Armco Iron.

Material	Density (g /cc)	Poisson's ratio	Longitudinal(Compressional) velocity c_L(m/sec)	Transverse(Shear) velocity c_T(m/sec)
Beryllium	1.87	0.05	12890	8880
Armco Iron	7.70	0.29	5960	3240

The fluid outside the sphere is assumed to be water of density 1 g /cc and compressional velocity 1410 m/sec.

Table 2. Acoustical Properties of Manganese Nodules

CONCRETION TYPE	WAVE SPEEDS			DENSITY (g/cc)
	C_L (m/s)	C_T (m/s)	C_T/C_L	
PACIFIC NODULES	1950 - 2500 [2350]*	1615 - 2450 [2000]	0.83 - 0.98	1.91 - 1.96
ATLANTIC NODULES	2125 - 3215 [2605]	1625 - 2580 [1980]	0.69 - 0.80	1.89 - 2.07

* [ ] - average

Table 3. Values of c_L/c_0, c_T/c_0 and g used in the Sensitivity Test.

c_L/c_0	c_T/c_0	g	Related plots	Remark
1.7	1.57	1.94	Figs. 14-15	Pacific nodules
1.7	0	1.94	Fig. 16	Fluid sphere case
1.7	1.57	1.40	Fig. 17	Gladsby's "g" used
1.7	1.20	1.94	Fig. 18	Effect of rigidity

Table 4. Bottom Statistical Data Using Smith's Photograph Analysis

Description	Parameter	Unit	Derivation	Magnitude
Area Number Density	ρ	$1/m^2$		160
Average Apparent Radius	$\bar{a}$	cm	$\bar{a} = 1.078b^{1/2}$	2.94
Average Apparent Radius Squared	$\bar{a^2}$	cm^2	$\bar{a^2} = 1.253b$	9.30
Average Apparent Radius Qubed	$\bar{a^3}$	cm^3	$\bar{a^3} = 1.546b^{3/2}$	31.25
Average Mass of Single Pacific Nodule	$\bar{m}$	kg	$\rho_E(4/3)\pi\bar{a^3}$	0,25
Average Apparent Area Mass Density	$\bar{M}$	kg/m^2	$\rho\bar{m}$	40.63
Area Coverage	$\bar{A}$	—	$\rho\pi\bar{a^2}$	0.46
Rayleigh Size Distribution Parameter	b	cm^2		7.42
Pacific Nodule's Mass Density	ρ_E	g/cm^3		1.94

Table 5. Comparison between the Magnitudes of kH and $\alpha\delta^2$

Frequency	kH Calculation	δ_{HP}	$\alpha\delta^2$ Calculation
1kHz	20943	2°	2807
10kHz	209430	4°	701
100kHz	2094300	6°	312
H = 5000 m c = 1500 m/sec δ = 90 degree			

Table 6. Beam Width Correction Factor(α/kH)

	Half Power Beam Width δ_{HP}		
Frequency	1°	5°	10°
1 kHz	0.22	0.0087	0.0022
10 kHz	0.022	0.00087	0.00022
100 kHz	0.0022	0.000087	0.000022
H = 5,000 m = 15,000 ft c_0 = 1500 m/sec			

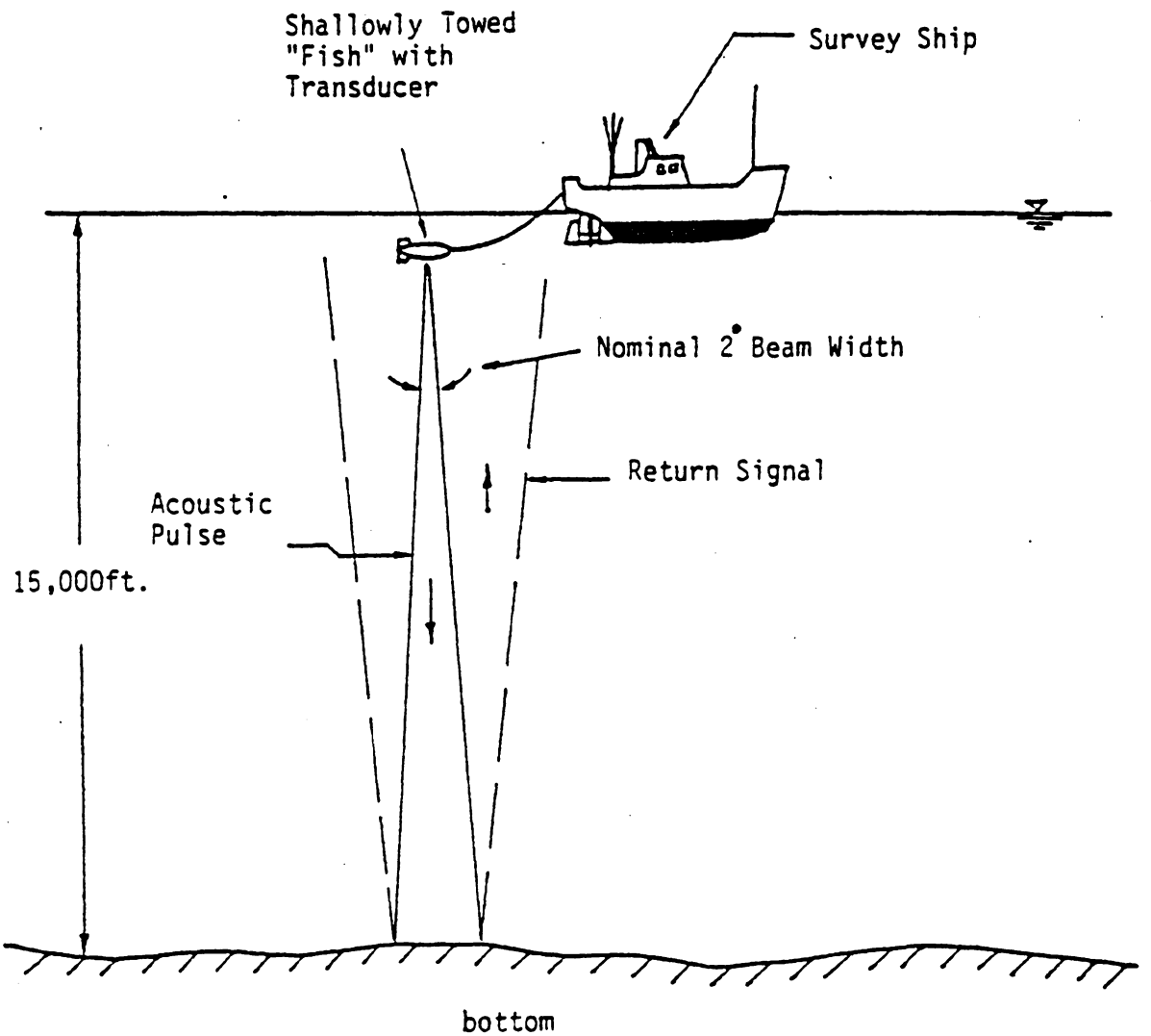

Figure 1. Proposed Prospecting System (Acoustic Sounding).

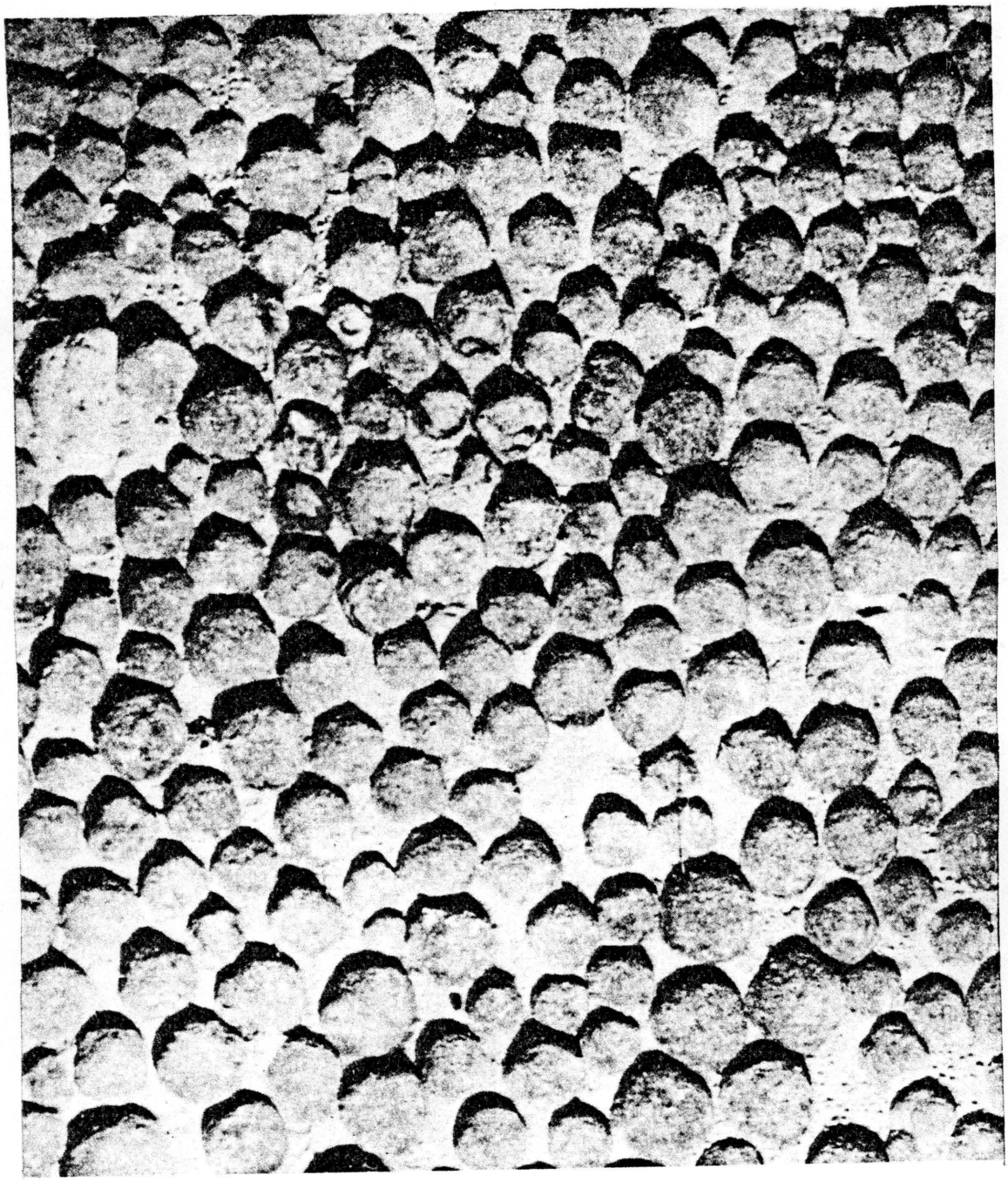

Figure 2. Seafloor Photograph of Ferromanganese Nodules, Depth 5320 m, Central South Pacific. (Courtesy of Lamont-Doherty Geological Observatory, Columbia University, Palisades, New York)

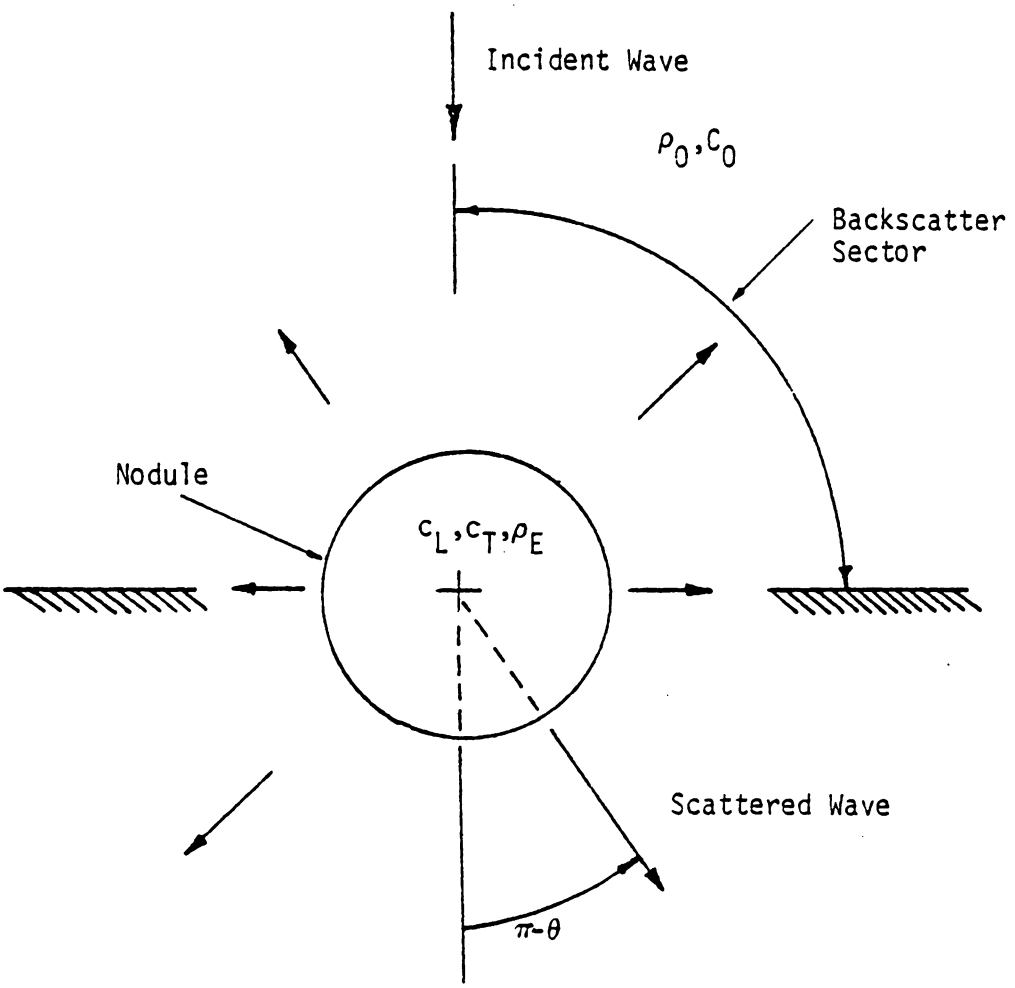

Figure 3. Scattering from Single Sphere.

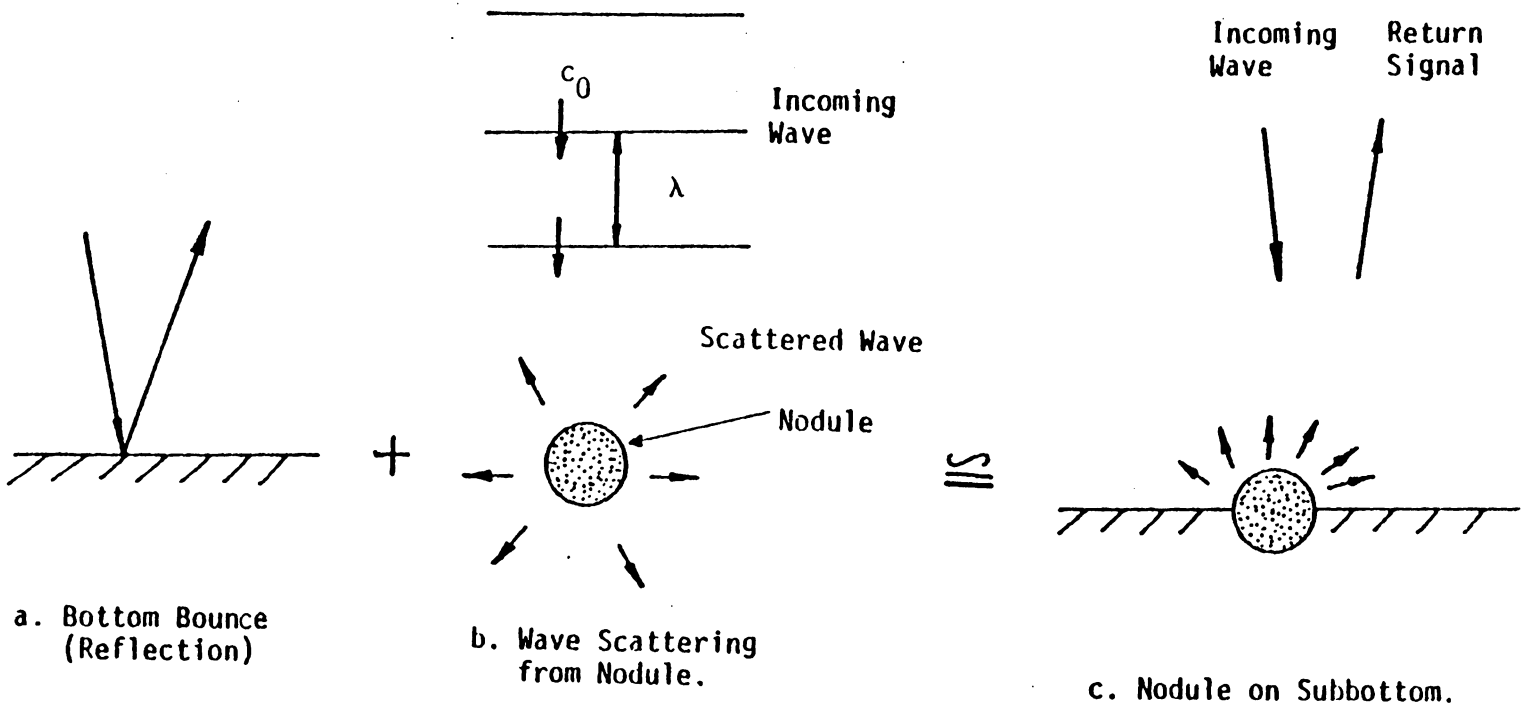

Figure 4. Simplified Model of Return Signal.

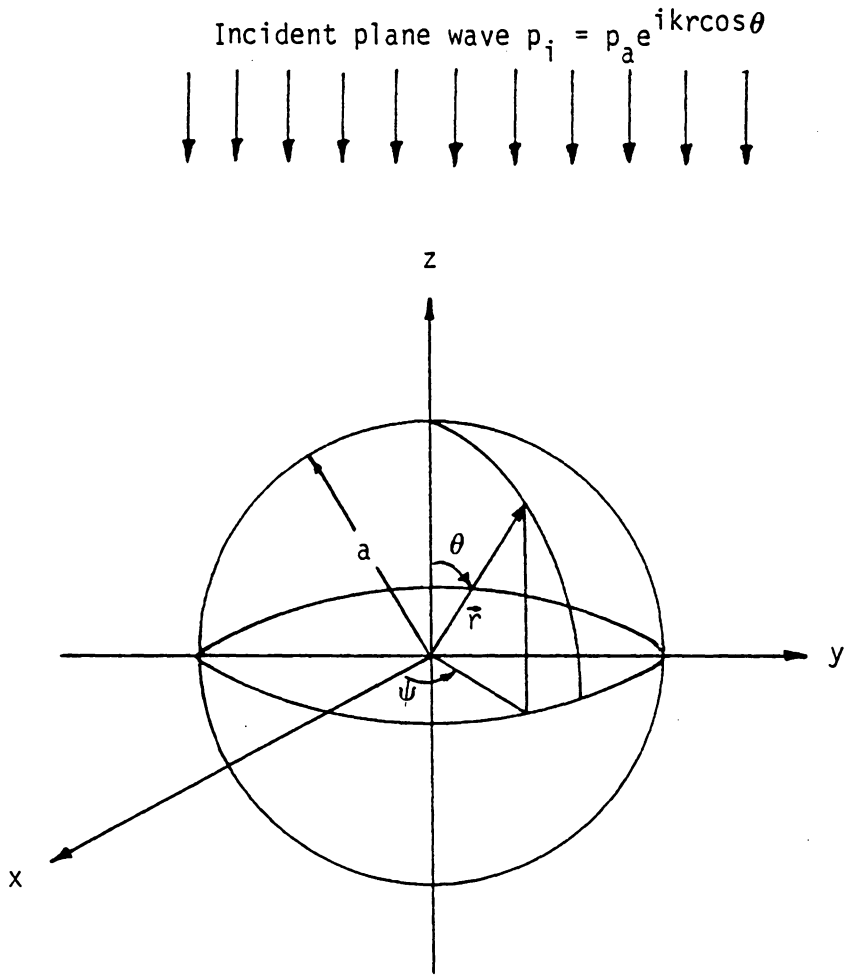

Figure 5. Choice of Coordinate Axes for Scattering by a Single Sphere.

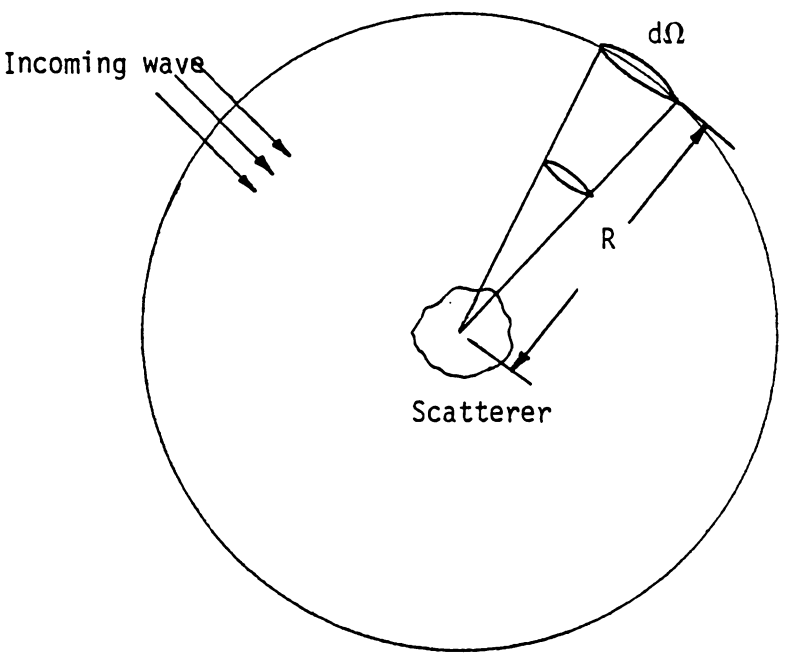

Figure 6. Schematic Representation of the Solid Angle.

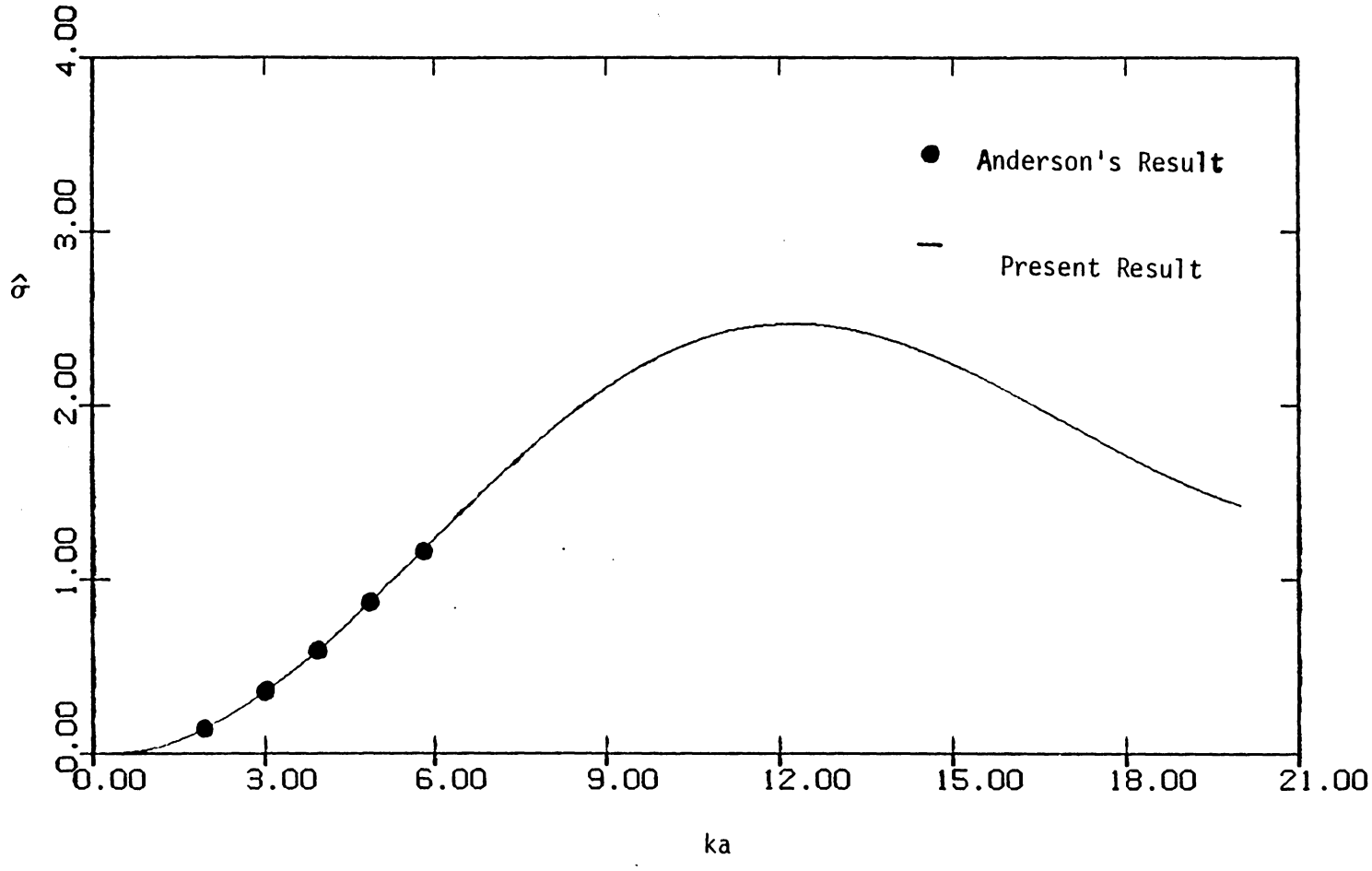

Figure 7. $\hat{\sigma}$ vs. ka for a Fluid Sphere(g = 1.0, h = 1.2).

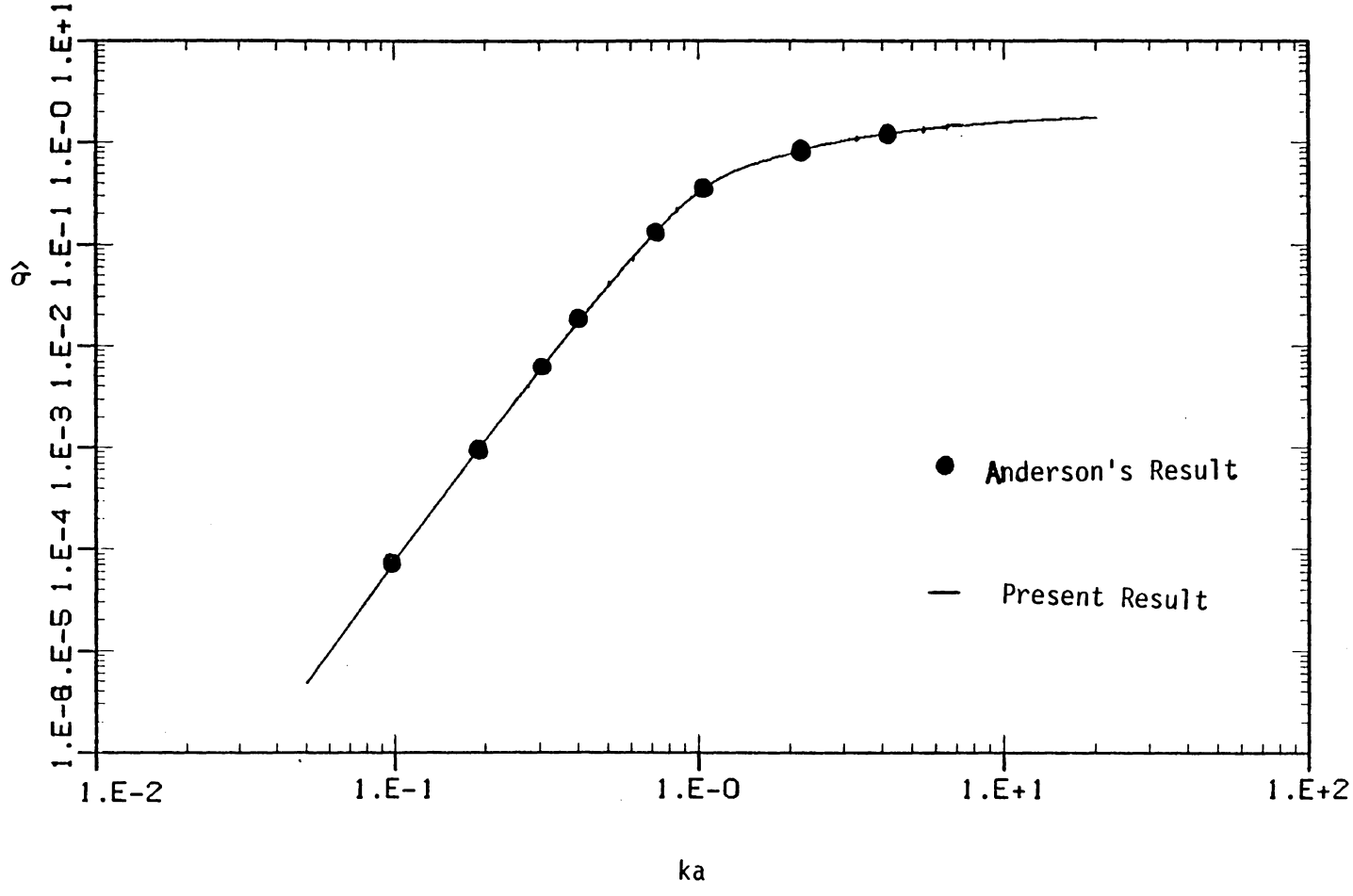

Figure 8. $\hat{\sigma}$ vs. ka for a Fixed Rigid Sphere.

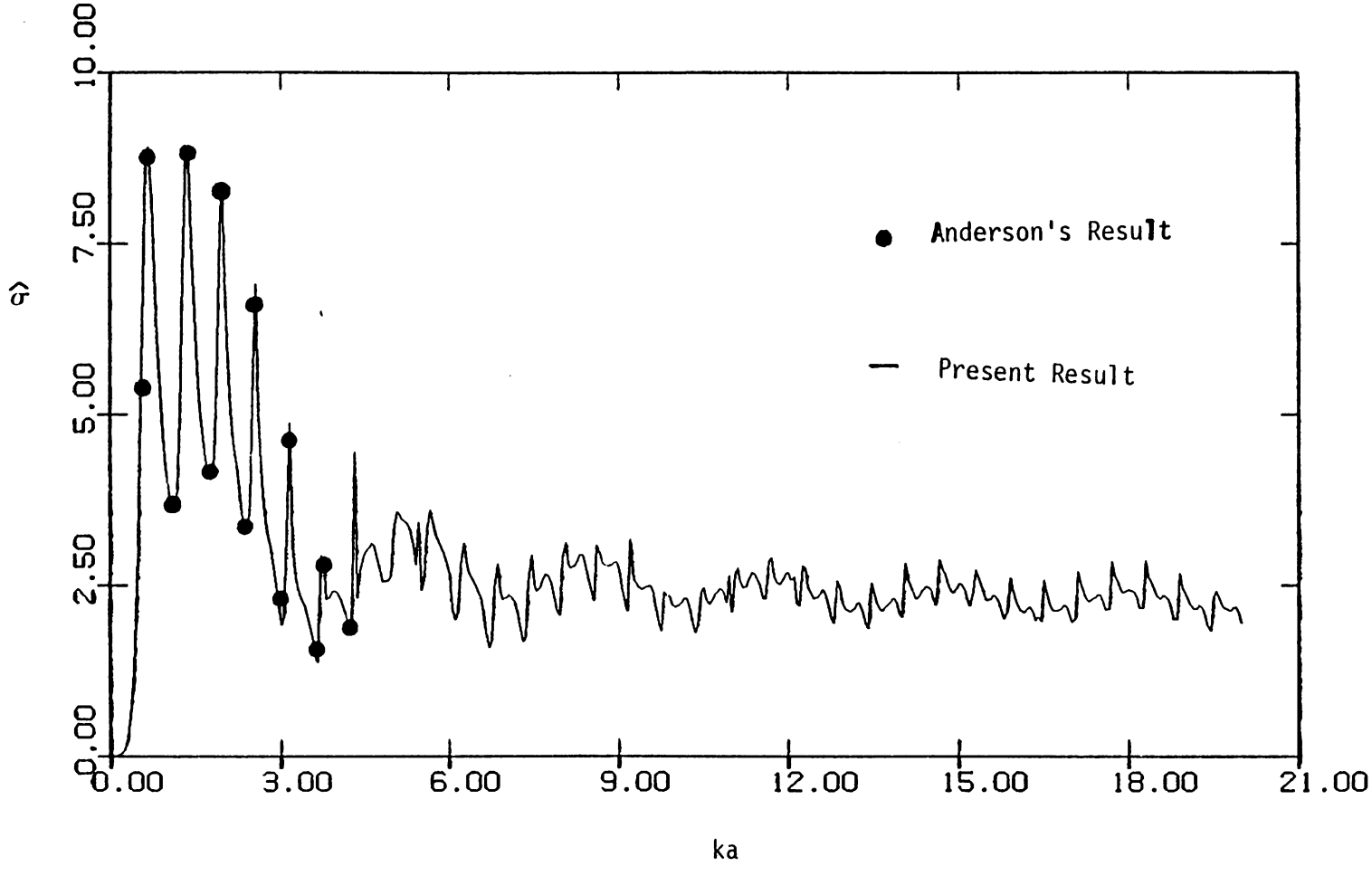

Figure 9. $\hat{\sigma}$ vs. ka for a Fluid Sphere(g = 0.5, h = 0.5)

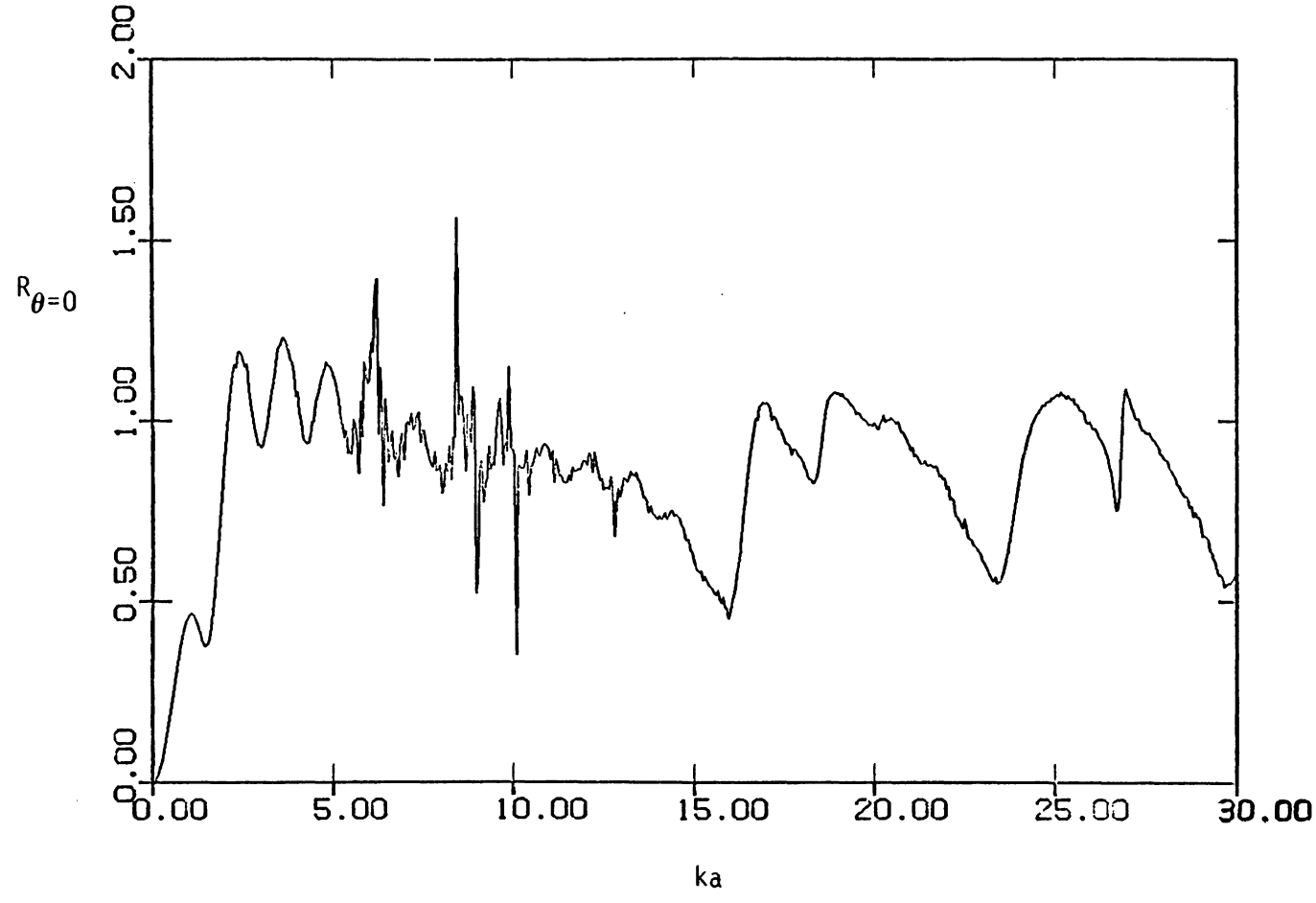

Figure 10. $R_{\theta=0}$ vs. ka for a Beryllium Sphere.

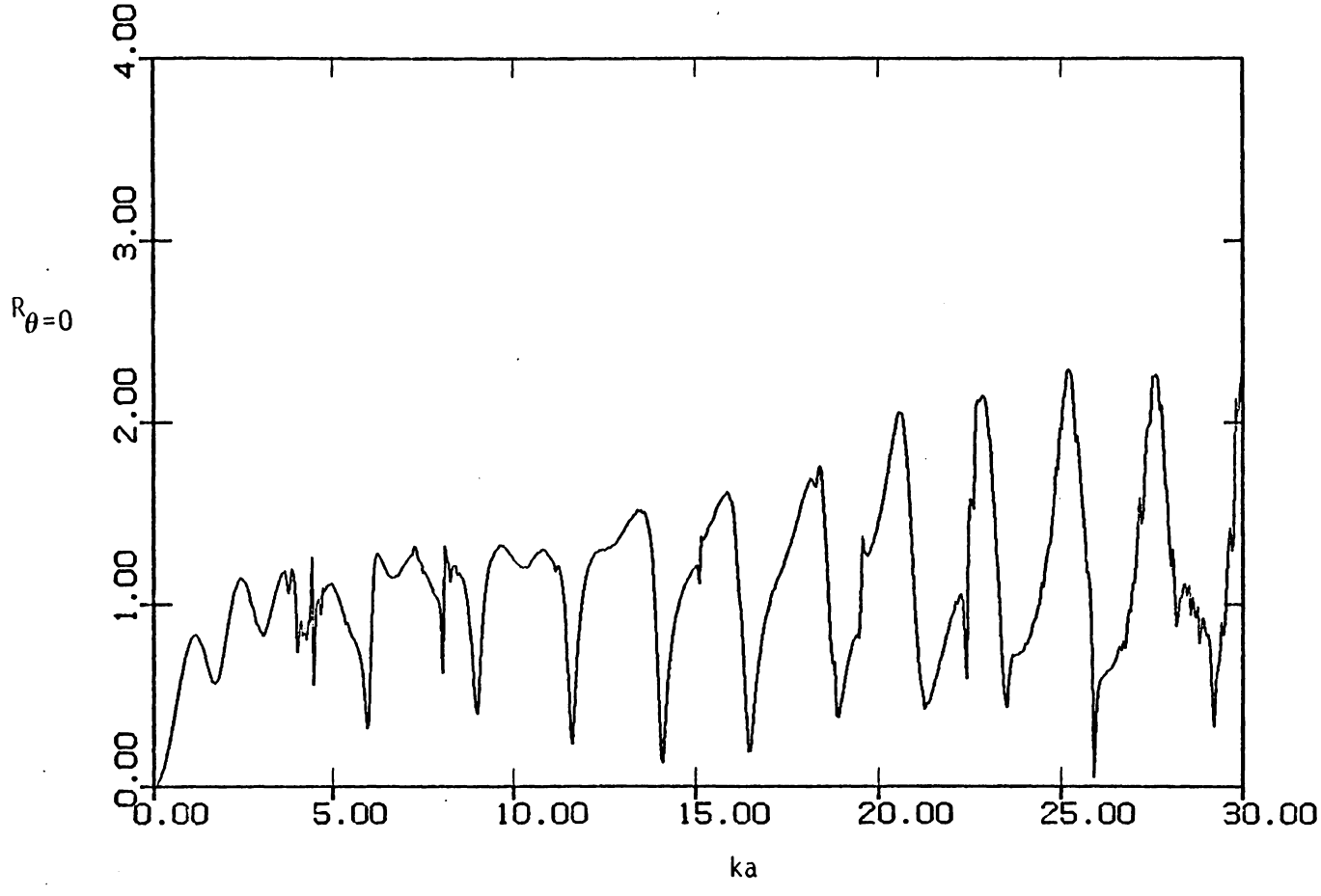

Figure 11. $R_{\theta=0}$ vs. ka for an Armco Iron Sphere.

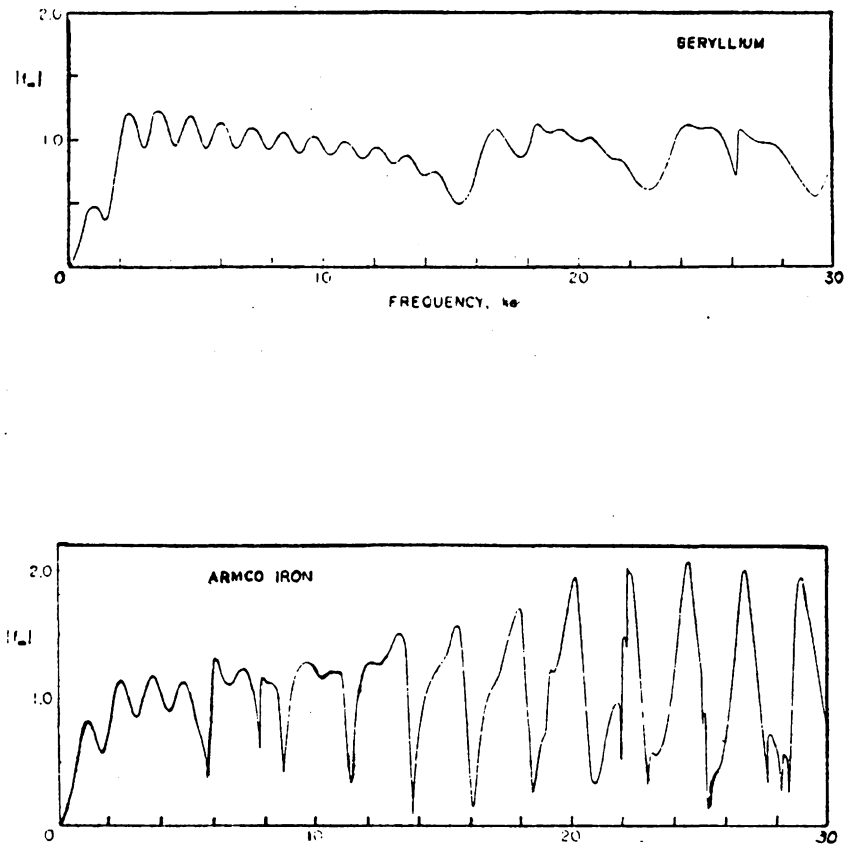

Figure 12. Results of $R_{\theta=0}$ vs. ka for Beryllium and Armco Iron Spheres from Hickling's Paper.

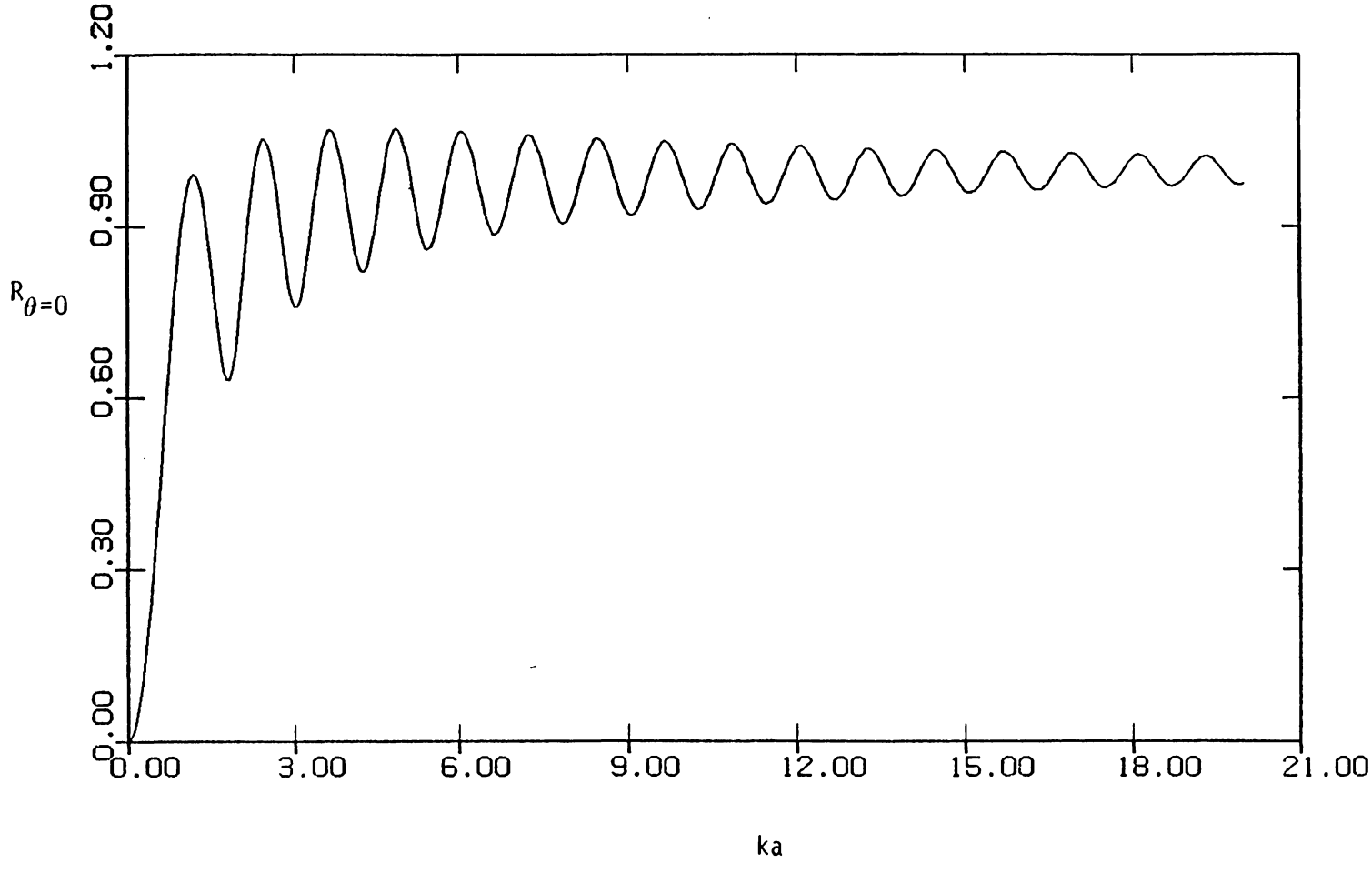

Figure 13. $R_{\theta=0}$ vs. ka for a Rigid Sphere.

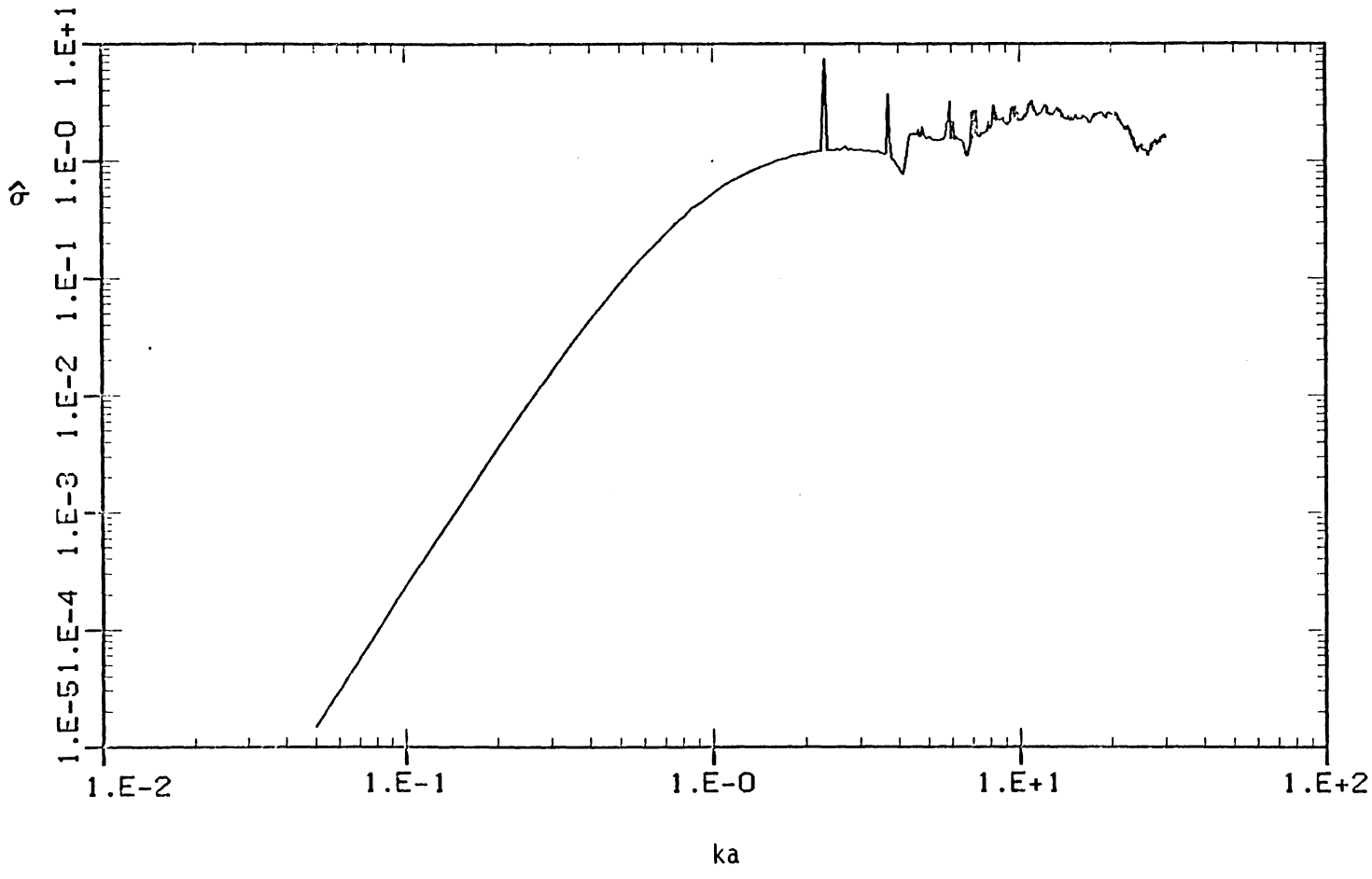

Figure 14. $\hat{\sigma}$ vs. ka for a Spherical Pacific Nodule(c_L/c_0 = 1.7, c_T/c_0 = 1.57, g = 1.94).

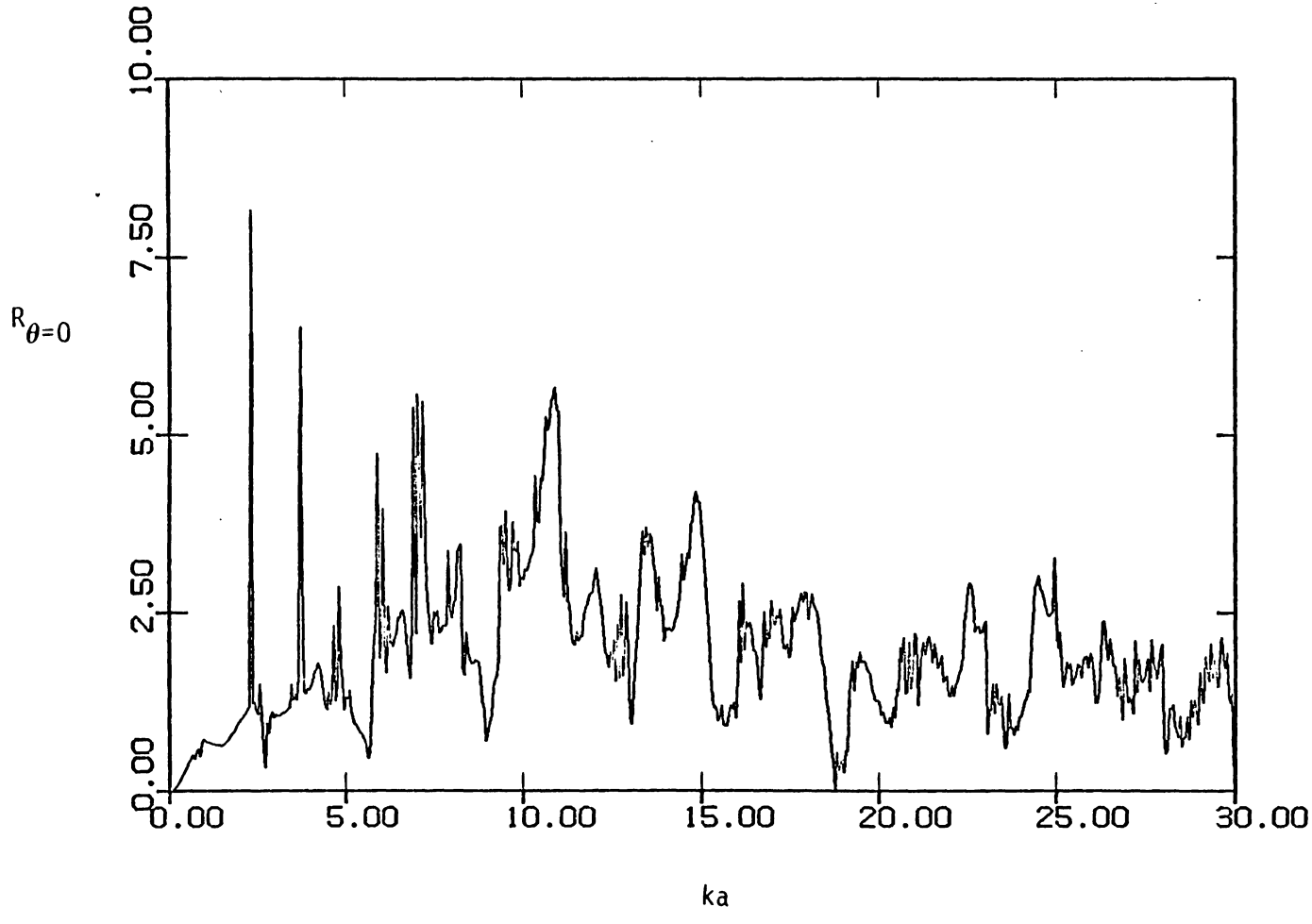

Figure 15. $R_{\theta=0}$ vs. ka for a Spherical Pacific Nodule(c_L/c_0 = 1.7, c_T/c_0 = 1.57, g = 1.94).

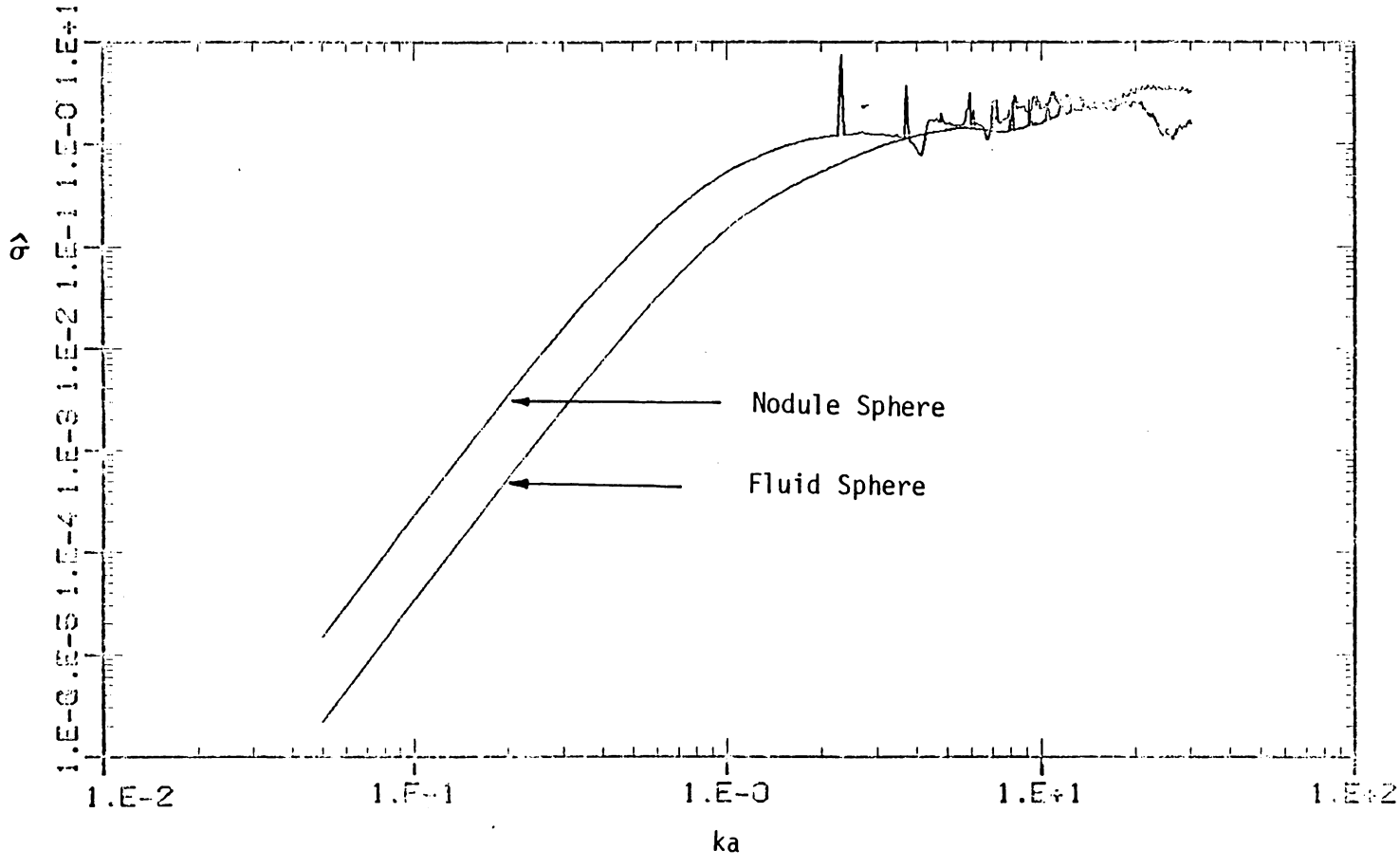

Figure 16. $\hat{\sigma}$ vs. ka for a Fluid Sphere(c_L/c_0 = 1.7, c_T/c_0 = 0, g = 1.94).

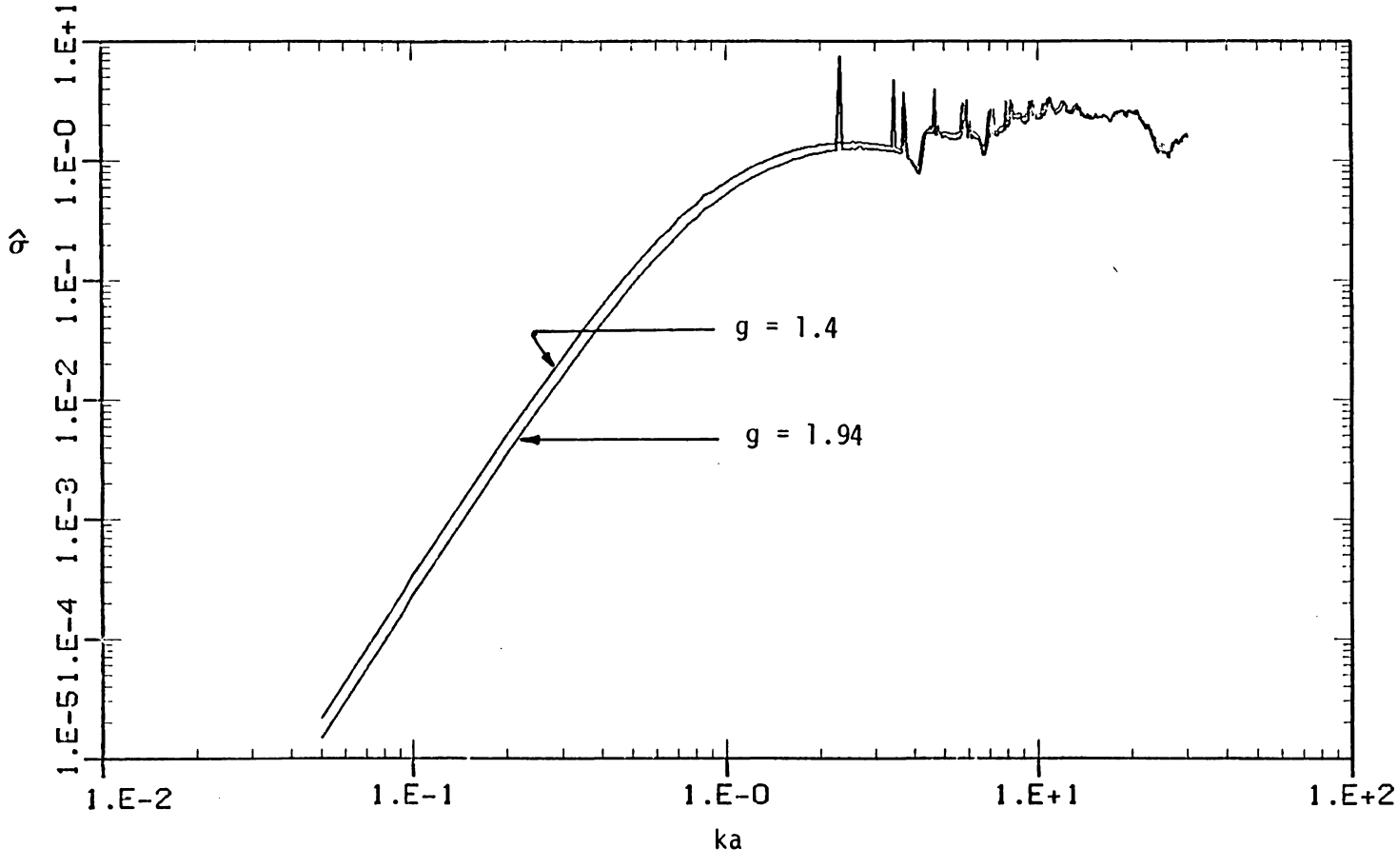

Figure 17. $\hat{\sigma}$ vs. ka for an Elastic Sphere(c_L/c_0 = 1.7, c_T/c_0 = 1.57, g = 1.4).

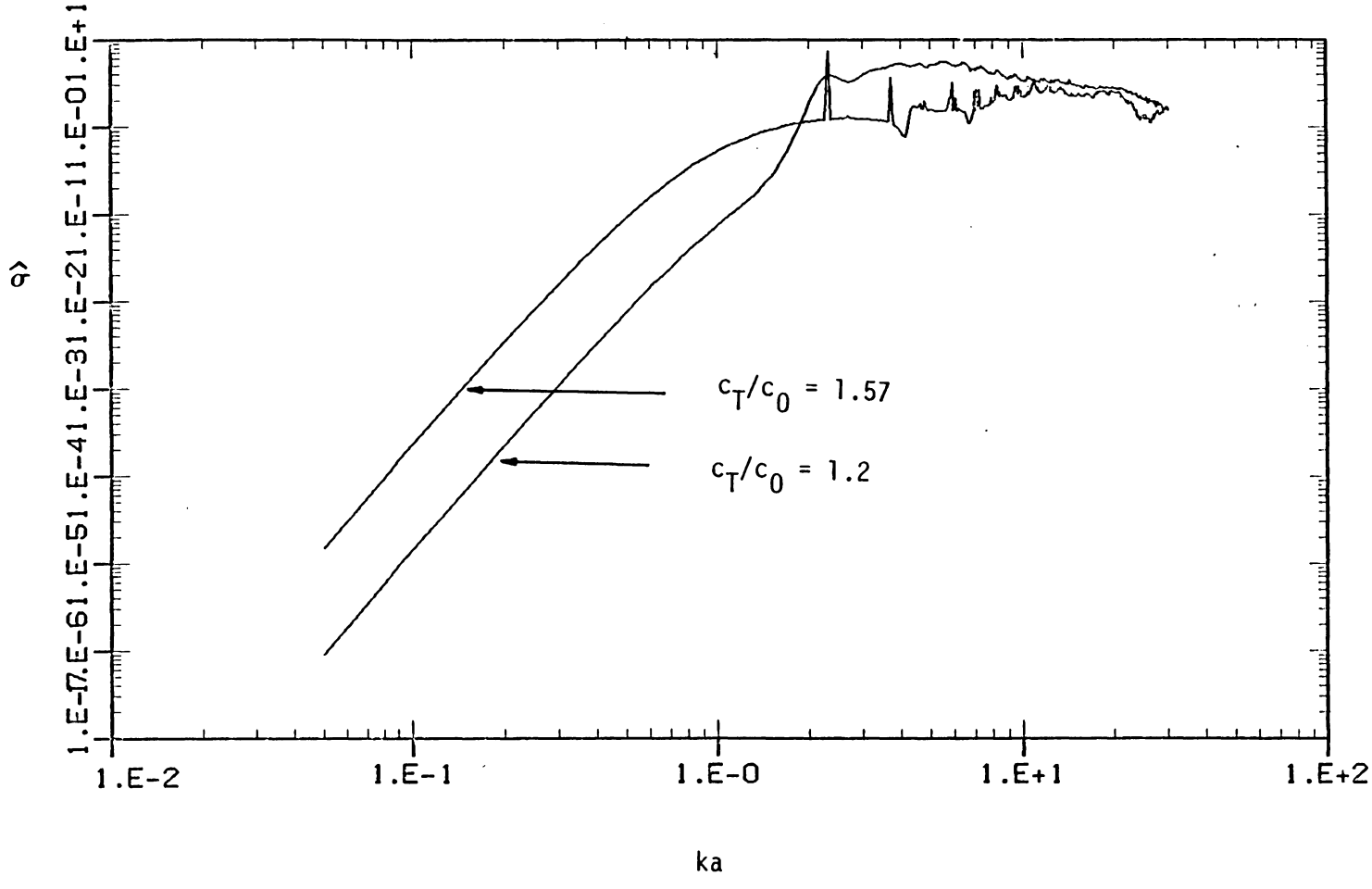

Figure 18. $\hat{\sigma}$ vs. ka for an Elastic Sphere(c_L/c_0 = 1.7, c_T/c_0 =1.2, g = 1.94).

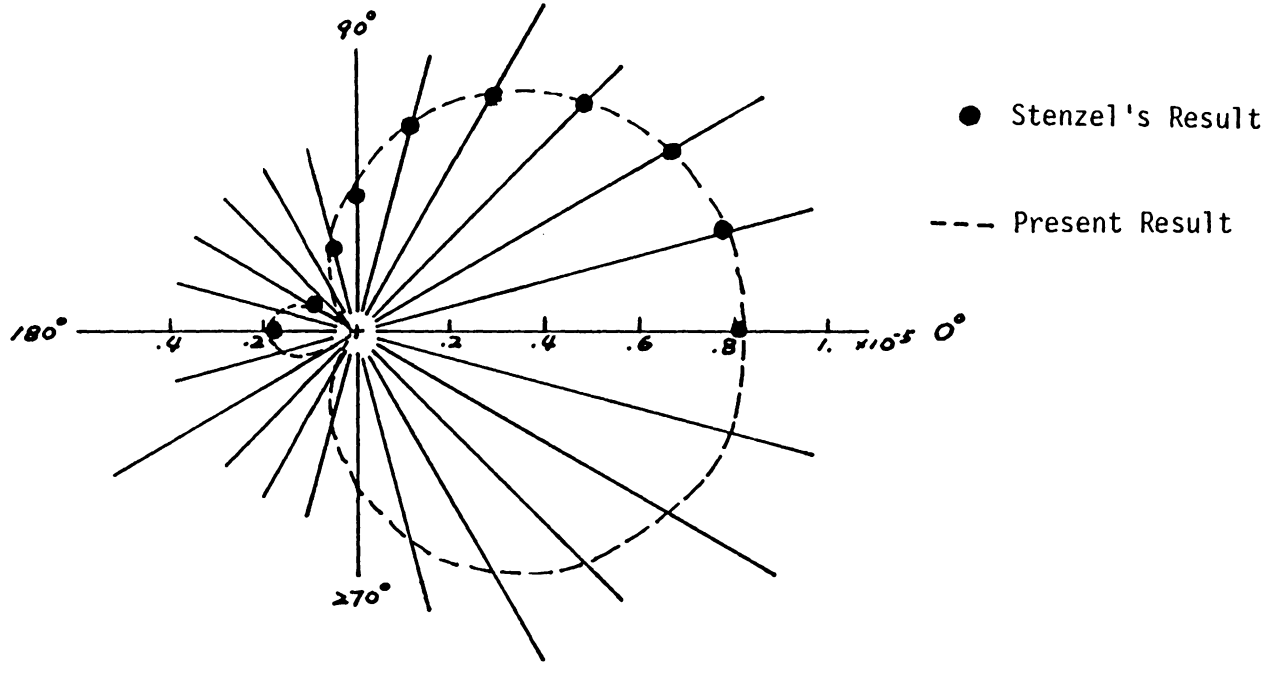

Figure 19. R_θ Polar of a Rigid Sphere for ka = 0.01

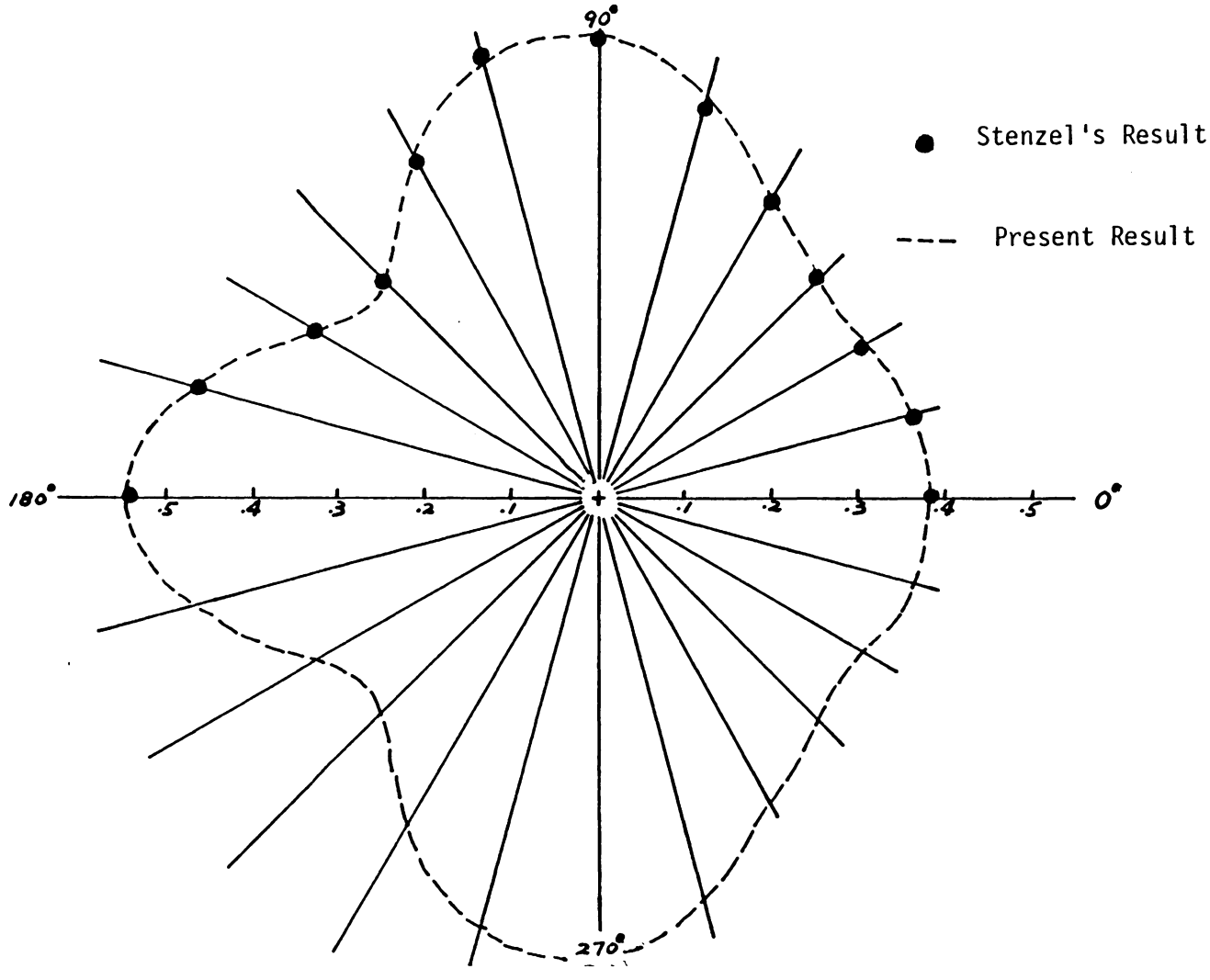

Figure 20. R_θ Polar of a Rigid Sphere for ka = 2.0

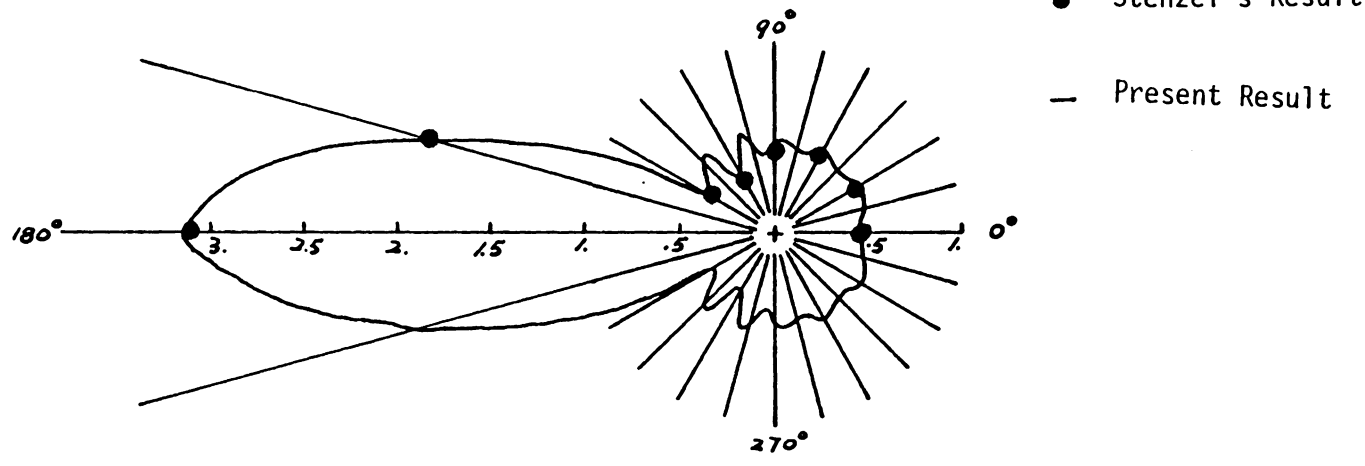

Figure 21. R_θ Polar of a Rigid Sphere for ka = 8.0

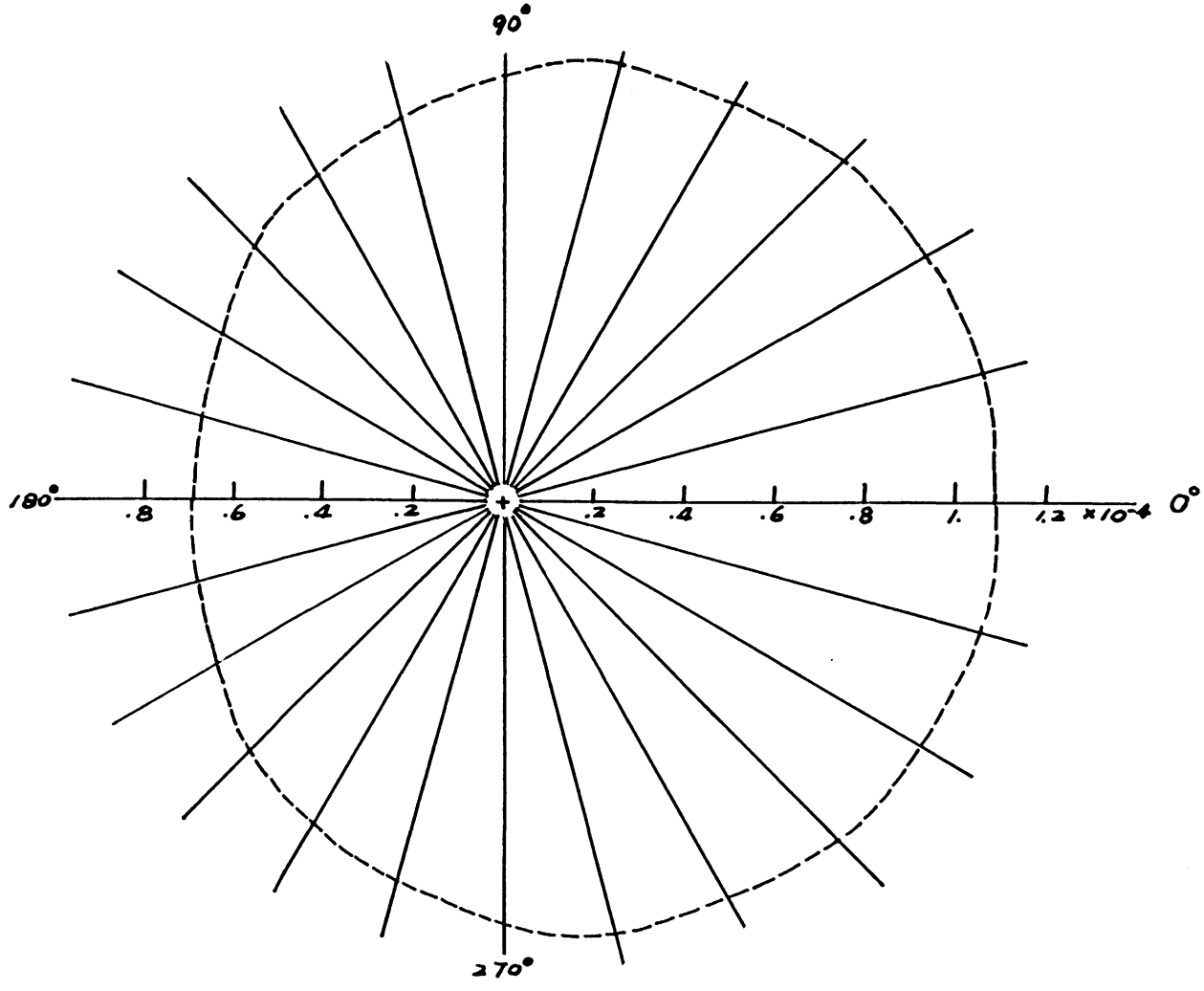

Figure 22. R_θ Polar of a Spherical Pacific Nodule for ka = 0.01

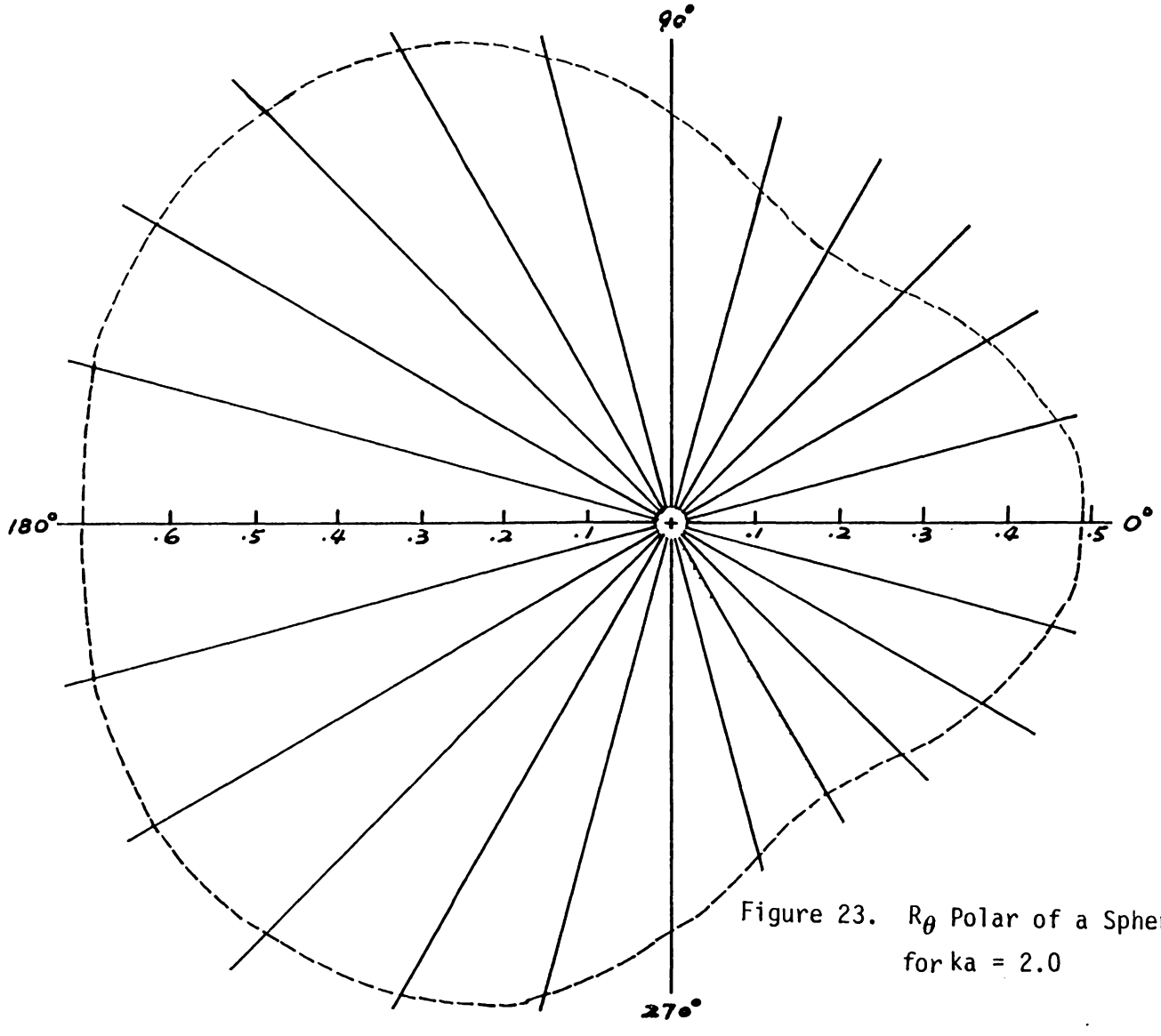

Figure 23. R_θ Polar of a Spherical Pacific Nodule for ka = 2.0

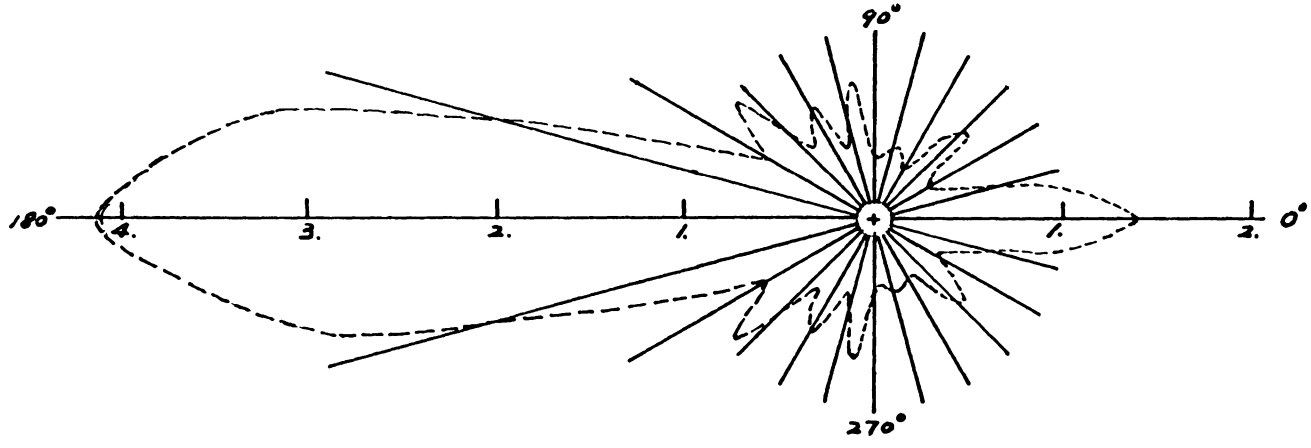

Figure 24. R_θ Polar of a Spherical Pacific Nodule for ka = 8.0

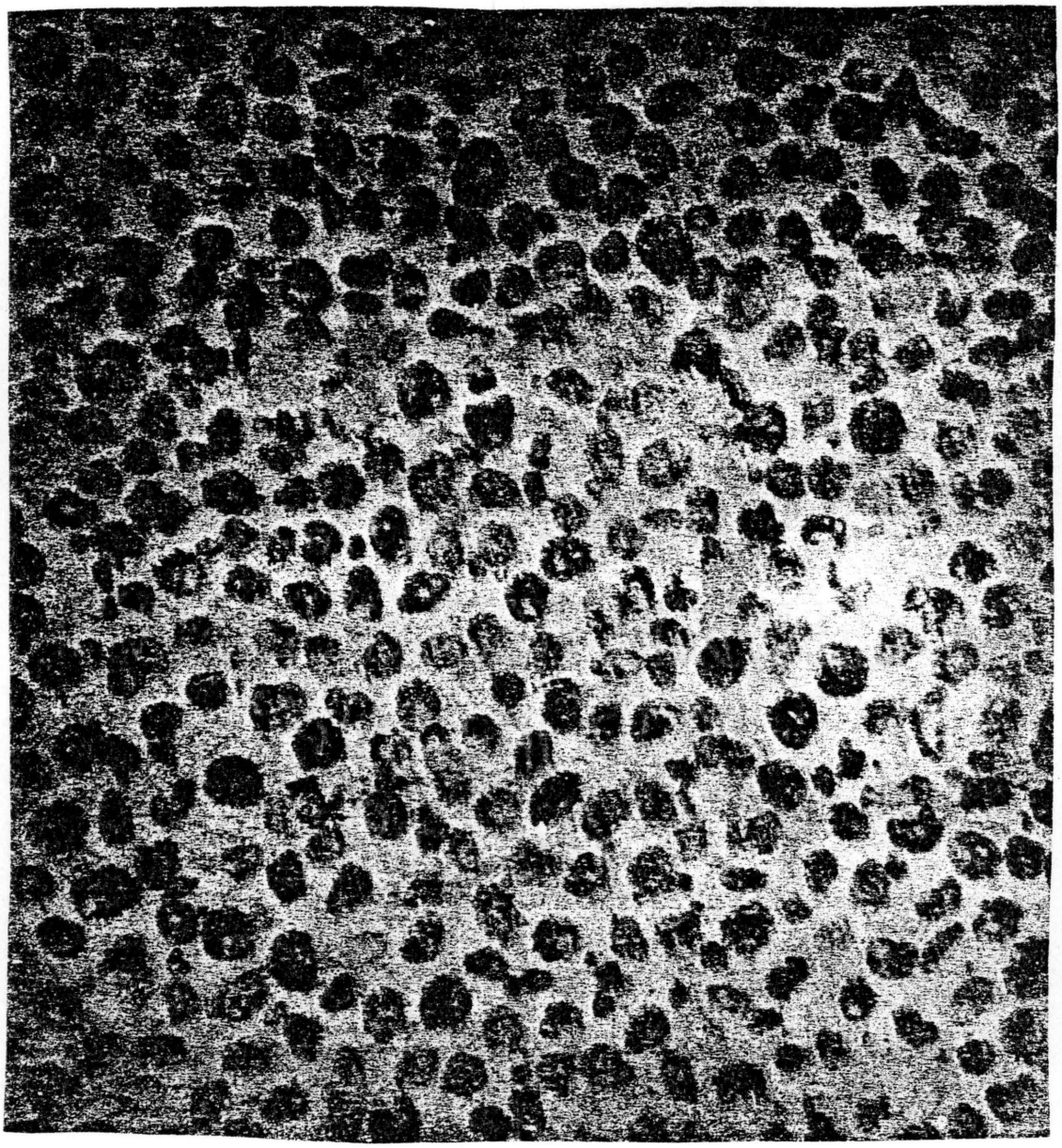

Figure 25. Typical Manganese Nodule Deposit on the Ocean Floor.
(Photo Courtesy of Deepsea Ventures, Inc.)

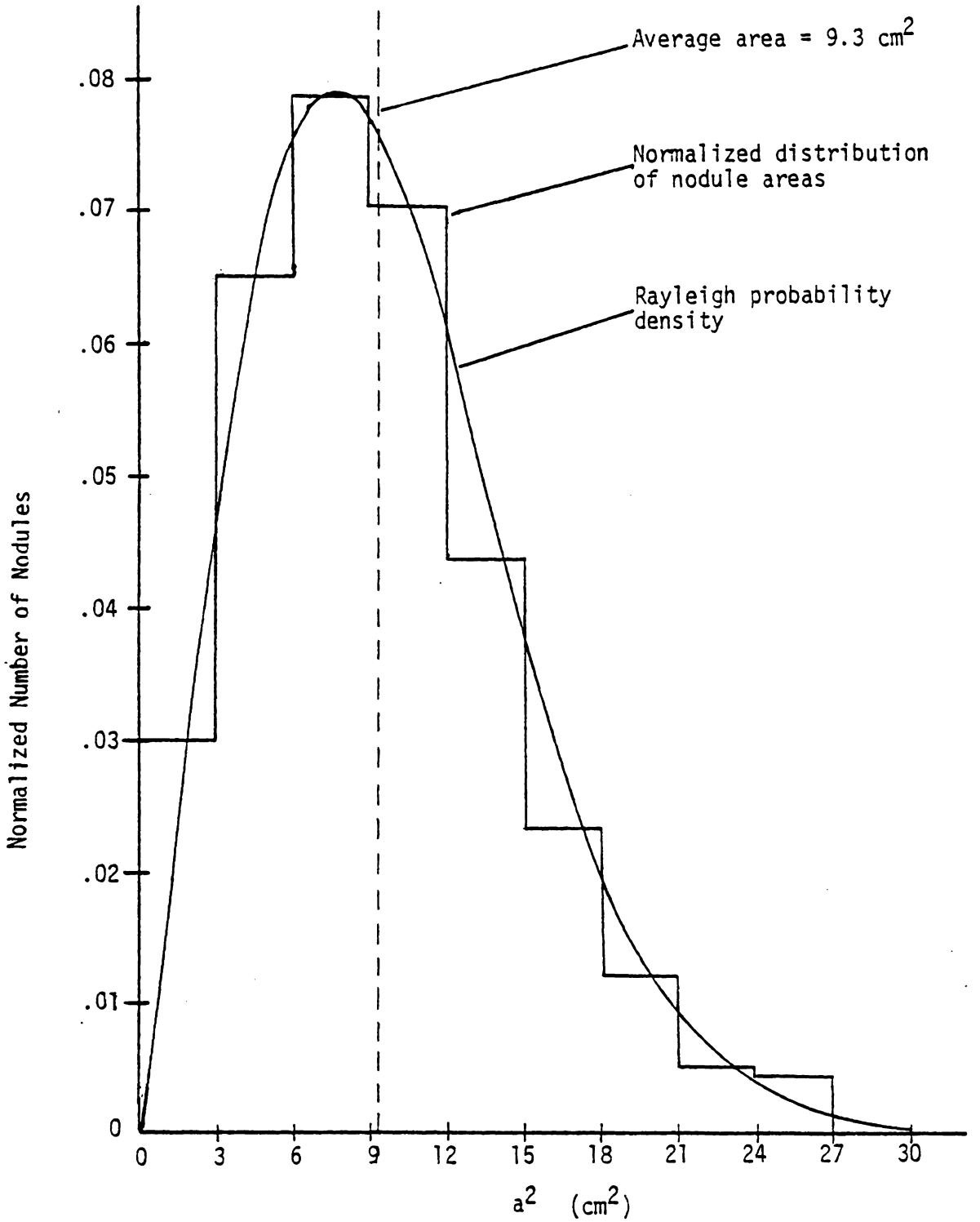

Figure 26. The Nodule Size Histogram.

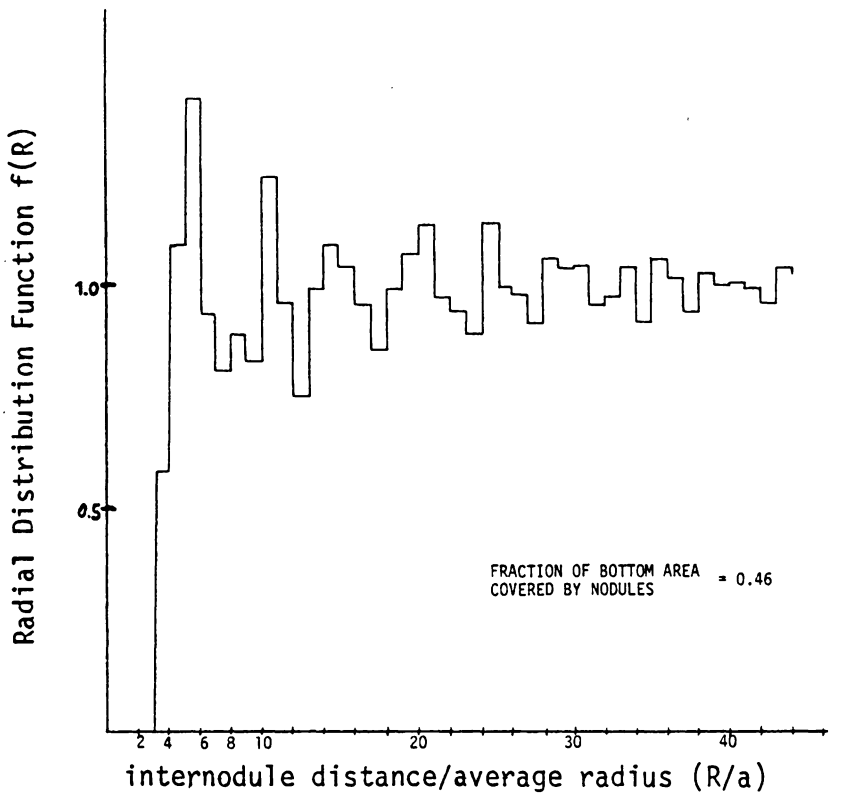

Figure 27. Radial Distribution Histogram.

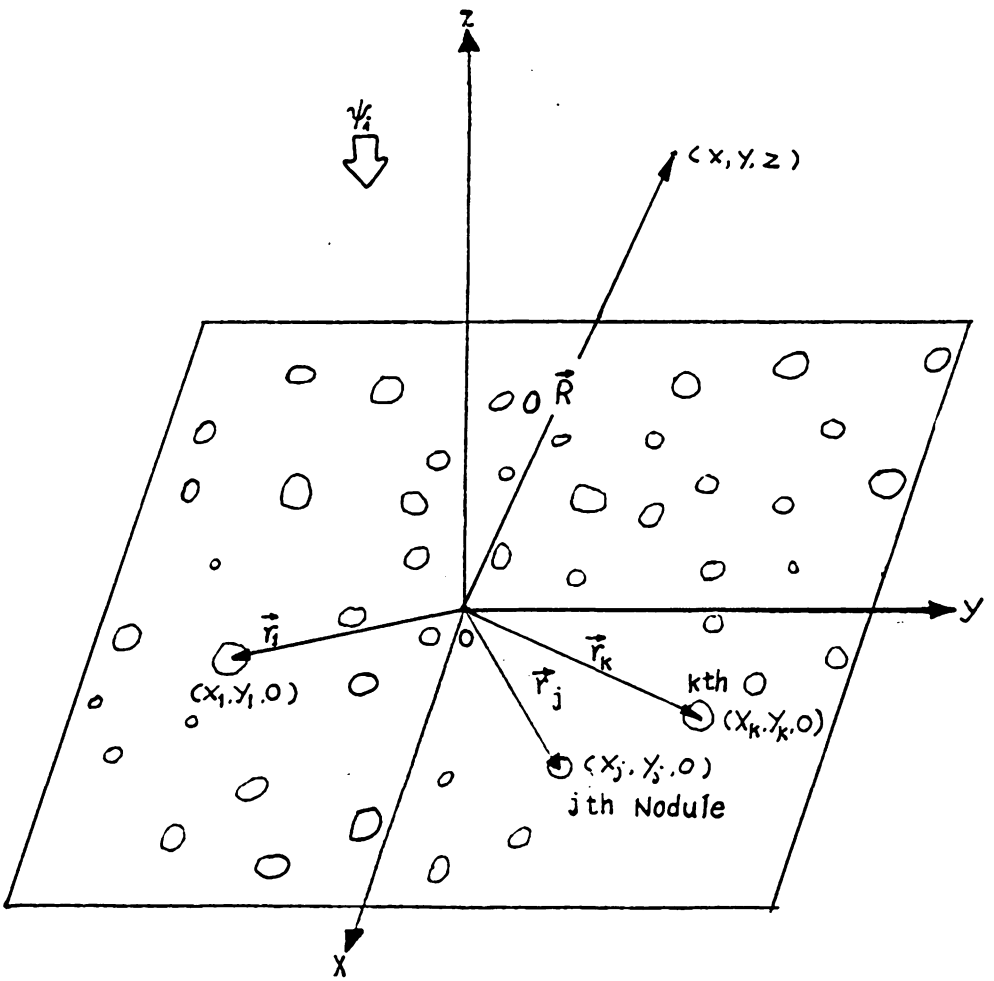

Figure 28. Coordinate System for Multiple Scattering Analysis

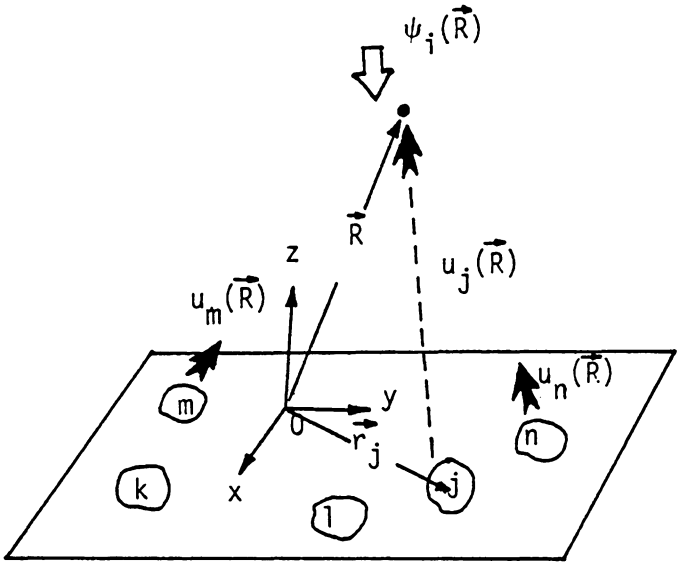

a. The Total Field at $\vec{R}$ (Incident and Scattered)

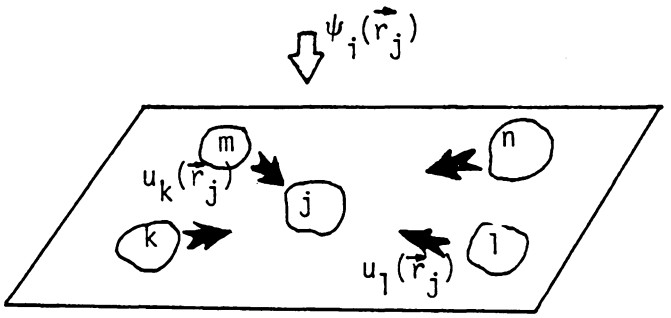

b. The External Field Acting on the jth Nodule

Figure 29. Schematic Representation of the Total Field and the External Field in Multiple Scattering.

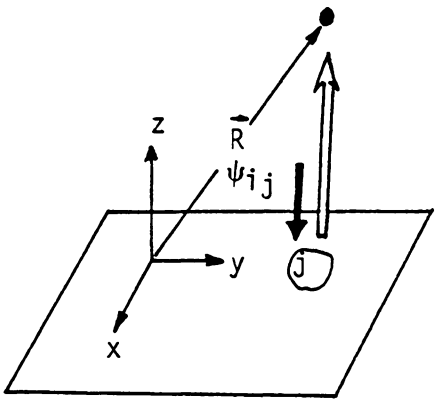

a. Single Scattering

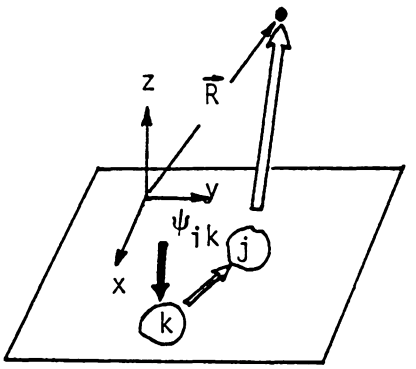

b. Double Scattering

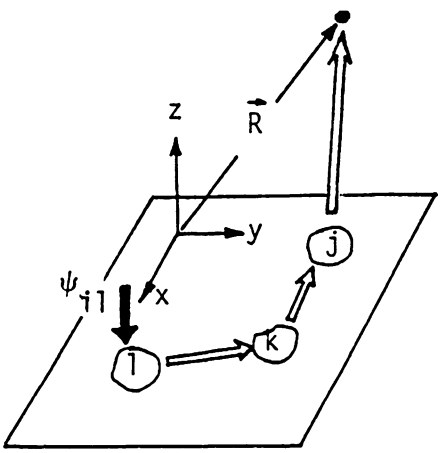

c. Triple Scattering

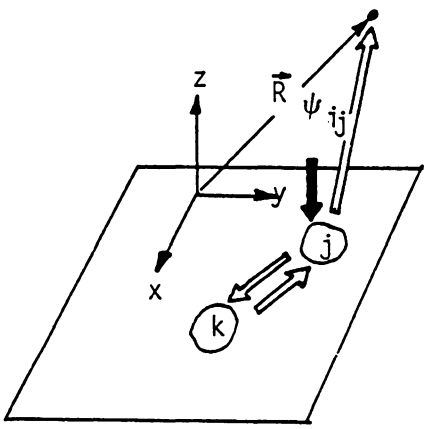

d. Ping-Pong Type Scattering

Figure 30. Schematic Representation of Different Orders of Multiple Scattering.

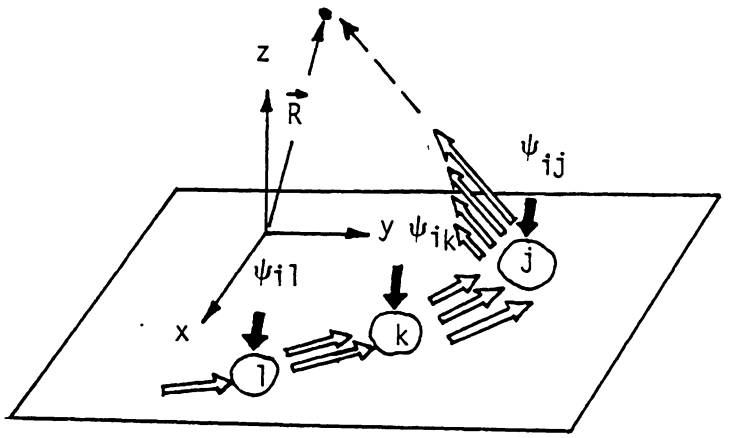

a. Multiple Scattering involves Chains of Successive Scattering

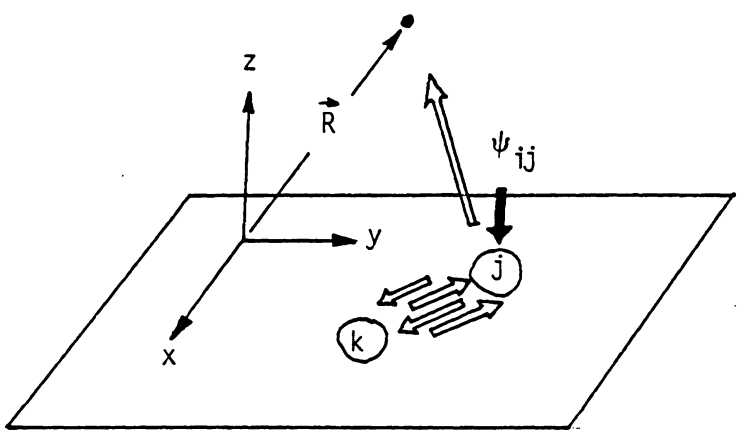

b. Multiple Scattering of Ping-Pong Type

Figure 31. Two Major Scattering Patterns in Multiple Scattering.

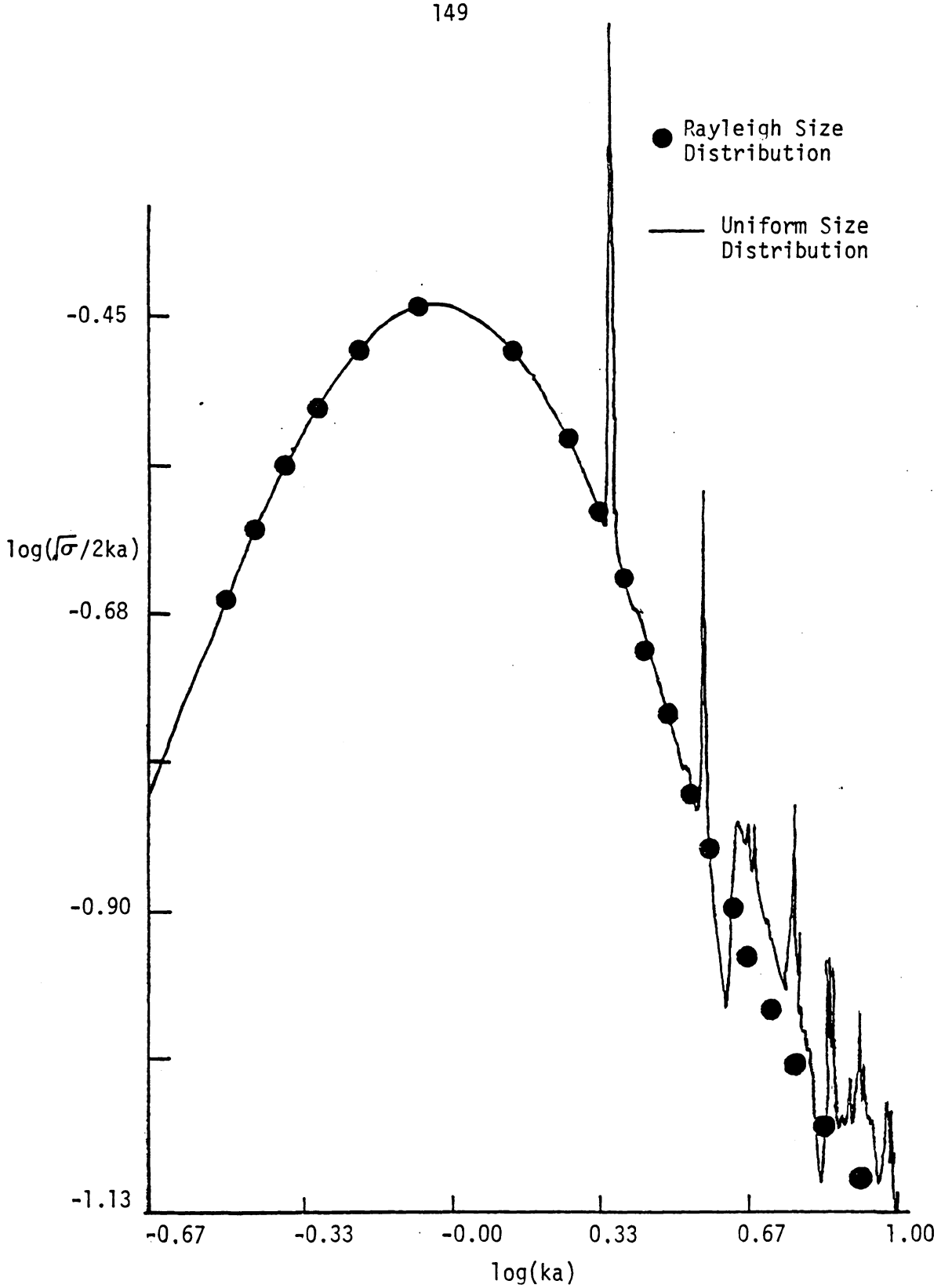

Figure 32. Effect of Size Averaging on the Acoustic Response.

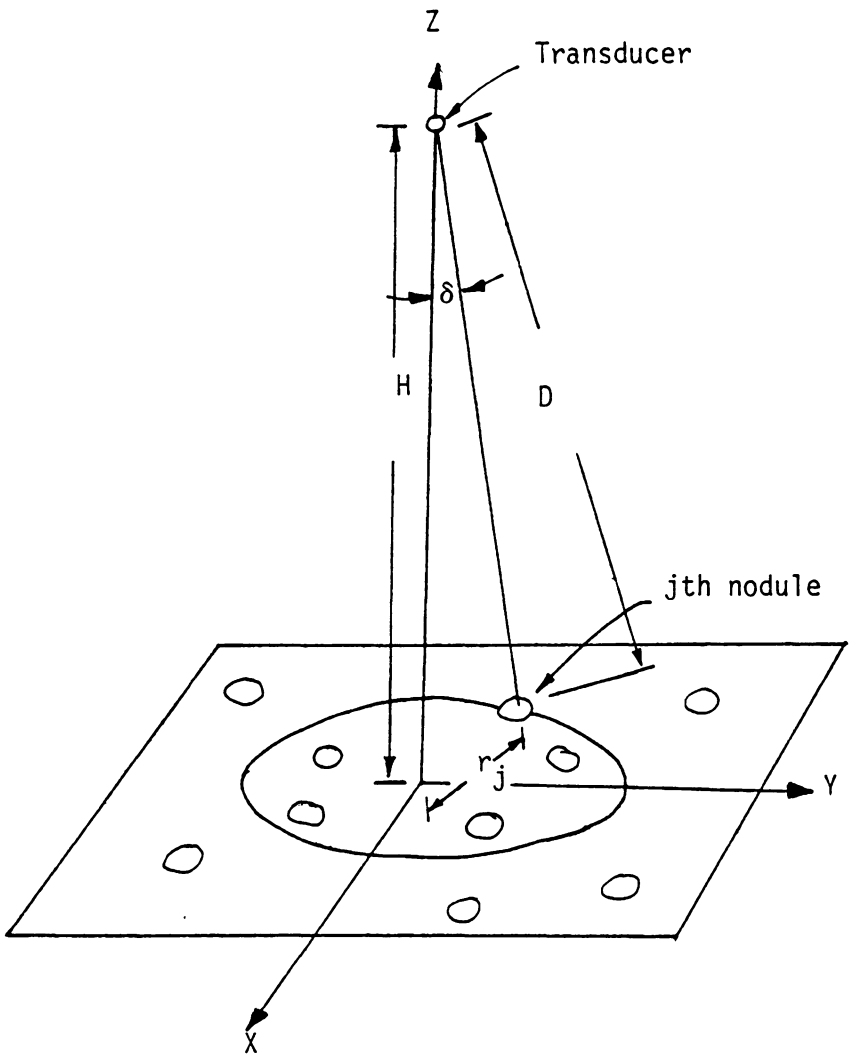

Figure 33. Geometry of the Narrow Beam Analysis.

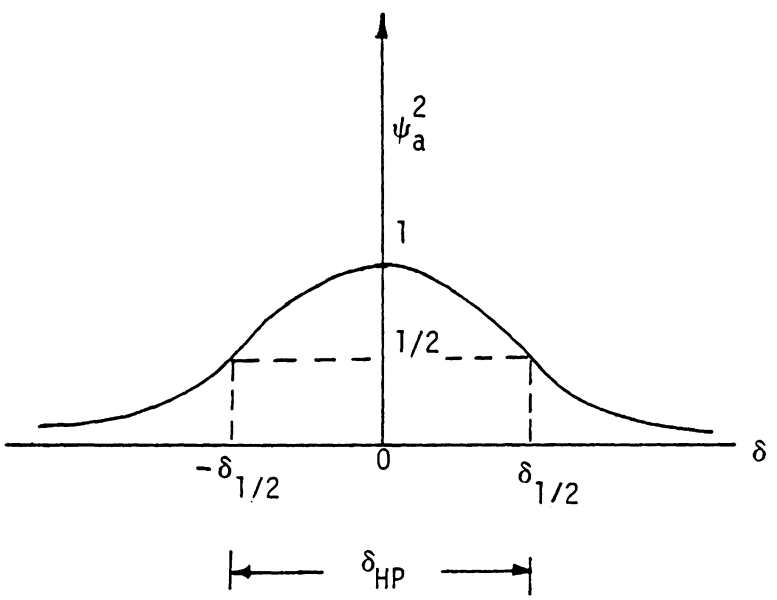

δ_{HP} = Half Power Beam Width = $2\delta_{1/2}$

Figure 34. Gaussian Beam Form.

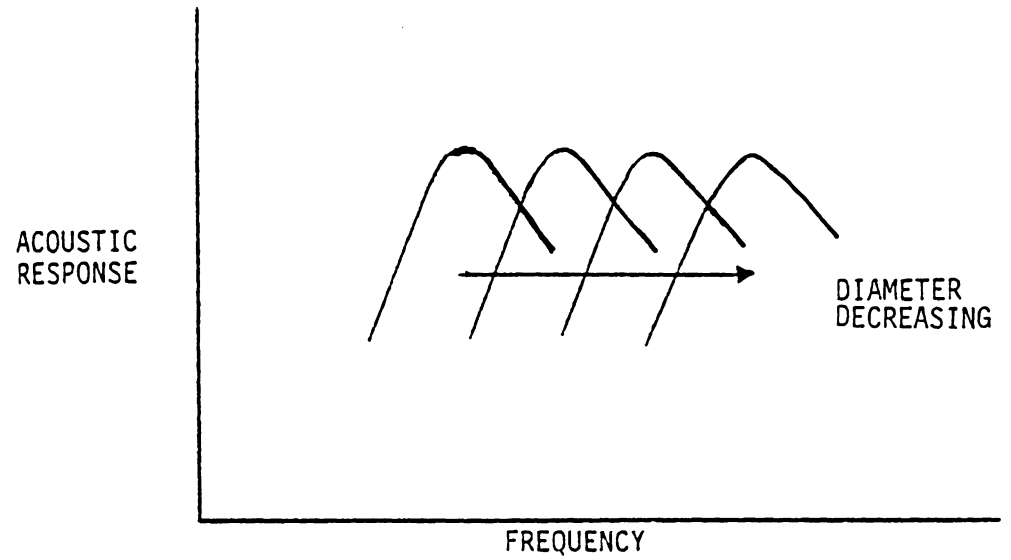

a. VARIATION WITH MEAN NODULE DIAMETER FOR DEPOSITS WITH SAME NUMBER DENSITY

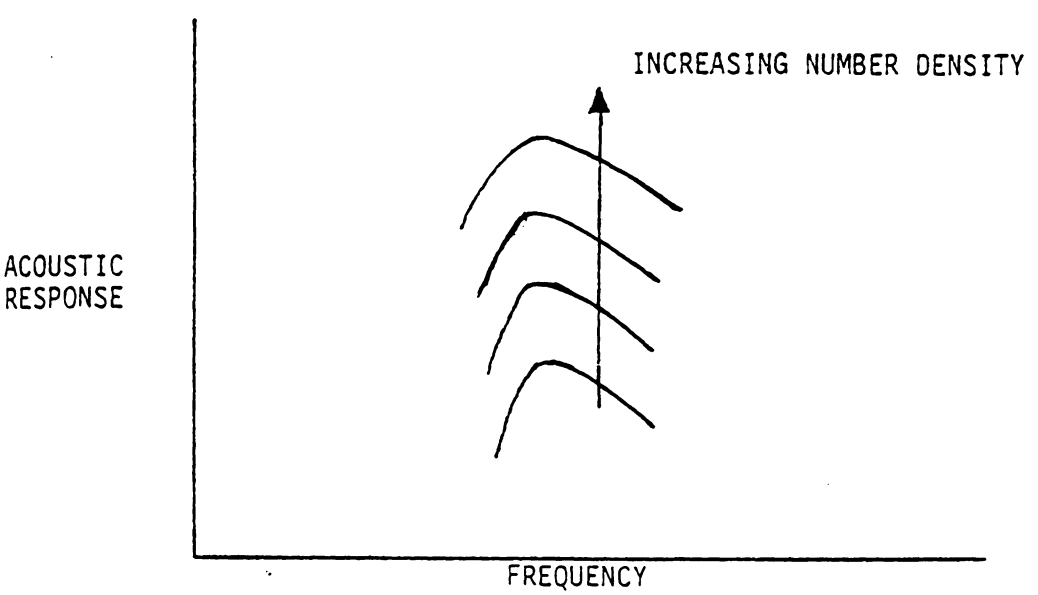

b. VARIATION WITH NUMBER DENSITY FOR FIXED MEAN DIAMETER OF NODULES

Figure 35. Acoustic Signature Trends for Nodule Deposits.

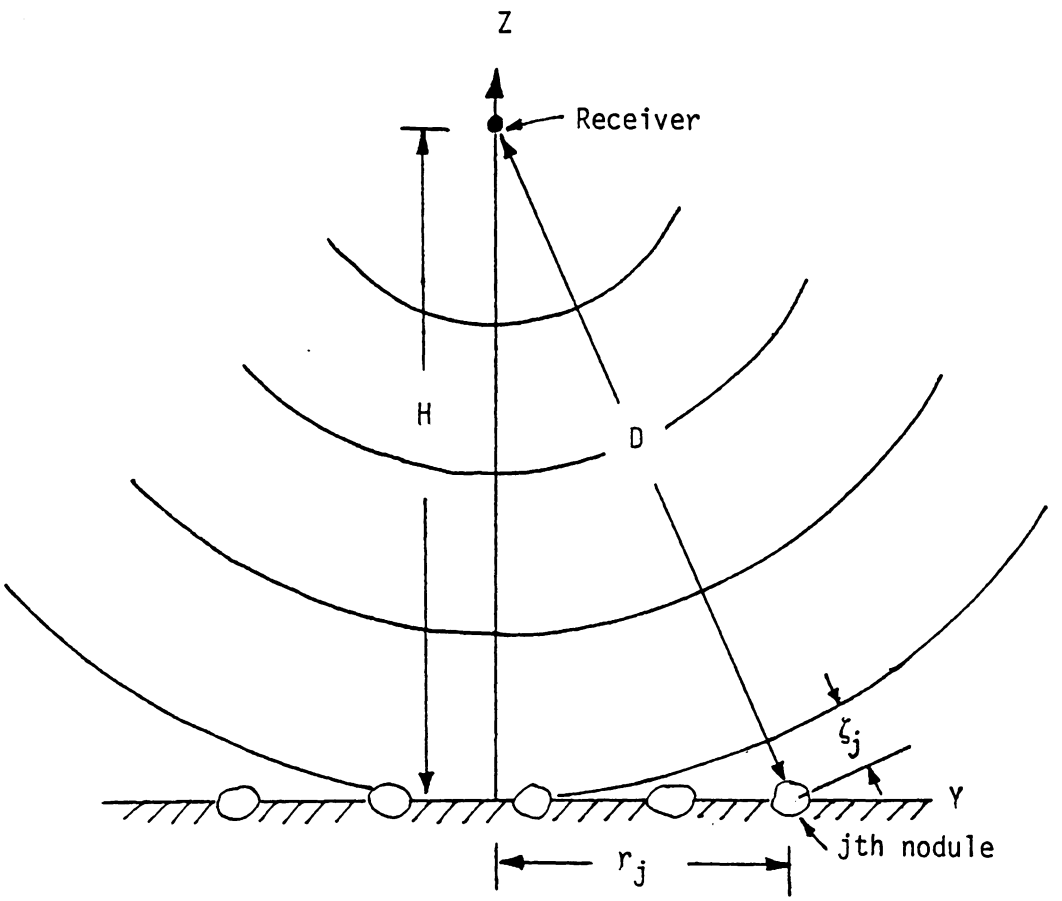

Figure 36. Sumitomo's Spherical Wave Model.

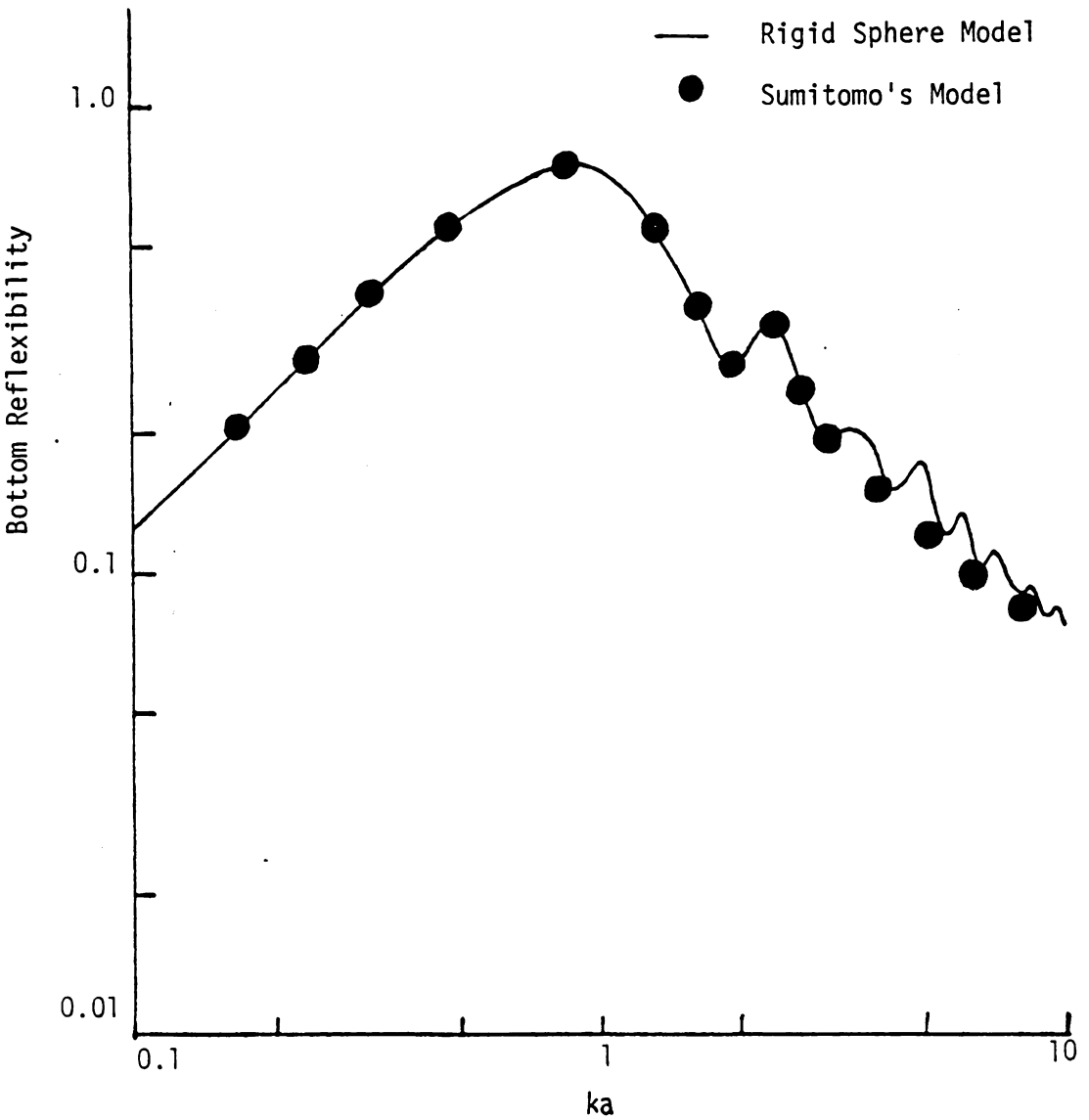

Figure 37. Sumitomo's Bottom Reflexibility.

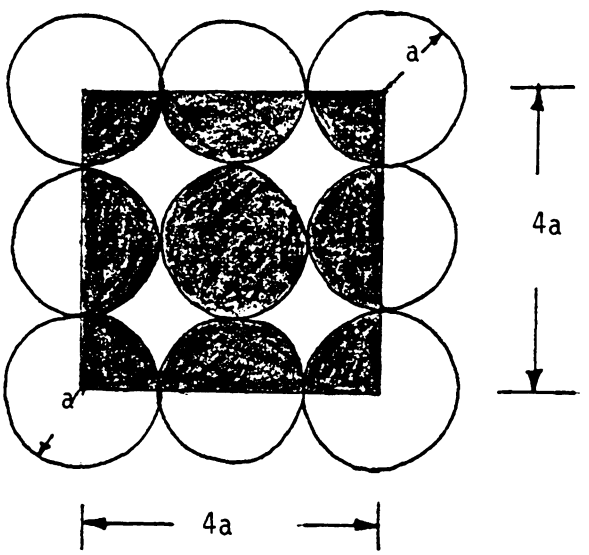

$$\text{Area Coverage} = \frac{\text{Cross Sectional Area of Nodules(Shaded)}}{\text{Area of Interest(Square)}}$$

$$= \frac{4 \times a^2}{16a^2} = 0.785$$

$$\text{Area Number Density} = \frac{\text{Number of Nodules}}{\text{Area of Interest}} = \frac{4}{16a^2} = \frac{1}{4a^2}$$

Figure 38. Simplified Bottom Profile Used in Sumitomo's Bottom Reflexibility Calculation.

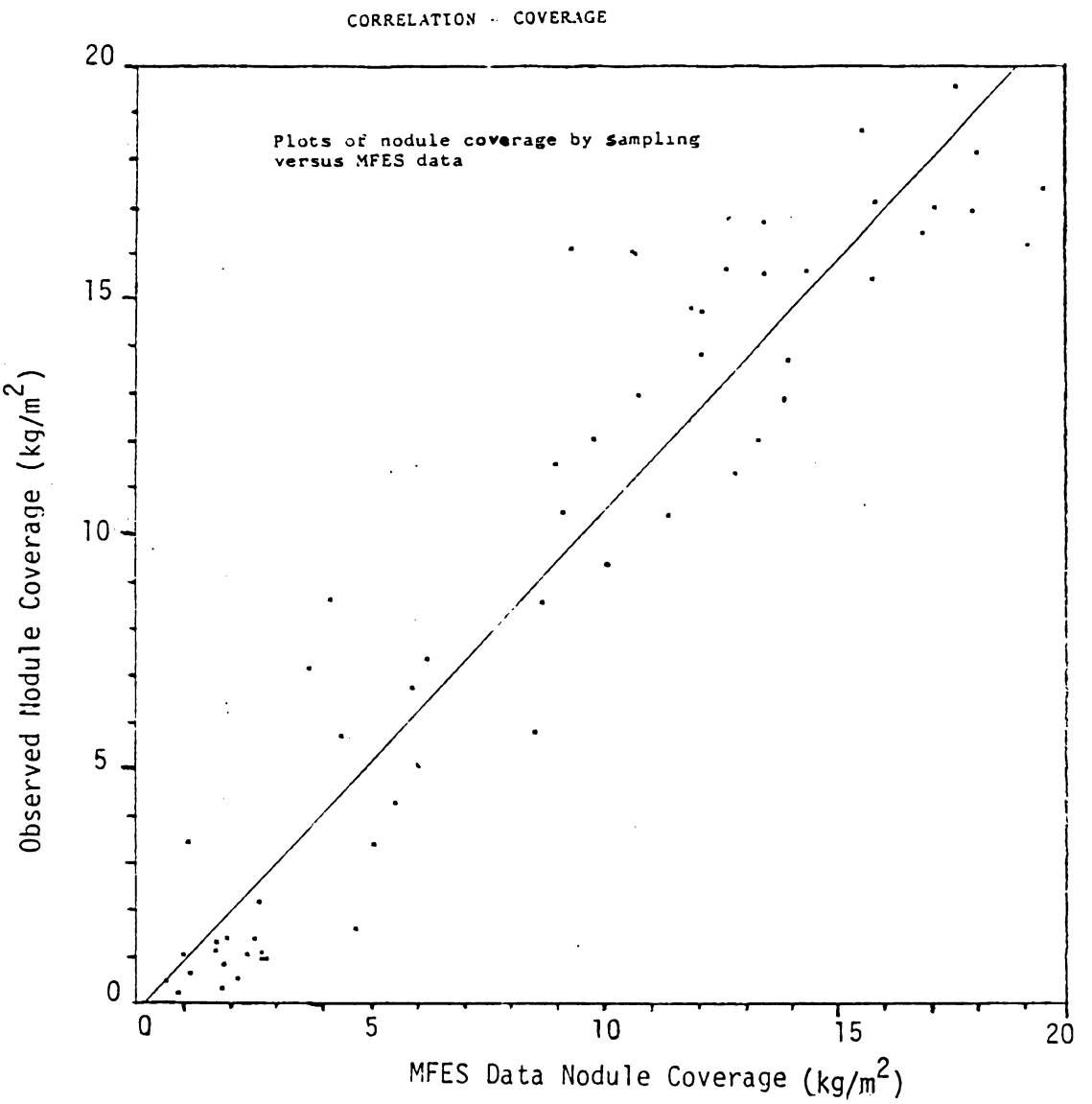

Figure 39. Correlation of Grab Sample (Measured) Nodule Coverage with MFES (Predicted) Sounding Data. (Courtesy of Sumitomo Metal Mining Co, Inc.)

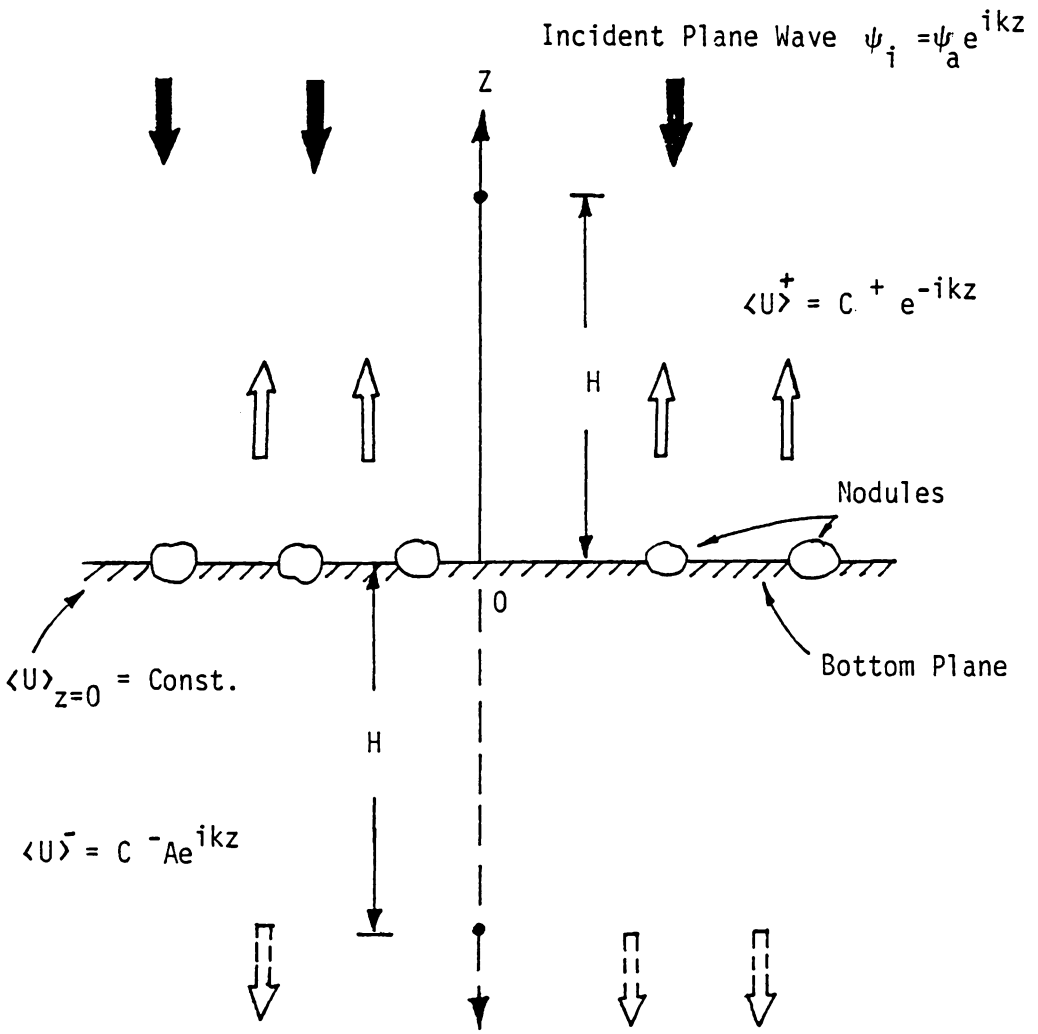

Figure 40. The Average Scattered Field Excited by a Normally Incident Plane Wave.

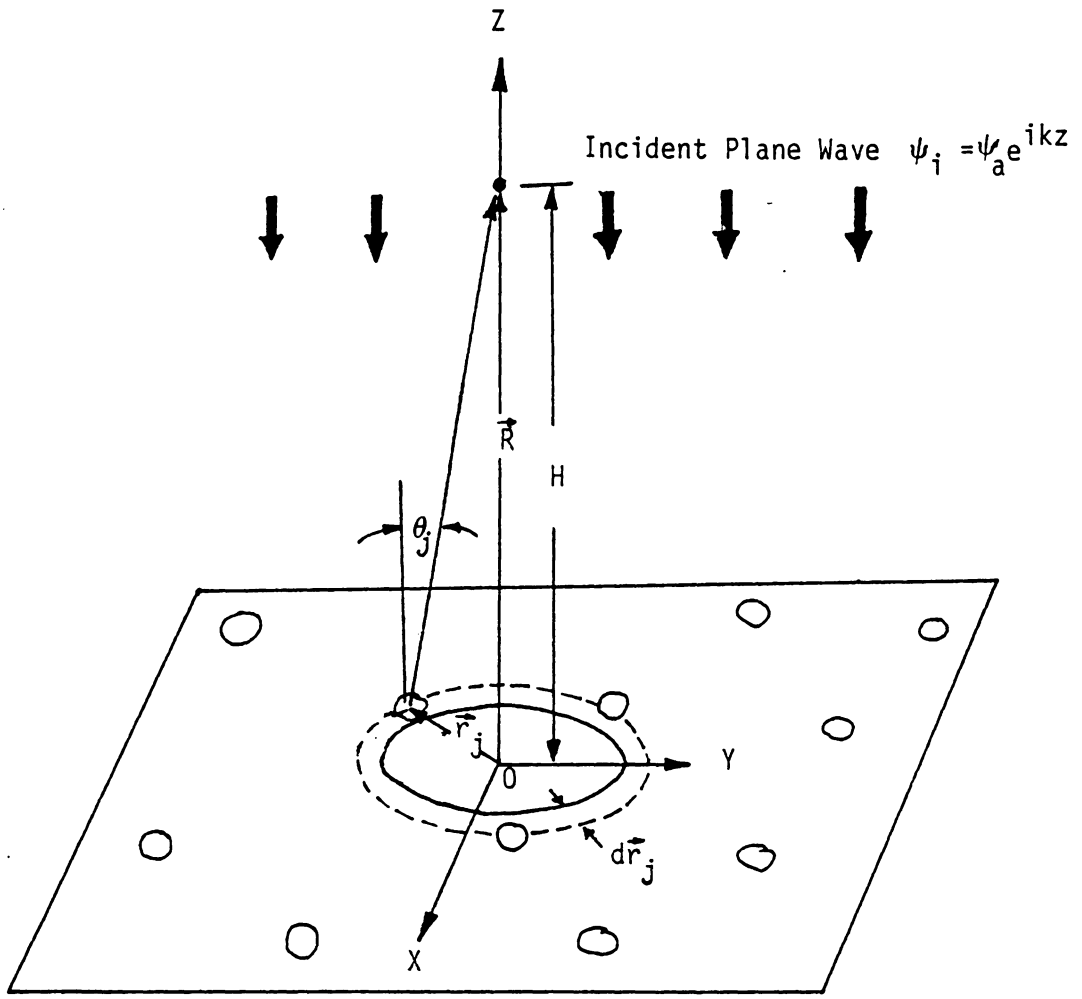

Figure 41. Scattering from Nodules on a Plane.

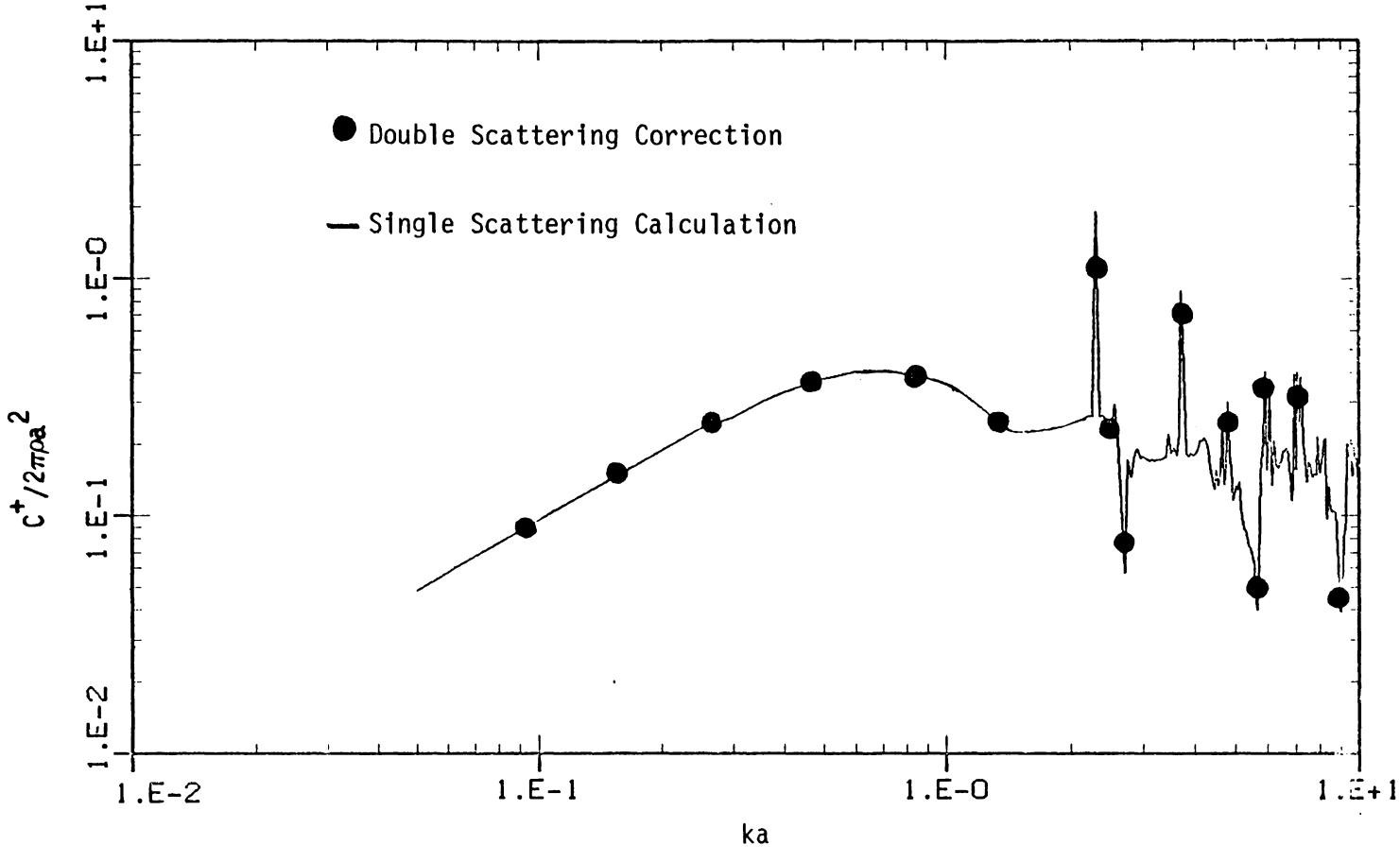

Figure 42. Equivalent Reflection Coefficient vs. ka for Uniform Size Distribution of Nodules.

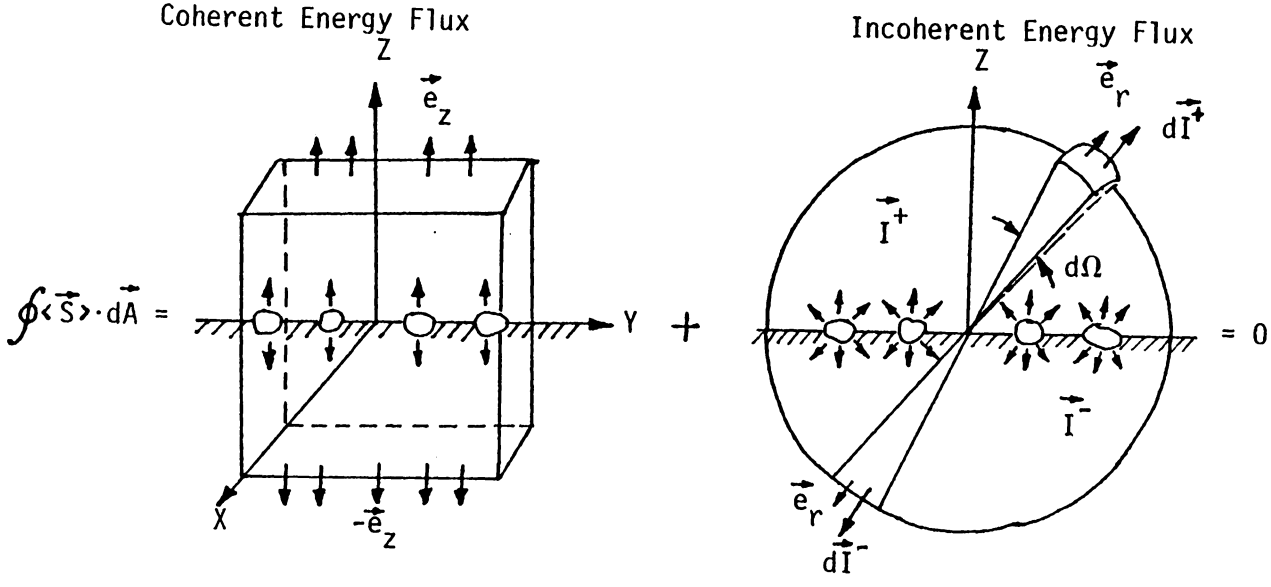

Figure 43. Control Volume for Energy Flux Consideration.

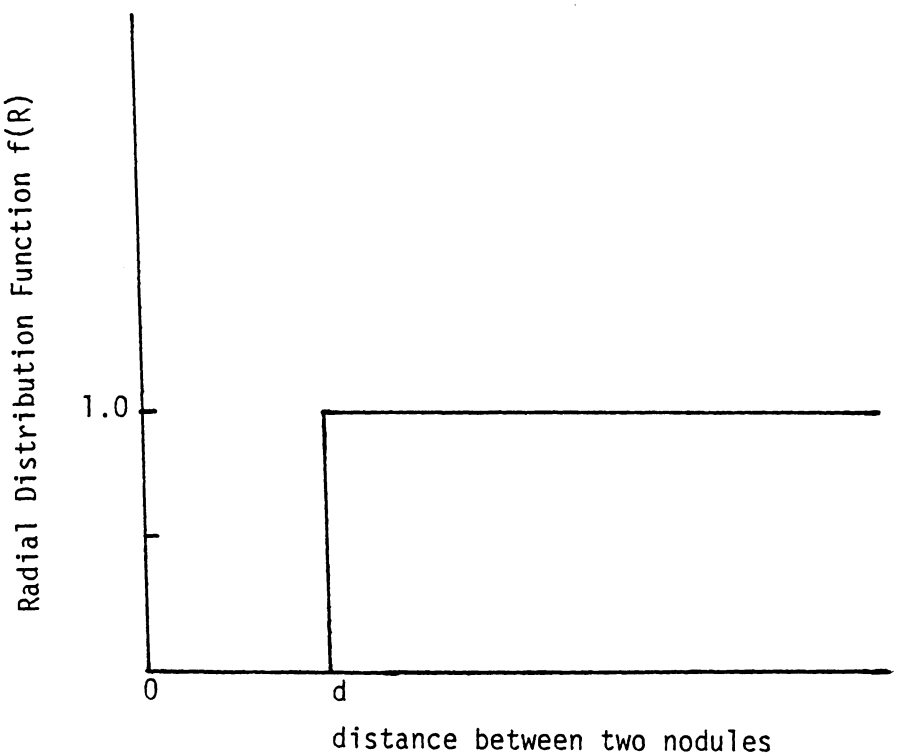

Figure 44. Simplified Radial Distribution Function.

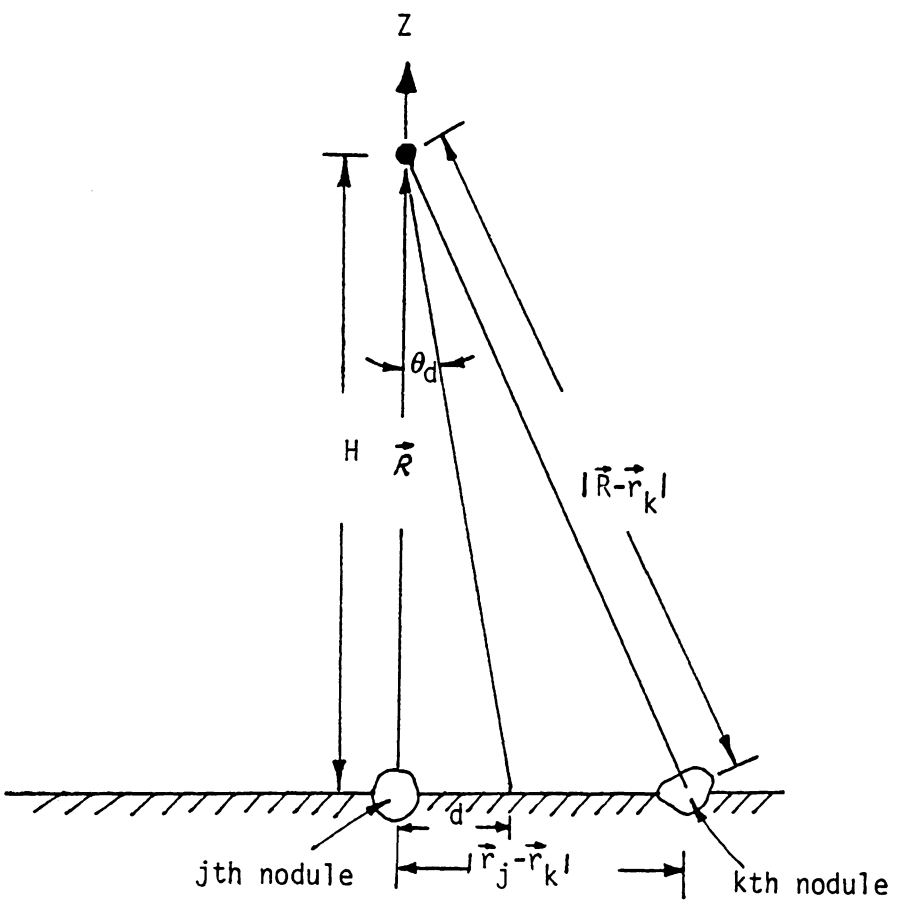

Figure 45. Geometry of the Scattering for Pair Correlated Nodules.

The vita has been removed from the scanned document

ACOUSTIC SCATTERING ANALYSIS FOR REMOTE SENSING OF MANGANESE NODULES

by

Yushieh Ma

(ABSTRACT)

The theory of the scattering of plane waves in a fluid medium by an isotropic elastic sphere representing a manganese nodule is developed. Scattering cross sections were computed using the theory and the results are presented graphically. The scattering cross section and the reflectivity factor govern the characteristic acoustic signature of the Pacific where manganese nodules are present.

Preliminary experimental data for the compressional and shear wave speeds in nodule material is given. This data was used in the scattering computations. Limiting cases of Rayleigh scattering and scattering from fixed rigid and fluid spheres are also shown for comparison. It is shown that the rigidity of the nodules dominates the high frequency response.

The problem of the multiple scattering of acoustic waves by randomly distributed nodules on the flat ocean bottom is investigated analytically. The statistical description of nodule deposits is given. The concept of the configurational average is introduced in order to obtain the average scattered response. The size averaging is found to be able to smooth the acoustic response in the high frequency region.

The plane wave analysis for the multiple scattering problem is justified by the narrow beam investigation. It shows that the beam effect on the average backscattered field can be neglected in the remote sensing.

For a planar distribution of nodules, the average scattered field excited by a normally incident plane wave is verified to be plane waves characterized by coherent reflection and transmission coefficients. The multiple scattering effect is found to be a higher order correction to the average scattered field. For a sparse distribution of nodules, the average scattered field can be well evaluated using the single scattering theory in which the scattering process is also shown to be energy conserved.

For a dense distribution of nodules, the radial distribution function is used in the Foldy-Lax hierarchy. The result shows that the pair correlation affects the phase of the second order correction term in the expression for the average scattered field when the higher order statistics are truncated using the quasi crystalline approximation.